Title

A Multiscale, Unconditionally Stable Multiphysics Time-Domain (MUST) Solver Unifying Electrodynamics, Elastodynamics and Spin Dynamics

Author

Yao, Zhi

Publication Date

2017

Peer reviewed|Thesis/dissertation

UNIVERSITY OF CALIFORNIA

Los Angeles

A Multiscale, Unconditionally Stable Multiphysics Time-Domain (MUST) Solver Unifying Electrodynamics, Elastodynamics and Spin Dynamics

A dissertation submitted in partial satisfaction of the

requirements for the degree Doctor of Philosophy

in Electrical Engineering

by

Zhi Yao

2017

ABSTRACT OF THE DISSERTATION

A Multiscale, Unconditionally Stable Multiphysics Time-Domain (MUST) Solver Unifying Electrodynamics, Elastodynamics and Spin Dynamics

by

Zhi Yao

Doctor of Philosophy in Electrical Engineering

University of California, Los Angeles, 2017

Professor Yuanxun Wang, Chair

The goal of this dissertation is to propose, elaborate, and validate a modeling, simulation and design tool for magnetic RF devices that encompasses the fields of electrodynamics, micromagnetics and other possible physics such as elastodynamics. Comparing to conventional approach based on magnetostatic approximations, our solution with full dynamics can provide a correct prediction to the electromagnetic power flow which determine the impedance match and radiation efficiency of a thin film magnetic filter or antenna.

First, we introduce both one-dimensional (1-D) and three-dimensional (3-D) modeling frameworks, with the former serving as the proof of the concept and the latter as a comprehensive modeling tool. The 1-D algorithm is based on an unknown reduction strategy to overcome the multiscale problem. The 3-D modeling is based on modified alternating-direction-implicit finite-difference time-domain methods (ADI FDTD) with unconditional stability. It has

the capability of modeling the anisotropic and dispersive properties of magnetic material. The proposed algorithms solve Maxwell's equations and Landau-Lifshitz-Gilbert (LLG) equation jointly and simultaneously, with verified accuracy and efficiency.

Second, we propose a novel antenna radiation mechanism, bulk-acoustic-wave (BAW) mediated multiferroic antenna. Such multiferroic antennas compose of piezoelectric material and magnetostrictive material, in which time-varying magnetic flux can be induced from the dynamic mechanical strain of acoustic waves. The BAW mediated multiferroic antenna can be used to create electromagnetic radiation and to alleviate the platform effect associated with low-profile conformal antennas. Its potential for efficient radiation of electromagnetic waves is evaluated by analytically deriving the lower bound of its radiation quality factor (Q factor). Moreover, the performance of the antenna is predicted by both the 1-D and 3-D modeling tools that we have developed. The study concludes that efficient antennas may be realized at GHz frequencies with thin film multiferroic material that has dimensions on the order of 10^{-5} wavelength.

Finally, we summarize the research results and discuss future potential research opportunities and challenges in this field. There are still many unresolved questions in this new research field. Nevertheless, the multiphysics time-domain solver that we proposed has shown the potential of an unprecedented ability to accurately model and design next-generation magnetic RF systems and components.

The dissertation of Zhi Yao is approved.

Tatsuo Itoh

Christopher S. Lynch

Robert N. Candler

Yuanxun Wang, Committee Chair

University of California, Los Angeles

2017

This dissertation is dedicated to my family,

for their unconditional love, encouragement and support.

TABLE OF CONTENTS

LIST OF FIGURES

LIST OF TABLES

SYMBOLS AND ACRONYMS

1-D/2-D/3-D	One-/Two-/Three-Dimensional
ADI	Alternating Direction Implicit
Al_2O_3	Alumina
AlN	Aluminum Nitride
BAW	Bulk Acoustic Waves
CFL	Courant-Friedrichs-Lewy
EM	Electromagnetic
FBAR	Film Bulk Acoustic Resonators
FDTD	Finite-Difference Time-Domain
FeGaB	Iron Gallium Boron
FMR	Ferromagnetic Resonance
FSL	Frequency Selective Limiters
LLG	Landau-Lifshitz-Gilbert
OOMMF	Object Oriented MicroMagnetic Framework
PEC	Perfect Electrically Conducting
Q factor	Quality Factor
SNE	Signal-to-noise Enhancers
Simulmag	PC Micromagnetic Simulator
YIG	Yttrium Iron Garnet
ZnO	Zinc Oxide

ACKNOWLEDGEMENTS

This dissertation was written as a testament to an invaluable experience and character enhancing journey. It has been a wonderful experience to have my graduate studies in the Digital Microwave Lab at UCLA. I have received numerous help from many people to make the work possible. I would love to especially thank my adviser, Professor Yuanxun Ethan Wang, for his insightful guidance, continuous support and encouragement in both the academic research and the daily life, for leading me to this fascinating field of electromagnetics and multiphysics, for guiding me to overcome various difficulties in the research, and for challenging me to come up with better ideas. I have also learned from Professor Wang the principles and philosophy in managing the lab, organizing the research and interacting with different people, which I really appreciate and would definitely benefit my future career.

I also would like to acknowledge Professor Tatsuo Itoh, Professor Christopher Lynch and Professor Robert Candler for serving as my doctoral committee members and giving me insightful comments and advice that greatly help me improve my work.

I am deeply grateful to my outstanding collaborators for their indispensable support and contribution to my research work. In particular, I would like to thank Professor Greg Carman and Dr. Paul Nordeen, Professor Robert Candler and Sidhant Tiwari at UCLA for their experimental realization and fabrication support. It is my great pleasure to work with many other talented researchers from multidiscipline. I appreciate the material support from Professor Jane Chang and Dr. Colin Rementer at UCLA, Professor Sarah Tolbert and Dr. Shauna Robbennolt at UCLA, Professor Nianxiang Sun and Dr. Tianxiang Nan at Northeastern University. I would also like to acknowledge Professor Sayeef Salahuddin and Dr. Dominic Labanowski at UC Berkeley,

Professor Abdon Sepulveda and Dr. Scott Keller at UCLA for the substantial theoretical support, and Professor Rashaunda Henderson and Nishanth Virushabadoss at UT Dallas for their experimental characterization.

My lab mates in Digital Microwave Lab have also provided tremendous amount of help to my research. Specifically, I would like to sincerely appreciate the unreserved help from Dr. Qiang Xu, on the fundamental understanding, sophisticated modeling and test setup. I also enjoy the inspiring discussion and collaboration with other lab mates who work on different fields, such as integrated circuit, antenna and wireless communication.

I would also like to thank Minji Zhu, the lab manager of the Center for High Frequency Electronics (CHFE) at UCLA, for his kind collaborations and support. I also appreciate Tom Normand's time and help at UCLA, with my expertise insight and career plan. I would like to acknowledge our staff members Celina Liebmann, Tsai-Tsai O-Lee and Michelle Schwartz at UCLA, for their kind assistance and support in preparing many documents, paperwork and mailings in my graduate studies.

I would like to thank Dr. Allen Tran at Qualcomm Research Center, for his useful technical advice, Professor Neville Luhmann at UC Davis, for his continuous help and caring advice, and Professor Zhizhang (David) Chen at Dalhousie University, for the inspiring conversation on the implementation of alternating-direction-implicit methods.

In this dissertation, Chapter 2 is mainly based on our manuscript titled with "A Multiscale, Unconditionally Stable Time-Domain (MUST) Solver Unifying Electrodynamics and Micromagnetics" and Chapter 3 is mainly based on our manuscript titled with "Bulk Acoustic Wave Mediated Multiferroic Antennas: Architecture and Performance Bound".

I also gratefully acknowledge sources of financial support for this work. Studies presented in Chapter 2 are supported by the DARPA Magnetic Miniaturized and Monolithically Integrated Components (M3IC) program, and NSF Nanosystems Engineering Research Center for Translational Applications of Nanoscale Multiferroic Systems (TANMS) Cooperative Agreement Award (No. EEC-1160504). The studies presented in Chapter 3 are also supported by TANMS. I also acknowledge the support from the Qualcomm Innovation Fellowship program and from the IEEE Antenna and Propagation Society Fellowship program, and the recognition from IEEE Microwave Theory and Techniques Society by awarding this work with the best paper honor in 2017 International Microwave Symposium.

Finally, I express my deepest love and special gratitude to my family for their unconditional love, encouragement and support.

VITA

Education

2014-2017 ***Graduate Student Researcher*** in **Electrical Engineering**
University of California, Los Angeles, USA

2012-2014 ***M.S.*** in **Electrical Engineering**
University of California, Los Angeles, USA

2008-2012 ***B.S.*** in **Optical Engineering**
Zhejiang University, Hangzhou, P. R. China

Selected Publications

[1] **Z. Yao**, R. U. Tok, T. Itoh and Y. E. Wang, "A Multiscale, Unconditionally Stable Time-Domain (MUST) Solver Unifying Electrodynamics and Micromagnetics," submitted to IEEE Transactions on Microwave Theory and Techniques, 2017.

[2] **Z. Yao**, Y. E. Wang, S. Keller and G. Carman, "Bulk acoustic wave mediated multiferroic antennas: architecture and performance Bound," IEEE Transactions on Antennas and Propagation, vol. 63, pp. 3335-3344, 2015.

Conference Presentations

[1] **Z. Yao** and Y. E. Wang, "3D Unconditionally Stable FDTD Modeling of Micromagnetics and Electrodynamics," 2017 IEEE International Microwave Symposium, Honolulu, Hawaii, June 4–9, 2017.

[2] **Z. Yao** and Y. E. Wang, "3D ADI-FDTD Modeling of Platform Reduction with Thin Film Ferromagnetic Material," 2016 IEEE International Symposium on Antennas and Propagation & USNC/URSI National Radio Science Meeting, Fajardo, Puerto Rico, June 26–July 1, 2016.

[3] **Z. Yao** and Y. E. Wang, "Bulk Acoustic Wave Mediated Multiferroic Antennas near Ferromagnetic Resonance," 2015 IEEE Antennas and Propagation Society International Symposium (APS/URSI), Vancouver, BC, July 19–25, 2015.

[4] **Z. Yao**, Q. Xu, and Y. E. Wang, "FDTD Analysis of Platform Effect Reduction with Thin Film Ferrite," 2015 IEEE Radio and Wireless Symposium (RWS), San Diego, USA, Jan. 25–28, 2015.

[5] **Z. Yao** and Y. E. Wang, "Dynamic Analysis of Acoustic Wave Mediated Multiferroic Radiation via FDTD Methods," 2014 IEEE International Symposium on Antennas and Propagation, Memphis, USA, Jul. 6–11, 2014.

Chapter 1

Introduction

1.1 Introduction to Multiphysics Modeling

Dynamic multiphysics is the general trend in the field of modern modeling. In most traditional modeling problems, one dynamic physics dominate. For example, in transformers, the dynamic electric circuit is modulated by the static magnetic hysteresis. In injection molds, thermotics is the key physics to consider. However, novel devices usually consist of multiphysics that equally contribute to the performance. For example, the voltage-controlled magnetic anisotropy (VCMA) memory involves spin dynamics, mechanics, and thermal dynamics [1]. In nanoscale motor, spin dynamics, magnetostriction, and mechanics are all dominant physics that determine the device performance [2]. Popular multiphysics simulators, such as Comsol Multiphysics and ANSYS Multiphysics, solve the coupled partial differential equations (PDEs) of electromagnetics (EM), mechanics, fluid flow, and chemical applications, however, may result in oversampling for problems of multiscale physics. This dissertation is focused on three multiscale physics that are frequently involved in novel RF devices: EM, elastodynamics, and micromagnetics.

1.1.1 EM and Micromagnetics

Ferrites and ferromagnets have been widely studied for RF devices, such as inductors, circulators, isolators [3-6], antennas [3, 7], frequency selective limiters (FSL) [8, 9] and signal-to-noise enhancers (SNE) [10]. Besides bulk magnetic materials, high-quality thin-film magnetic materials can now be reliably fabricated with nanofabrication technology. It is well known that

thin-film magnetic materials in micrometer or sub-micrometer scale thickness possess unique properties such as high in-plane permeability and high ferromagnetic resonance (FMR) frequency due to the out-of-the-plane demagnetization effects [5, 6]. These unique properties of thin films may lead to a variety of new applications in microwave communication systems, wearable devices and implantable devices for diagnosis. Understanding the role of micromagnetic effects of the material is significant for advanced design and fabrication of RF magnetic devices, because such devices often take advantage of the strong coupling between the dynamic magnetization and the EM field. On the other hand, the lack of effective modeling tools tackling the interactions between oscillating magnetization and EM waves has hindered the state of the art in design of RF magnetic devices due to the insufficient understanding of the underlying physics in a quantitative manner.

In micromagnetic theory represented by Landau-Lifshitz-Gilbert (LLG) equation, the property of magnetic material is designated by the magnetic moment of orbital and spin of electrons. The Larmor precession of the spin creates a resonant frequency in the material property, defined by FMR. The state-of-the-art micromagnetic simulators, such as FastMag [11], PC Micromagnetic Simulator (Simulmag) [12] and Object Oriented MicroMagnetic Framework (OOMMF) [13], solve LLG equation dynamically with coupling to the magnetostatic solution. These tools, however, do not predict the interaction between the magnetization and EM waves. Full-wave EM simulators, such as HFSS and CST, solve Maxwell's equations with defined material dispersion and anisotropy, i.e. applying Polder's permeability tensor as the constitutive relation. In fact, progressive works on interacting EM and micromagnetics have been published in, but not limited to, [14-20]. The existence of weak solutions in the three-dimensional (3-D) Maxwell-LLG system has been studied first in [14]. Concerning the numerical analysis of this

system, closely related works include [16-20]. In [16, 19, 20], Maxwell's equations are taken under the magnetostatic limit. In [17], a weak formulation is adapted to the continuous Maxwell-LLG problem. In [18], the nonuniform field distributions are obtained by an iterative method. The FDTD solution of dynamic Maxwell's equations and LLG equation was obtained in [15], showing the two-dimensional (2-D) analysis of ferrite-loaded waveguides at frequencies below FMR frequency.

We propose for the first time an efficient and accurate 3-D modeling tool for multiphysics problems that encompasses the fields of electrodynamics and micromagnetics. The proposed modeling is based on a modified finite-difference-time-domain (FDTD) [21, 22] method that jointly solves Maxwell's equations and LLG equation. The advantage of utilizing FDTD method is that the intrinsic nonlinearity of magnetic material favors time-domain representation. However, conventional FDTD algorithm is subject to Courant–Friedrichs–Lewy (CFL) condition, which limits the time-step size to $\Delta t \leq \Delta/(\sqrt{3}c)$, with Δ being the spatial mesh size. Models described by LLG equation often require very fine grained discretization, which may result in tiny time-step sizes in the modeling, and consequently, impractical computational complexity. Therefore, unconditionally stable FDTD algorithms are necessary in order for the time step to surpass the CFL condition. Both implicit [23-28] and explicit [29] unconditionally stable FDTD algorithms for EM wave computation were developed previously, with satisfactory reliability and accuracy. In this work, we adopted alternating-direction-implicit (ADI) FDTD formulation [23, 24] due to the easy implementation and controllable accuracy.

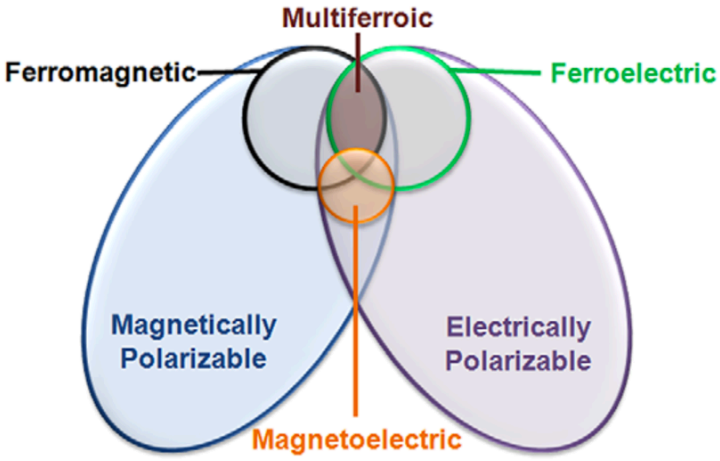

(a)

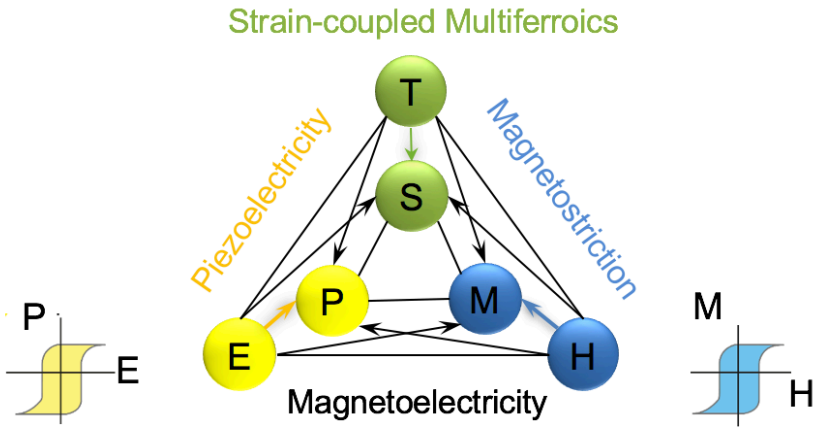

(b)

Figure 1.1-1. Types of coupling in materials and multiferroic materials. **a.** Relationship between multiferroic and magnetoelectric materials. **b.** Schematic illustrating different types of coupling present in materials. Much attention has been given to materials where electric and magnetic order is coupled. These materials are known as magnetoelectric materials [30].

1.1.2 Multiferroics

Schmid coins the term "multiferroic" in 1994 [31]; since then, thousands of papers have been published investigating the attractive properties of this type of material. Multiferroic materials are materials that exhibit at least two, and sometimes all three, types of ferroic ordering in the same phase. The ferroic orderings are ferroelectric, ferromagnetic and ferroelastic and relate to the type of applied field required for the material to exhibit a spontaneously polarized state. Fig. 2.1.1 shows these types of ferroic ordering, where an applied electric, magnetic or stress field induces a spontaneous electric polarization, magnetization or strain, respectively [30]. However, in multiferroics additional levels of ordering can result from the coupling between the different types of ferroic ordering. For instance, in a magnetoelectric multiferroic, an applied magnetic field can be used to control the polarization, or an applied electric field could be used to control the magnetization.

1.2 Introduction to BAW Mediated Multiferroic Antennas

Traditional antennas such as dipoles and loops generate propagating electromagnetic waves from conductive currents exposed in free space. Such antennas, however, radiate poorly when placed at a short distance above a conducting plane. This is because an image current flowing in the opposite direction is generated by the platform and it cancels the radiation of the original antenna. The platform effect is also described by the excessive storage of reactive energy between the radiating element and the platform, which elevates the radiation Q factor and makes the antenna difficult to match [32, 33].

Using magneto-dielectric material to reduce the high radiation Q factor associated with the platform effect has been extensively studied in [34-40], where optimization of the bandwidth and

efficiency performance of specific antenna structures, such as microstrip patch antennas, have been discussed. The usages of both natural magnetic material [37, 38, 41] and artificial magnetic material [39] to alleviate the platform effect have been considered. Recently, the emergence of multiferroic material that couples electric field, magnetic field and mechanical field has received great attention [42-47]. In particular, the composite of piezoelectric and magnetostrictive material, with the mechanical strain as the medium between the coupling of electric field and magnetic field can exhibit giant multiferroic coupling needed for practical applications [46]. It has been proposed to utilize such composite multiferroic materials to miniaturize the RF antenna dimensions as they exhibit high permittivity and high permeability simultaneously [48]. Another application of composite multiferroic material is to create frequency reconfigurable antennas by altering the magnetic property of the material with electric field [41].

1.2.1 Overview

We propose a new class of antennas called strain mediated multiferroic antennas [49]. Instead of using conductive currents, dynamic electric flux (displacement current) or magnetic flux is utilized as the radiation source of multiferroic antennas. To achieve this purpose, dynamic strain is induced in a thin piezoelectric or piezomagnetic plate to generate a dynamic flux density, which then forms the aperture field on the surface of the plate resulting in outgoing electromagnetic waves. For example, electromagnetic radiation may be created through vibrating a piezoelectric plate mechanically as envisioned and formulated in [50-53]. Strain-mediated antennas offer several potential advantages compared to conductive current based antennas. First, the Ohmic loss associated with the current conduction is absent, which promises superior radiation efficiency. Second, the platform effects may be overcome if strain mediated magnetic

flux is used as the radiation source flowing above the conducting platform. This is because the image effect by the conducting platform enhances rather than cancels the radiation effects of the magnetic flux. Third, strain mediated antennas can be designed with minimum or no conductor elements over a conducting ground plane, which helps to achieve low observability and robustness against strong interferences. On the other hand, one must realize that generating and coupling a dynamic strain at RF frequency into a device is not a trivial task. The distribution of strain is often not uniform as dynamic mechanical vibrations may generate acoustic waves that can propagate, scatter and radiate in or out of the structure. These effects cannot be ignored once the structure dimension is comparable to the acoustic wavelength, which is on the order of several micrometers. Therefore, generation and propagation of acoustic waves must always be included in the consideration.

A strain mediated antenna structure is proposed as a vehicle to study how the platform effects can be overcome by decreasing the radiation Q factor with the multiferroic coupling. The proposed antenna structure consists of a sandwich of two layers of piezoelectric material and one layer of magnetostrictive material and it relies on bulk acoustic wave (BAW) resonances to transfer the dynamic strain across different layers. Analyses show that, the radiation quality factor can be significantly lowered with high permeability and a high magnetomechanical coupling figure of merit in the magnetostrictive material, which could lead to low profile antennas with high radiation efficiency. Then we develop a multi-physics and multi-scale modeling tool to emulate the dynamic, two-way interactions between electromagnetic waves and acoustic waves. The model must be based on the fundamental laws of electrodynamics, Maxwell's equations and elastodynamics, Newton's equations. A one-dimensional finite-difference time-domain (1D FDTD) technique [21, 54-57] is developed for the purpose of

proving the concept, where Newton's law and Maxwell's equations are solved jointly in time domain. The dynamic response of the stress profile is simulated and from which the radiation Q factor is derived. The radiation Q is then compared to the analytical results. The BAW mediated antenna performance is also predicted by the full 3-D multiscale and unconditionally stable modeling tool that we propose in Chapter 2. Lastly, we identify the material property required for practical implementation of multiferroic antennas through the modeling. It is concluded that a multiferroic antenna can be built with a thickness of only a few micrometers above a conducting plane provided the relative permeability of the magnetic material can reach to a few thousands and the magnetomechanical coupling figure of merit is greater than 85%.

1.2.2 Multiferroic Constitutive Relations

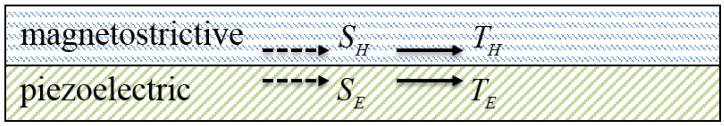

Figure 1.2-1. Composite multiferroic structure formed by lamination of one layer of piezoelectric film and one layer of magnetostrictive layer.

A typical configuration of multiferroic composite is through a laminate of piezoelectric and magnetostrictive layer, shown in Figure 1.2-1. The lamination interface between the layers is assumed to be perfect so that the mechanical strain is continuous across the interface. The multiferroic constitutive relationship is then described by the following equations [58].

$$\begin{bmatrix} \boldsymbol{S_E} \\ \boldsymbol{D} \end{bmatrix} = \begin{bmatrix} \boldsymbol{s_E} & \boldsymbol{d_E} \\ \boldsymbol{d_E} & \boldsymbol{\epsilon_T} \end{bmatrix} \begin{bmatrix} \boldsymbol{T_E} \\ \boldsymbol{E} \end{bmatrix} \tag{1.2-1}$$

$$\begin{bmatrix} \boldsymbol{S_H} \\ \boldsymbol{D} \end{bmatrix} = \begin{bmatrix} \boldsymbol{s_H} & \boldsymbol{d_H} \\ \boldsymbol{d_H} & \boldsymbol{\mu_T} \end{bmatrix} \begin{bmatrix} \boldsymbol{T_H} \\ \boldsymbol{H} \end{bmatrix} \tag{1.2-2}$$

where $\boldsymbol{T_{E,H}}$ and $\boldsymbol{S_{E,H}}$ stand for the stress and strain field tensors in the piezoelectric layer and magnetostrictive layer respectively. $\boldsymbol{E}$ and $\boldsymbol{H}$ are the electric and magnetic field intensity vectors, $\boldsymbol{D}$ and $\boldsymbol{B}$ are the electric and magnetic flux density vectors. In the piezoelectric strain equation (1.2-1), $\boldsymbol{\epsilon_T}$ is the stress-free permittivity. The coefficient $\boldsymbol{s_E}$ is the compliance constant, and it is a fourth rank tensor. The coefficient $\boldsymbol{d_E}$ is the strain constant or piezoelectric coefficient, and it is a third rank tensor. Subscripts *T* and *E* have been added to $\boldsymbol{\epsilon}$ and $\boldsymbol{s}$ to show that these coefficients describe dielectric and elastic properties measured under conditions of constant stress and constant electric field, respectively [58]. In the magnetostrictive strain equation (1.2-2), $\boldsymbol{\mu_T}$ is the stress-free permeability, the fourth-rank tensor $\boldsymbol{s_H}$ is the compliance constant, and the third-rank tensor $\boldsymbol{d_H}$ is the strain constant or piezomagnetic coefficient. Similarly, the subscripts *T* and *H* added to $\boldsymbol{\mu}$ and $\boldsymbol{s}$ show that these coefficients describe magnetic and elastic properties measured under conditions of constant stress and constant magnetic field, respectively. For simplicity, assuming all the field variables are uni-directional in the horizontal plane and the strain and stress are uniform within each layer. The boundary conditions enforced by the interface in the stationary state are $\boldsymbol{S_E} = \boldsymbol{S_H}$, $\boldsymbol{T_E} = -\boldsymbol{T_H}$. One can then merge Eq. (1.2-1) and Eq. (1.2-2), by eliminating the mechanical field variables, which yields

$$\begin{bmatrix} \boldsymbol{D} \\ \boldsymbol{B} \end{bmatrix} = \begin{bmatrix} \boldsymbol{\epsilon_T} - \frac{\boldsymbol{d_E^2}}{\boldsymbol{s_E + s_H}} & \frac{\boldsymbol{d_E \cdot d_H}}{\boldsymbol{s_E + s_H}} \\ \frac{\boldsymbol{d_E \cdot d_H}}{\boldsymbol{s_E + s_H}} & \boldsymbol{\mu_T} - \frac{\boldsymbol{d_H^2}}{\boldsymbol{s_E + s_H}} \end{bmatrix} \begin{bmatrix} \boldsymbol{E} \\ \boldsymbol{H} \end{bmatrix} \tag{1.2-3}$$

This is in the form of the constitutive relations of the famous bianisotropic magnetoelectric material [57], where the electromagnetic flux densities and fields are cross coupled. In a dynamic strain mediated system, however, the bianisotropic relations described by Eq. (1.2-3) do not hold in general as the strain and stress are often functions of time and space. Consequently, the discussions on the dynamic property of multiferroic material must be carried out concerning the dynamic, bilateral interactions between electrodynamics and dynamic mechanics. The equations Eq. (1.2-1) and Eq. (1.2-2) can be rewritten in the following alternative form:

$$T = -\frac{e_D}{\epsilon_S} D + c_D S, \;\; E = \frac{1}{\epsilon_S} D - \frac{e_D}{\epsilon_S} S \tag{1.2-4}$$

$$T = -\frac{e_B}{\mu_S} B + c_B S, \;\; H = \frac{1}{\mu_S} B - \frac{e_B}{\mu_S} S \tag{1.2-5}$$

where e_D and e_B are the stress constants of the piezoelectric and magnetostrictive material for constant strain, which are related to the parameters in Eq. (1.2-1) and Eq. (1.2-2) by $e_D = d_E/s_E = d_E \cdot c_E$ and $e_B = d_H/s_H = d_H \cdot c_H$. The coefficients c_E and c_H are the Young's modulus of the material measured under constant electric field and magnetic field, which are inversions of the mechanical compliances measured under the same condition, e.g. $c_E = 1/s_E$ and $c_H = 1/s_H$. The coefficients c_D and c_B in Eq. (1.2-4) and Eq. (1.2-5) are mechanical compliances measured under constant electric and magnetic flux densities. ϵ_S and μ_S are constant strain permittivity and permeability and they are related to the constant electromagnetic field and stress parameters through the following,

$$\begin{cases} c_D = \frac{c_E}{1-k_E^2} \\ c_B = \frac{c_H}{1-k_H^2} \end{cases}, \; \begin{cases} \epsilon_S = \epsilon_T(1-k_E^2) \\ \mu_S = \mu_T(1-k_H^2) \end{cases} \tag{1.2-6}$$

where k_E^2 and k_E^2 are respectively electromechanical and magnetomechanical coupling figures of merits, given by

$$k_E^2 = \frac{d_E^2}{s_E \epsilon_T},\ k_H^2 = \frac{d_H^2}{s_H \mu_T} \tag{1.2-7}$$

The definition of energy in a multiferroic system can appear varied depending on which field quantities are viewed as the independent variables in the equation. As a consequence, an energy formulation can be obtained in terms of either stress or strain for the mechanical variables or in terms of flux density or field density for the electromagnetic terms. In this discussion, we write the mechanical energy in terms of stress and the electromagnetic energy in terms of the flux density. Using magnetostrictive layer as an example, a variation of Eq. (1.2-2) can be written as,

$$S = s_B T + \frac{d_H}{\mu_T} B,\ H = -\frac{d_H}{\mu_T} T + \frac{1}{\mu_T} B \tag{1.2-8}$$

The total stored energy W_{Total} in the magnetic phase of the system according to this definition is given by:

$$\begin{aligned} W_{Total} &= \frac{1}{2} \iiint S \cdot T \, dv + \frac{1}{2} \iiint B \cdot H \, dv \\ &= \frac{1}{2} \iiint s_B \cdot |T|^2 \, dv + \frac{1}{2} \iiint \frac{|B|^2}{\mu_T} dv \end{aligned} \tag{1.2-9}$$

where $s_B = 1/c_B = (1 - k_H^2) s_H$ is the mechanical compliance defined for constant magnetic flux density. Note that the total energy input to the system is now stored as a summation of the mechanical energy in the form of mechanical stress and the magnetic energy in the form of magnetic flux density $W_B = \frac{1}{2} \iiint \frac{|B|^2}{\mu_T} dv$. The weak magnetic field condition holds when $|H| \ll |B|/\mu_T$ as it will be seen in the following proposed antenna system. In this case, the energy in the system established by or released to the magnetic field in the outside world can be a small fraction of what is in the system stored in the form of magnetic flux density, e.g.

$$\left|\frac{1}{2}\iiint B \cdot H \, dv\right| \ll W_B = \frac{1}{2}\iiint \frac{|B|^2}{\mu_T} dv \tag{1.2-10}$$

This leads to the observation that the input of the energy to the system is primarily mechanical while the stored energy is in the forms of both mechanical stress and magnetic flux density as part of the mechanical energy is transferred to the magnetic energy, which is

$$W_{Total} \approx \frac{1}{2}\iiint S \cdot T \, dv = \frac{1}{2}\iiint s_B \cdot |T|^2 \, dv + \frac{1}{2}\iiint \frac{|B|^2}{\mu_T} dv \tag{1.2-11}$$

On the other hand, it is obvious under the weak magnetic field assumption that $H \approx 0, B \approx d_H T$ from the second equation in Eq. (1.2-8). Substituting this relationship into Eq. (1.2-9) results,

$$W_{Total} = \frac{1}{2}\iiint s_B \cdot |T|^2 \, dv + \frac{1}{2}\iiint \frac{d_H^2}{\mu_T} |T|^2 \, dv = \frac{1}{2}\iiint s_H \cdot |T|^2 \, dv \tag{1.2-12}$$

Multiplying Eq. (1.2-12) with $1 - k_H^2$, then subtracting it from Eq. (1.2-9) yields,

$$W_{Total} = \frac{1}{k_H^2}\frac{1}{2}\iiint \frac{|B|^2}{\mu_T} dv = \frac{1}{k_H^2} W_B \tag{1.2-13}$$

The magnetomechanical coupling figure of merit k_H^2 defined by Eq. (1.2-7) thus has a very clear physical meaning as the maximum ratio of the mechanical energy input that is transferred to magnetic energy and stored in the form of magnetic flux density. It thus carries a fundamental limit of $k_H^2 \leq 1$ to obey the energy conservation. Similar discussions can be carried out to describe the stored energy in a piezoelectric system and the mechanical to electric energy transfer relation.

1.2.3 Strain-mediated Radiation

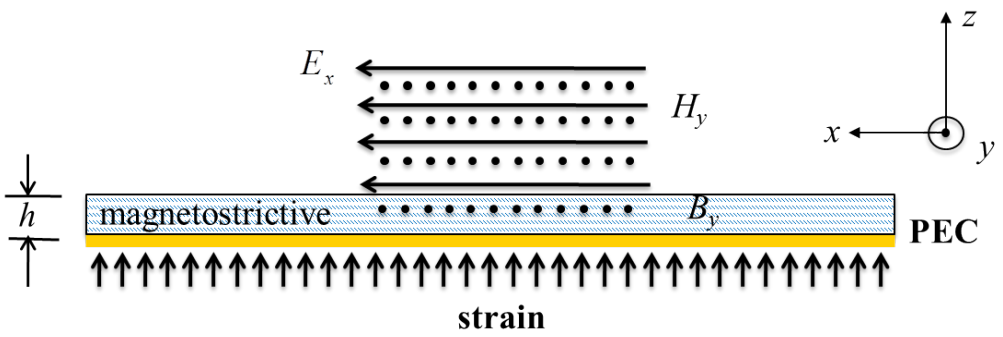

Figure 1.2-2. Strain mediated radiation in the magnetostrictive layer. The coordinate system is chosen such that the magnetic flux is in the *y* direction. The thickness of the substrate satisfies the condition $\boldsymbol{\mu_r k_0 h = 1}$.

The essence of the proposed strain mediated antenna is to create dynamic magnetic flux that is parallel to a conducting plane so that electromagnetic wave radiation can be formed away from the conducting plane. The dynamic magnetic flux replaces the typical conductive current to be the source of radiation in this case. As the platform effect of the conventional current based antennas is associated with the excessive energy stored on the platform manifested as elevated radiation *Q* factors, the performance bound of the proposed antenna must also be examined in regard to its radiation *Q* factor. To derive such a performance bound, a thin layer of magnetostrictive material on a perfect electrically conducting (PEC) ground plane excited under a vertical dynamic strain is assumed and depicted in Figure 1.2-2. The structure is assumed to be homogeneous and extending to infinity in the horizontal directions. In Figure 1.2-2, it is assumed that the dynamic strain is coupled through the ground plane and transferred uniformly onto the magnetostrictive layer. The dynamic strain excites a uniform dynamic magnetic flux within the

layer of magnetic material. According to Faraday's law, this dynamic magnetic flux generates a dynamic electric field that is linearly varying along the thickness dimension until it reaches above the surface of the magnetostrictive layer where an aperture electric field is formed. Denoting the aperture electric field by E_0 and the average radiated power of the electromagnetic wave is thus calculated to be,

$$P_{rad} = \frac{1}{2\eta_0} \iint_S |E_0|^2 \, ds \tag{1.2-14}$$

Using Faraday's law $|B| = |E_0|/(\omega h) = |E_0|/(ck_0 h)$ where c is the speed of light and k_0 is the free space wave number, the stored energy in the form of magnetic flux density in the magnetostrictive layer is thus derived to be:

$$W_B = \frac{1}{2} \iint_{0<z<h} \frac{|B|^2}{\mu_T} dv \approx \frac{h}{2(\omega h)^2 \mu_T} \iint_S |E_0|^2 \, ds \tag{1.2-15}$$

The total stored energy includes an additional component in the form of mechanical stress as evidenced by Eq. (1.2-9). Joining the free space radiation boundary condition $H = E_0/\eta_0 = E_0/c\mu_0$, and Faraday's law, it is not difficult to show that the weak magnetic field condition $|H| \ll |B|/\mu_T$ holds when $\mu_r k_0 h \ll 1$. The total stored energy can thus be well represented by Eq. (1.2-13). The radiation quality factor is thus derived as Eq. (1.2-13) is substituted in,

$$Q_{bound} = \omega \frac{W_{Total}}{P_{rad}} = \omega \frac{W_B/k_H^2}{P_{rad}} = \frac{1}{k_H^2} \frac{1}{\mu_r k_0 h} = \frac{s_H}{d_H^2} \frac{\mu_0}{k_0 h} \tag{1.2-16}$$

Equation (1.2-16) actually represents the lower bound of the radiation Q factor for the proposed strain mediated antenna when the stored energy on the magnetostrictive layer is the primary form of the stored energy. The stored energy considered for the above derivation

includes neither that in the near field above the antenna structure, nor that stored in the feeding structure underneath the ground plane. A complete antenna may involve stored energy in other parts and consequentially a higher radiation quality factor may emerge. On the other hand, it is evident in Eq. (1.2-16) that the lower bound of the radiation Q factor decreases with higher permeability and higher mechanical-to-magnetic coupling factor k_H^2 of the magnetostrictive material. The concept of utilizing high permeability magnetic material to lower the radiation quality factor is consistent with the approaches attempted in [34-36]. The strain mediated multiferroic approach can have further benefit by exploiting other features such as absence of Ohmic loss associated with the current conduction and ease of impedance matching in the vertical direction through acoustic wave resonances.

1.2.4 BAW Mediated Multiferroic Antennas

The structure of BAW resonator is exploited here to create dynamic strain and to couple it to the radiating element. BAW resonators based on either Bragg reflectors or Film Bulk Acoustic Resonance (FBAR) architectures have been extensively used by the RF filter society to create high performance, low loss RF filters with small form factors [59]. Here, the vertical stress and strain profile of BAW at resonance is leveraged to couple the dynamic strain from the piezoelectric phase to the magnetostrictive phase, while in the other two horizontal dimensions the ability of scaling the radiating elements is retained to satisfy certain impedance and gain requirements in practical antenna applications.

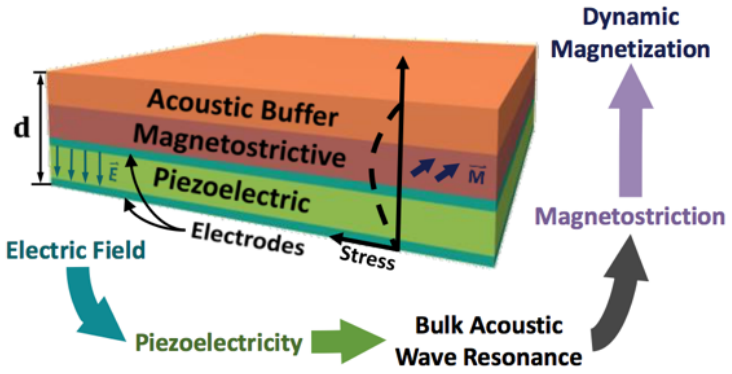

(a)

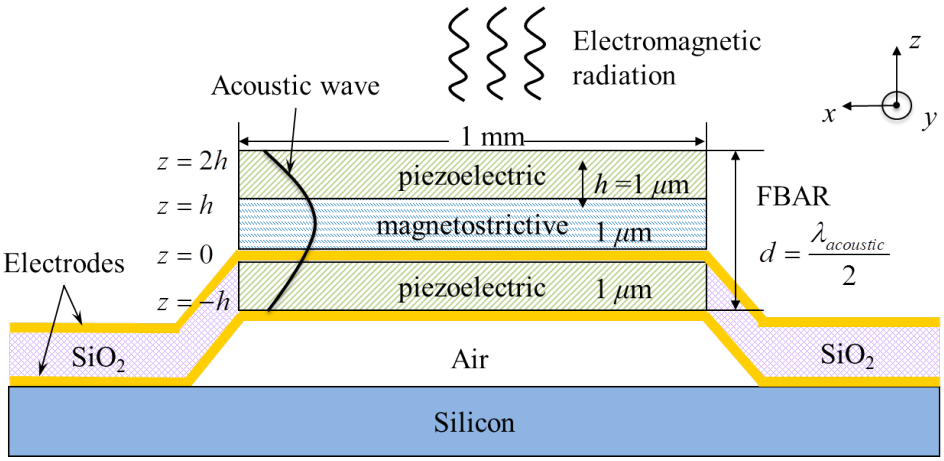

(b)

Figure 1.2-3. BAW resonance based antenna. **a.** Structure and physical coupling mechanism [60]. **b.** Cross section of the antenna. Electric current excitation is applied to the electrodes on both sides of the bottom piezoelectric layer, and it triggers the BAW resonance through converse piezoelectric effect.

Shown in Figure 1.2-3 is the proposed multiferroic antenna operating in the proximity of 1 GHz, which consists of a three-layer strain mediated BAW structure. An air cavity such as those in FBAR is placed underneath the layered structure to overcome the mechanical clamping effect of the substrate. The three layers include a 1-μm-thick magnetostrictive layer sandwiched by two 1-μm-thick piezoelectric layers. The bottom piezoelectric layer serves as the excitation layer, which accepts a current injection and excites the acoustic wave into the layered structure. BAW resonance is thus formed along the vertical direction when the total vertical dimension is approximately a half-acoustic-wavelength. For example, a total of 3-μm-thick layered structure allows BAW resonance at approximately 1 GHz to be established.

At the fundamental resonant mode, the half-period sinusoidal stress profile is plotted in Figure 1.2-3, which is maximized in the middle portion where the magnetostrictive layer is. This allows the maximum strain to be imposed on the magnetostrictive layer for the purpose of generating a strong dynamic magnetic flux. To analyze the radiation quality factor of this structure, the energy stored in the complete sandwiched structure must be considered which includes energy stored in both the magnetostrictive and piezoelectric phase. Due to the open circuit excitation to the piezoelectric layer ($D = 0$) after the initial current pulse drive and the weak magnetic field condition from the magnetostrictive layer ($|H| \ll \frac{|B|}{\mu_T}$ or $H \approx 0$), the exchange of electric energy and magnetic energy with the outside world is negligible compared to the stored energy. The stored energy can thus be represented by the total mechanical energy stored in the form of constant electric flux density stress in piezoelectric material and constant magnetic field stress in magnetostrictive material as shown in Eq. (1.2-12).

$$W_{Total} = \frac{1}{2}\iiint_{-h<z<0\ \&\ h<z<2h} s_D|T|^2\,dv + \frac{1}{2}\iiint_{0<z<h} s_H|T|^2$$

$$= 2W_{PE} + W_{PM} \tag{1.2-17}$$

where W_{PE} and W_{PM} are the stored mechanical energy in each of the piezoelectric layer and magnetic layer. If the mechanical compliance of the piezoelectric layer is approximately the same of that in the magnetostrictive layer, the stored energy in these two phases are proportionally related by the vertical stress profile in the structure at the resonance. Given the stress field distribution of $T = T_0 \sin(2\pi z/\lambda_{ac})$ and the resonance condition $\lambda_{ac} = 2d = 6h$ where λ_{ac} is the wavelength of the acoustic wave, the total stored mechanical energy in the magnetic layer is thus,

$$W_{Total} = \frac{1}{2}\iiint_{-h<z<2h} s_H|T|^2\,dv$$

$$= \frac{1}{2}s_H T_0^2 \cdot A \cdot \int_0^d \sin^2\left(\frac{2\pi}{\lambda_{ac}}z\right)dz$$

$$= \frac{1}{2}s_H T_0^2 \cdot A \cdot \frac{\lambda_{ac}}{2\pi}\int_0^\pi \sin^2(x)\,dx$$

$$= \frac{3}{2}W_{TU} \tag{1.2-18}$$

where A is the surface area of the BAW structure and W_{TU} is the stored energy calculated based on an uniform strain distribution just as the one obtained from Eq. (1.2-12),

$$W_{TU} = \frac{1}{2}s_H T_0^2 \cdot A \cdot h \tag{1.2-19}$$

In addition to the elastic energy stored in the form of mechanical stress, the energy in an acoustic resonator should include an equal amount of kinetic energy. The radiation quality factor of the BAW structure is thus derived,

$$Q_a = \omega \frac{2W_T}{P_{rad}} = \omega \frac{3W_{TU}}{P_{rad}} = 3Q_{bound} \tag{1.2-20}$$

and Q_{bound} is the lower bound of the radiation Q given by Eq. (1.2-16).

1.3 Motivation

The state of the art in modeling RF magnetic components is significantly lagging those consisting of only electric material, with most of commercial software being limited to modeling simple material behavior with defined material dispersion and anisotropy, i.e. applying permittivity and permeability tensor as the constitutive relation, which is not representative of material response in actual hardware. In addition, the modeling approaches currently being used often rely on very coarse scale in relation to the wavelength of the operating frequency due to intrinsic stability requirements present in their programs. Yet applications of thin or thick magnetic film components are thriving thanks to the maturing of nanofabrication technologies such as sputtering or deposition techniques. High quality films are readily available with thickness dimensions in the order of 1/1000th to 1/10000th of the wavelength, ranging from a few μm to a few tens of μm that could be beneficial to developing advanced antennas and filters even at the low GHz frequencies. While the materials are available, the dramatic scale difference cannot be adequately addressed with commercial software due to the overwhelming computational complexity in both space and time gridding. Modeling challenges are exacerbated by the fact that available numerical software programs lack coupled electrodynamic, micromagnetic, and elastodynamic solvers/solutions.

We aim to attack this grand challenge through development of a multi-physics, multi-scale time-domain solver that can model the five orders of magnitudes scale difference from

micrometers to centimeters, including the physics from electromagnetic waves, acoustic waves to micromagnetics into one unified framework. The ultimate goal of this work is to provide a comprehensive and precise modeling solution for dynamic magnetics. Furthermore, we focus on providing a computation platform that is numerically affordable in comparison to existing commercial software.

1.4 Dissertation Outline

In this dissertation, we will present two closely related projects on the development, validation and application of the MUST algorithm. In Chapter 2, we will first present the details of the proposed algorithm in both 1-D and 3-D framework, including both the overall mathematical formulation and the special treatment of material boundaries. In particular, in the 3-D framework, magnetization at the interface between different materials is handled with full consideration of demagnetization. Then we use two numerical examples to demonstrate both the accuracy and efficiency of the proposed method. Furthermore, the ability of magnetic thin films on eliminating the radiation platform effect is explored with physical insight. In Chapter 3, we propose an antenna structure consists of a sandwich of two layers of piezoelectric material and one layer of magnetostrictive material and it relies on BAW resonances to transfer the dynamic strain across different layers. Analyses show that, the radiation quality factor can be significantly lowered with high permeability and a high magnetomechanical coupling figure of merit in the magnetostrictive material, which could lead to low profile antennas with high radiation efficiency. We also implemented the multi-physics and multi-scale modeling tool that was developed in Chapter 2 to emulate the dynamic, two-way interactions between electromagnetic waves and acoustic waves. It is concluded that a multiferroic antenna can be built with a

thickness of only a few micrometers above a conducting plane provided the relative permeability of the magnetic material can reach to a few thousands and the magnetomechanical coupling figure of merit is greater than 85%. Finally, a brief discussion and conclusion will be given in Chapter 4, followed by an outlook of future research work.

Chapter 2

Multiscale, Unconditionally Stable Multiphysics Time-Domain (MUST) Algorithm

In the multiphysics problem involved in ferromagnetic RF devices, dynamic Maxwell's equations (2.0-1) and the LLG equation (2.0-2) must be considered, shown respectively as the following:

$$\nabla\times\boldsymbol{H} = \epsilon\frac{\partial \boldsymbol{E}}{\partial t} + \boldsymbol{J} + \sigma\boldsymbol{E}, \nabla\times\boldsymbol{E} = -\frac{\partial \boldsymbol{B}}{\partial t}, \tag{2.0-1}$$

$$\frac{\partial \boldsymbol{M}}{\partial t} = \mu_0\gamma(\boldsymbol{M}\times\boldsymbol{H}) - \frac{\alpha}{|\boldsymbol{M}|}\boldsymbol{M}\times\frac{\partial \boldsymbol{M}}{\partial t}, \tag{2.0-2}$$

where the gyromagnetic ratio is $\gamma = -1.759\times10^{11}C/kg$, and the magnetic damping constant is $\alpha = \mu_0\gamma\Delta H/4\pi f_t$, with ΔH being the FMR linewidth and f_t the frequency at which the linewidth is measured. Due to strong coupling of magnetization to the EM field, a useful modeling tool should solve Eq. (2.0-1) and Eq. (2.0-2) in a simultaneous manner, instead of considering them as two separate systems. Therefore, iterating through all the physics in each time step is necessary. Furthermore, the thicknesses of magnetic thin films are mostly on the micrometer level, which is 10^5 times smaller than the EM wavelength at GHz frequencies. Also, some possible additional physics require a drastically smaller spatial scale than the EM wavelength. For example, the exchange coupling between spins functions within nanometer distances. Both these two factors lead to tremendous computational load. Finally, under strong magnetization, the field boundary conditions are no longer automatically incorporated by conventional Yee's spatial meshing, because of the demagnetization effect intrinsically presented

by the magnetic field intensity and magnetic flux. To summarize, there are three major challenges to model interactive micromagnetics and EM waves, which are:

1) Coupling between Maxwell's equations and the LLG equation in each time step,
2) Scale disparity of the multiphysics,
3) Demagnetization.

In the 1-D scheme, the challenges are overcome by spatial extrapolation. In the 3-D scheme, the first two challenges are overcome by ADI-FDTD with spin dynamics modification, and the third one by rigorous magnetic material meshing and boundary conditions.

2.1 One-dimensional Multiscale FDTD with Unknown Reduction

A one-dimensional (1-D) FDTD algorithm is developed to model current radiations off the thin-film ferrite coated ground plane, which takes care of the dual-way interactions between the magnetization and electromagnetic field. The equation of motion of electron spin, also known as the Landau-Lifshitz-Gilbert (LLG) equation is coupled with Maxwell's equations to model the dispersive nature of the magnetization and the loss mechanism due to hysteresis. Both the ferromagnetic resonances (FMR) and radiation of electromagnetic wave caused by the dynamic magnetic field are simulated.

2.1.1 1-D Unknown Reduction Through Spatial Extrapolation

Figure 2.1-1 shows the thin-film ferrite antenna structure. The thickness of the film is $d = 1\ \mu m$. The dimension of the film is assumed to be infinitely large in the horizontal plane so that the 1-D approximation is valid. A static magnetic field bias $\boldsymbol{H}_0$ and a dynamic current excitation are applied in the y direction, so that dynamic magnetic field is generated in the x direction and

the z direction. In Figure 2.1-1, the term M_S is the saturation magnetization, $\boldsymbol{m}$ is the AC magnetization caused by $\boldsymbol{h}$. This dynamic magnetization modeling will solve the Maxwell's equations and LLG equations simultaneously as both the magnetic moment and electromagnetic coupling phenomena exist physically and inseparably in the ferrite. With the small signal approximation, Eq. (2.0-1) is expanded in the following scalar form [15]:

$$\frac{1}{\mu_0}\frac{\partial b_z}{\partial t} - \frac{\partial h_z}{\partial t} = \gamma[H_0 b_x - \mu_0(M_S + H_0)h_x] + \alpha\left[\frac{1}{\mu_0}\frac{\partial b_x}{\partial t} - \frac{\partial h_x}{\partial t}\right], \tag{2.1-1}$$

$$\frac{1}{\mu_0}\frac{\partial b_x}{\partial t} - \frac{\partial h_x}{\partial t} = \gamma[-H_0 b_z + \mu_0(M_S + H_0)h_z] - \alpha\left[\frac{1}{\mu_0}\frac{\partial b_z}{\partial t} - \frac{\partial h_z}{\partial t}\right], \tag{2.1-2}$$

$$b_y = \mu_0 h_y. \tag{2.1-3}$$

Enforcing 1-D approximation to Eq. (2.0-2) reduces the Maxwell's equations to

$$\frac{\partial b_x}{\partial t} = \frac{\partial e_y}{\partial z},\ e_z = 0,\ b_z = 0 \tag{2.1-4}$$

which further simplifies Eq. (2.1-1) and Eq. (2.1-2) into

$$-\frac{\partial h_z}{\partial t} = \gamma[H_0 b_x - \mu_0(M_S + H_0)h_x] + \alpha\left[\frac{1}{\mu_0}\frac{\partial b_x}{\partial t} - \frac{\partial h_x}{\partial t}\right], \tag{2.1-5}$$

$$\frac{1}{\mu_0}\frac{\partial b_x}{\partial t} - \frac{\partial h_x}{\partial t} = \gamma[\mu_0(M_S + H_0)h_z] - \alpha\frac{\partial h_z}{\partial t}. \tag{2.1-6}$$

In time domain numerical modeling, the stability condition between the spatial grid and the time step is $\max(\Delta x, \Delta y, \Delta z) \geq c\Delta t/\sqrt{3}$ to stabilize the iteration process. If the antenna works at 1 GHz, the ratio of the wavelength and the structure dimension is $\lambda/h = 3\times10^5$, thus even though the whole structure occupies only one spatial grid, the duration of one time step has to be no larger than $\Delta t_{max} = 6\times10^{-15}s$. If a time window of $10^{-9}s$ should be simulated, the number of time steps is almost one million, which is enormous data. To avoid this stability problem, the following polynomial spatial expansion of electromagnetic field is used:

$$e_y = e_{y1}z,\ h_x = h_{x0}, b_x = b_{x0} \tag{2.1-7}$$

where e_{y1}, h_{x0} and b_{x0} are unknowns to be solved. With the spatial expansion, the stability issue is cleverly avoided, and the simulation will be much less time and storage consuming. Therefore, the radiation boundary condition

$$\left.\frac{E_y}{H_x}\right|_{z=d} = \eta_0 \tag{2.1-8}$$

yields

$$e_{y1} = -\frac{\eta_0}{d}\left(h_{x0} + J_y\right) \tag{2.1-9}$$

where J_y is the surface current excitation. Substituting Eq. (2.1-4) and Eq. (2.1-9) into Eq. (2.1-5) and Eq. (2.1-6) gives

$$\frac{\partial b_{x0}}{\partial t} = -\frac{\eta_0}{d}\left(h_{x0} + J_y\right) \tag{2.1-10}$$

$$-\frac{\partial h_z}{\partial t} = \gamma H_i b_{x0} - \gamma\mu_0(M_S + H_0)h_{x0} - \frac{\alpha\eta_0}{d\mu_0}\left(h_{x0} + J_y\right) - \alpha\frac{\partial h_{x0}}{\partial t} \tag{2.1-11}$$

$$-\frac{\eta_0}{d\mu_0}\left(h_{x0} + J_y\right) - \frac{\partial h_{x0}}{\partial t} = \gamma\mu_0(M_S + H_0)h_z + \alpha\frac{\partial h_z}{\partial t} \tag{2.1-12}$$

The time difference equations are obtained by discretizing Eq. (2.1-10)–Eq. (2.1-12), as follows:

$$k_1 \cdot h_{x0}^n = k_2 \cdot h_{x0}^{n-1} - \left(\alpha + \frac{1}{\alpha}\right)\frac{\eta_0}{\mu_0 d}\frac{J_y^n + J_y^{n-1}}{2} - \frac{\gamma}{\alpha}(M_S + H_0)\mu_0 h_z^{n-\frac{1}{2}} + \gamma H_0 b_{x0}^{n-\frac{1}{2}} \tag{2.1-13}$$

$$b_{x0}^{n-\frac{1}{2}} = -\frac{\eta_0\Delta t}{d}\left[h_{x0}^n + J_y^n\right] + b_{x0}^{n-\frac{1}{2}} \tag{2.1-14}$$

$$k_3 \cdot h_z^{n+\frac{1}{2}} = k_4 \cdot h_z^{n-\frac{1}{2}} - \gamma H_0\frac{b_{x0}^{n+\frac{1}{2}} + b_{x0}^{n-\frac{1}{2}}}{2} - \gamma\mu_0(M_S + H_0)h_{x0}^n \tag{2.1-15}$$

where

$$k_{1,2} = \left(\frac{\eta_0}{2\mu_0 d} + \frac{1}{\Delta t}\right)\left(\alpha + \frac{1}{\alpha}\right) \pm \frac{\gamma\mu_0(M_S + H_0)}{2} \tag{2.1-16}$$

$$k_{3,4} = \frac{(\alpha^2+1)}{\Delta} \pm \frac{\alpha\gamma\mu_0(M_S+H_0)}{2} \tag{2.1-17}$$

A surface electric current density in the form of Gaussian pulse $J_y = \exp[-(t-t_0)^2/2\tau]$ is applied to the thin film, as the excitation to the recursive FDTD time-marching algorithm. The leap-frog time stepping scheme can be implemented by solving the aperture dynamic component h_{x0}, coupled back to update the magnetic flux density and then to update the other magnetic field component h_z. The ferrite material is chosen to be yttrium iron garnet (YIG), with $4\pi M_S = 1750\ Gauss$, $\Delta H = 5\ Oe$, $\epsilon_r = 13$.

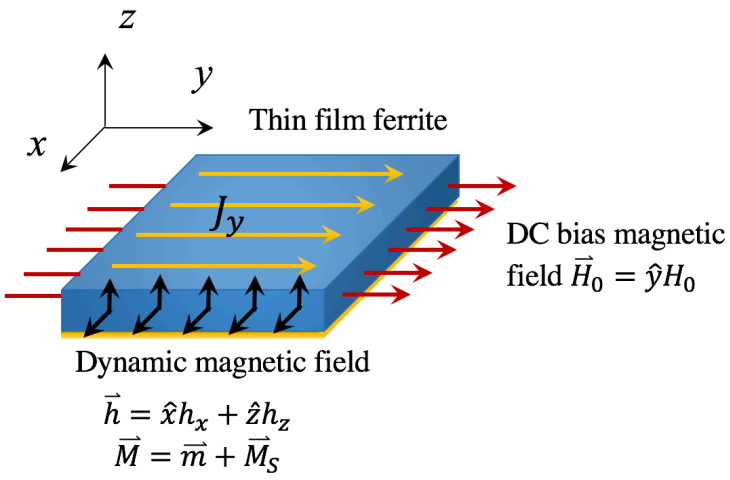

Figure 2.1-1. Infinite magnetic thin film backed by PEC ground plane, on which a uniform electric current sheet $\boldsymbol{J_y}$ is placed.

2.1.2 Simulation Results

The relative permeability curves shown in Figure 2.1-2 are obtained by the ratio of the frequency domain fields, which are computed using the fast Fourier transform of the time domain field. The analytical results are computed based on [6]:

$$\omega_0 = \mu_0 \gamma H_0 + j\alpha\omega, \chi = \frac{\omega_m(\omega_m+\omega_0)}{[\omega_0(\omega_m+\omega_0)-\omega^2]} \quad (2.1\text{-}18)$$

where $\mu_0 \gamma H_0$ is the precession frequency, and $\omega_m = \mu_0 \gamma M_S$. The FMR is shifted to higher frequencies as the DC magnetic bias increases. A very good agreement between the simulated results and the analytical results can be observed in Figure 2.1-2. The normalized radiated power into free space (shown by Figure 2.1-3) increases as the thickness of the film increases or the line width of the material decreases. It should be noted that the radiated power is maximum at FMR, where the magnetic loss tangent reaches its peak and the relative permeability is nearly zero. This phenomenon was not predicted prior to this research. It can be explained that near FMR region, the ferrite becomes a good magnetic conductor so that dynamic electromagnetic fields could hardly stand inside the material, which results in high power released into the free space. This conclusion opens up a new antenna design strategy to make the antenna work at FMR to enhance the radiation.

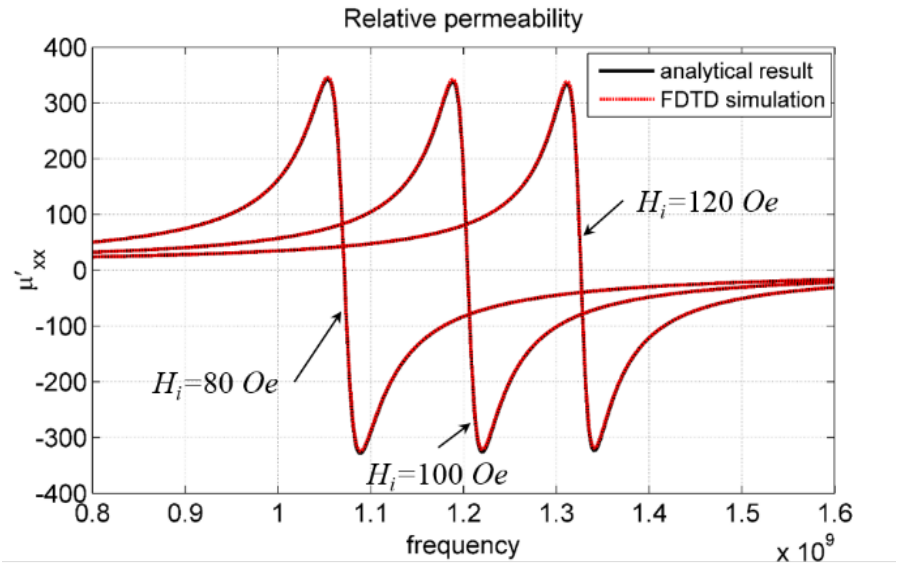

(a)

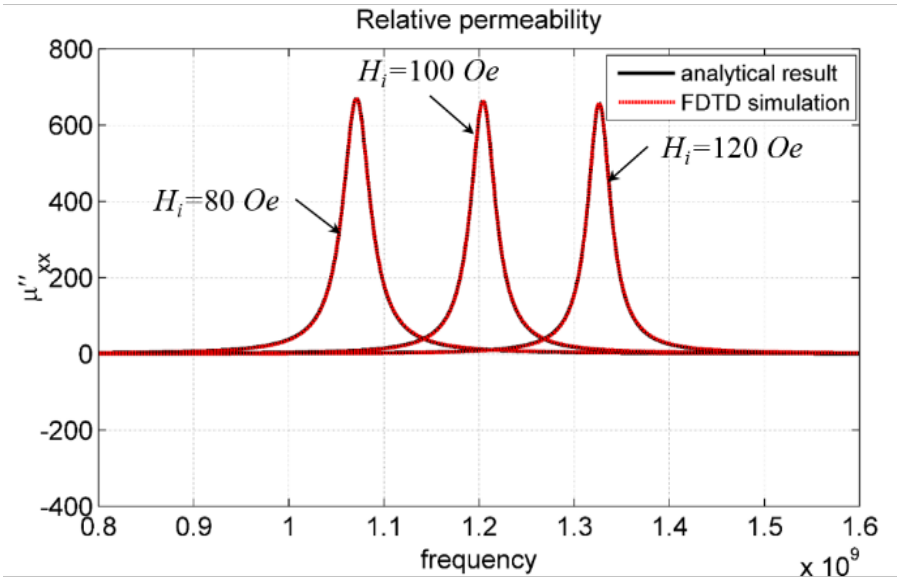

(b)

Figure 2.1-2. Relative permeability with different DC magnetic bias, $\boldsymbol{\Delta H = 50\ Oe}$. **a.** Real part $\boldsymbol{\mu'}$. **b.** Imaginary part $\boldsymbol{\mu''}$.

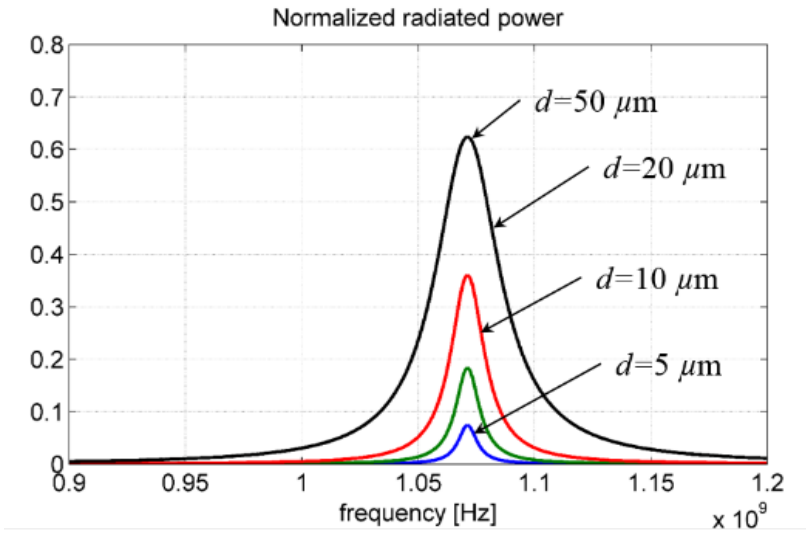

(a)

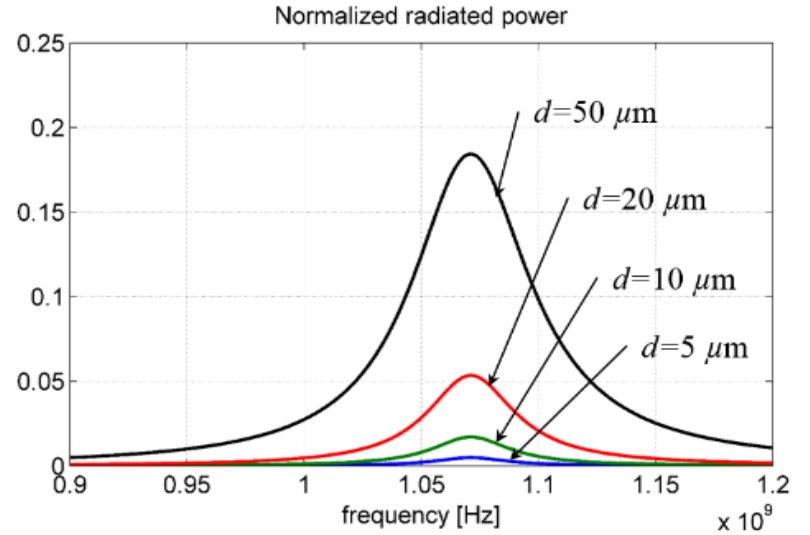

(b)

Figure 2.1-3. Normalized radiated power of the thin film ferrite. **a.** $\boldsymbol{\Delta H = 1\ Oe}$, **b.** $\boldsymbol{\Delta H = 5\ Oe}$.

2.2 Three-dimensional Unconditionally Stable Multiphysics FDTD

We propose for the first time an efficient and accurate modeling, simulation and design tool for multiphysics problems that encompasses the fields of electrodynamics and micromagnetics. The proposed modeling is based on a modified alternating-direction-implicit FDTD (ADI-FDTD) method. We will introduce the details of the algorithm, including both the mathematical formulation and boundary conditions. Magnetization at the interface between different materials is handled with full consideration of demagnetization. Numerical examples have demonstrated both the accuracy and efficiency of the proposed method. First, an E-plane ferrite resonance isolator is simulated and compared to the commercial capability. The agreement of the simulated performance proves the accuracy of this work. Second, as a further validation of the proposed modeling, the simulated permeability of an infinite YIG thin film matches theoretical prediction. We will also show a demonstration of potential application of the proposed modeling tool. The effect of magnetic thin film to eliminate the platform effect is explored with insight. The radiation performance of magnetic thin film loaded current source is shown under various magnetic DC bias, and is three orders of magnitude higher than that without magnetic thin film.

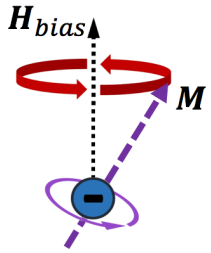

Figure 2.2-1. Electron angular momentum about its own central axis (called spin) leads to a magnetic moment $\boldsymbol{M}$ precessing around the applied magnetic field $\boldsymbol{H_{bias}}$. The spin of magnetization results in the intrinsic coupling between different magnetic field components orthogonal to the bias [60].

2.2.1 Introduction to ADI FDTD

Zheng, Chen and Zhang (ZCZ) reported an ADI time-stepping algorithm for FDTD that has theoretical unconditional stability for the general 3-D case steps [22, 24], with detailed theoretical stability analysis. While the ZCZ ADI technique uses the same Yee space lattice, the six field vector components are collocated rather than staggered in time. Figure 2.2-2 interoperates the procedure of updating the E field in both the conventional FDTD and ADI FDTD. In conventional FDTD, the field is directly advanced from one time step to the next one, without the knowledge of the field value at a half time step. However, the ADI scheme iterates the field variable forward in time for half a time step and then backward for another half a time step to derive implicit relations among the field variables in the new time step as a function of that in the prior time steps.

Original ADI FDTD expands Eq. (2.0-1) into Eq. (2.1-1), with *E* and *H* fields collocated temporally. In Eq. (2.1-1), $\boldsymbol{M}_i$ are the tridiagonal matrices, and F_i^n are the functions of *E* and *H* fields at time-step (n) and $F_i^{n+1/2}$ at $(n+1/2)$ [22-24].

$$\begin{bmatrix} \boldsymbol{M}_1 & 0 & 0 \\ 0 & \boldsymbol{M}_2 & 0 \\ 0 & 0 & \boldsymbol{M}_3 \end{bmatrix} \begin{bmatrix} E_x^{n+\frac{1}{2}} \\ E_y^{n+\frac{1}{2}} \\ E_z^{n+\frac{1}{2}} \end{bmatrix} = \begin{bmatrix} F_1^n \\ F_2^n \\ F_3^n \end{bmatrix},$$

$$\begin{bmatrix} \boldsymbol{M}_4 & 0 & 0 \\ 0 & \boldsymbol{M}_5 & 0 \\ 0 & 0 & \boldsymbol{M}_6 \end{bmatrix} \begin{bmatrix} E_x^{n+1} \\ E_y^{n+1} \\ E_z^{n+1} \end{bmatrix} = \begin{bmatrix} F_4^{n+\frac{1}{2}} \\ F_5^{n+\frac{1}{2}} \\ F_6^{n+\frac{1}{2}} \end{bmatrix}, \tag{2.2-1}$$

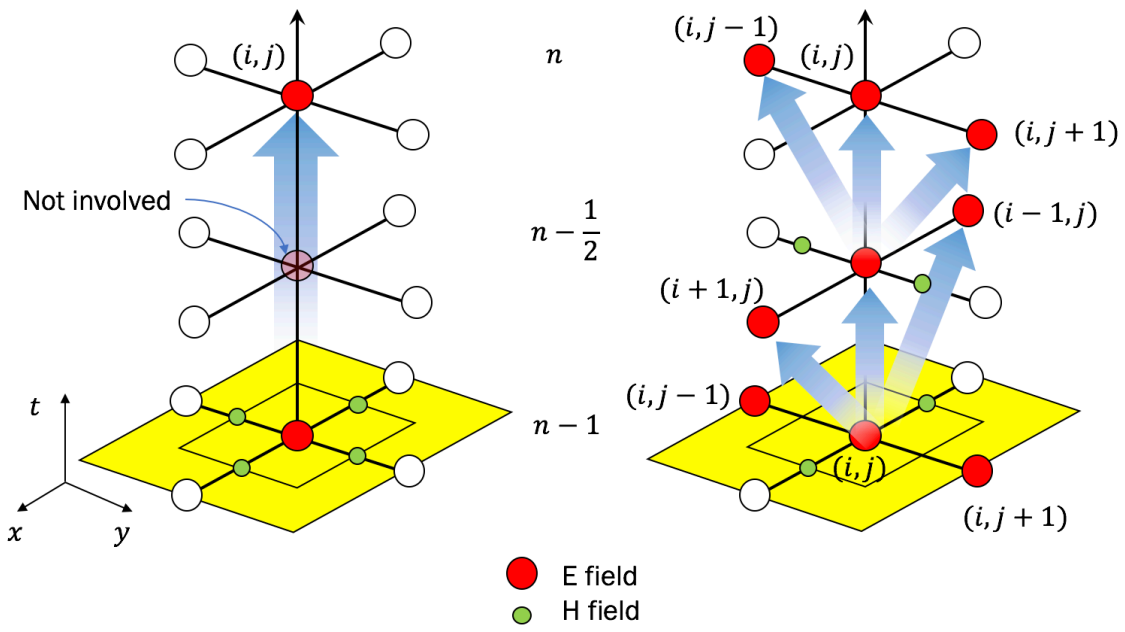

Figure 2.2-2. Stencil figure for the alternating direction implicit method in finite difference equations. Left: conventional FDTD scheme. Right: ADI FDTD scheme.

2.2.2 Formulation of ADI-FDTD with Spin Dynamics

Without loss of generality, we apply a magnetic DC bias field H_i in the in-plane y direction, to saturate the magnetic material so that it presents magneto-dynamic properties, and the magnitude of magnetization is the saturation value M_S. We apply the small signal approximation ($H_y = 0$), as the typical case in RF devices. Differentiating Eq. (2.0-2) in a similar manner leads to

$$A_0 H_x^{n+\frac{1}{2}} = A_1 B_x^{n+\frac{1}{2}} + A_2 B_z^{n+\frac{1}{2}} + A_3 B_x^n + A_4 B_z^n + A_5 H_x^n + A_6 H_z^n, \tag{2.2-2}$$

$$A_0 H_z^{n+\frac{1}{2}} = A_1 B_z^{n+\frac{1}{2}} - A_2 B_x^{n+\frac{1}{2}} + A_3 B_z^n - A_4 B_x^n + A_5 H_z^n - A_6 H_x^n, \tag{2.2-3}$$

with $A_0 = \frac{\gamma\mu_0(M_S+H_i)}{2}\left\{\left[\frac{4(\alpha^2+1)}{\gamma\mu_0(M_S+H_i)\Delta t} + \alpha\right]^2 + 1\right\}$,

$$A_{1,3} = \frac{\gamma H_i}{2} + \left[\pm\frac{2(\alpha^2+1)}{\mu_0 \Delta t} + \frac{\alpha\gamma H_i}{2}\right]\left[\frac{4(\alpha^2+1)}{\gamma\mu_0(M_S+H_i)\Delta t} + \alpha\right],\ A_2 = -\frac{2(\alpha^2+1)M_S}{\mu_0\Delta t(M_S+H_i)},$$

$$A_4 = \frac{2(\alpha^2+1)(M_S+2H_i)}{\mu_0\Delta t(M_S+H_i)},\ A_5 = -\frac{\gamma\mu_0(M_S+H_i)(\alpha^2+1)}{2} + \frac{8(\alpha^2+1)^2}{\gamma\mu_0(\Delta t)^2(M_S+H_i)},\ A_6 = -\frac{4(\alpha^2+1)}{\Delta t}.$$

In nonmagnetic material, Eq. (2.2-2) and Eq. (2.2-3) reduce to $H_x = B_x/\mu_0$ and $H_z = B_z/\mu_0$. Similarly, H_x and H_z are advanced from time-step $(n+1/2)$ to $(n+1)$ as in Eq. (2.2-4) and Eq. (2.2-5).

$$A_0 H_x^{n+1} = A_1 B_x^{n+1} + A_2 B_z^{n+1} + A_3 B_x^{n+\frac{1}{2}} + A_4 B_z^{n+\frac{1}{2}} + A_5 H_x^{n+\frac{1}{2}} + A_6 H_z^{n+\frac{1}{2}}, \tag{2.2-4}$$

$$A_0 H_z^{n+1} = A_1 B_z^{n+1} - A_2 B_x^{n+1} + A_3 B_z^{n+\frac{1}{2}} - A_4 B_x^{n+\frac{1}{2}} + A_5 H_z^{n+\frac{1}{2}} - A_6 H_x^{n+\frac{1}{2}}, \tag{2.2-5}$$

Substituting Eq. (2.2-2) and Eq. (2.2-3) into the differentiated form of Eq. (2.0-1) results in a modified matrix representation of Eq. (2.2-1):

$$\begin{bmatrix} \boldsymbol{M}_1' & \boldsymbol{N}_1' & 0 \\ \boldsymbol{N}_2' & \boldsymbol{M}_2' & 0 \\ 0 & 0 & \boldsymbol{M}_3 \end{bmatrix} \begin{bmatrix} E_x^{n+\frac{1}{2}} \\ E_y^{n+\frac{1}{2}} \\ E_z^{n+\frac{1}{2}} \end{bmatrix} = \begin{bmatrix} F_1'^n \\ F_2'^n \\ F_3'^n \end{bmatrix},$$

$$\begin{bmatrix} \boldsymbol{M}_4 & 0 & 0 \\ 0 & \boldsymbol{M}_5' & \boldsymbol{N}_5' \\ 0 & \boldsymbol{N}_6' & \boldsymbol{M}_6' \end{bmatrix} \begin{bmatrix} E_x^{n+1} \\ E_y^{n+1} \\ E_z^{n+1} \end{bmatrix} = \begin{bmatrix} F_4'^{n+\frac{1}{2}} \\ F_5'^{n+\frac{1}{2}} \\ F_6'^{n+\frac{1}{2}} \end{bmatrix}, \tag{2.2-6}$$

where $\boldsymbol{M}_i'$ are the modified tridiagonal matrices, with all the $1/\mu$ terms replaced by (A_1/A_0), and $\boldsymbol{N}_i'$ are non-tridiagonal matrices dependent on (A_2/A_0). The terms $F_i'^n$ are the functions of known E and H fields at time-step (n) and $F_i'^{n+1/2}$ at $(n+1/2)$. The major difference between F_i' and F_i comes from the intrinsic coupling between H_x and H_z, as indicated in Figure 2.2-1. For example, F_1^n is a function of E_x^n, E_y^n, H_y^n and H_z^n, while with the LLG equation, H_z is coupled

with H_x; thus, besides the aforementioned four fields, ${F_1'}^n$ is also a function of E_z^n, H_x^n, B_x^n and B_z^n. For clear illustration, the linear forms of Eq. (2.2-6) are shown in Section 2.5. Appendix.

To avoid complicated matrix inversion, let us move the unknowns $\boldsymbol{N}_i' E$ to the right-hand side of Eq. (2.2-6), such that the matrices associated with the desired unknown terms are maintained to be tri-diagonal. Such manipulation leads to:

$$\begin{bmatrix} \boldsymbol{M}_1' & 0 & 0 \\ 0 & \boldsymbol{M}_2' & 0 \\ 0 & 0 & \boldsymbol{M}_3 \end{bmatrix} \begin{bmatrix} E_x^{n+\frac{1}{2}} \\ E_y^{n+\frac{1}{2}} \\ E_z^{n+\frac{1}{2}} \end{bmatrix} = \begin{bmatrix} {F_1'}^n - \boldsymbol{N}_1' E_y^{n+\frac{1}{2}} \\ {F_2'}^n - \boldsymbol{N}_2' E_x^{n+\frac{1}{2}} \\ {F_3'}^n \end{bmatrix},$$

$$\begin{bmatrix} \boldsymbol{M}_4 & 0 & 0 \\ 0 & \boldsymbol{M}_5' & 0 \\ 0 & 0 & \boldsymbol{M}_6' \end{bmatrix} \begin{bmatrix} E_x^{n+1} \\ E_y^{n+1} \\ E_z^{n+1} \end{bmatrix} = \begin{bmatrix} {F_4'}^{n+\frac{1}{2}} \\ {F_5'}^{n+\frac{1}{2}} - \boldsymbol{N}_5' E_z^{n+1} \\ {F_6'}^{n+\frac{1}{2}} - \boldsymbol{N}_6' E_y^{n+1} \end{bmatrix}, \tag{2.2-7}$$

The unknowns on the left-hand side of Eq. (2.2-7) can be solved by only inversion of the tri-diagonal matrices. However, due to the existence of additional unknown terms on the right-hand side, the solution must be amended. In every time-marching step, we update the desired unknowns on the left-hand side by iterating the prior solution of the right-hand side unknowns. For example, in the $(m+1)^{th}$ iteration, $E_y^{n+\frac{1}{2}}$ is recalculated using $E_x^{n+\frac{1}{2}}$ obtained in the m^{th} iteration, until the convergence criterion is reached. In this work, the convergence criterion is set to be: $|\Delta E| = \frac{|E_{m+1} - E_m|^2}{|E_m|^2} < 10^{-6}$. The accuracy of such an iteration process is limited by the ratio of $N_n'/{M_n}'$, which is proportional to $\Delta t \times (A_2/A_1)$. Therefore, to guarantee the accuracy of the modeling, the time-step size Δt and the value of saturation magnetization $4\pi M_S$ should be limited. In typical magnetic materials, $4\pi M_S$ is below 10^5 *Gauss*. Such a value leads to a time-

step size below 10^4 times larger than CFL limit in an RF device composed of micrometer-thick thin films working at GHz range.

2.2.3 Demagnetization and Rigorous Magnetic Material Meshing

Figure 2.2-3a shows the classical Yee's spatial meshing. In conventional FDTD with a scalar permeability representation, for example, $\boldsymbol{B} = \mu \boldsymbol{H}$, the normal $\boldsymbol{B}$ continuity is incorporated automatically without being determined explicitly as FDTD cell is divergence-free. However, in a practical magnetic material setting, the magnetic constitutive relation defined by LLG equation becomes a tensor relation, i.e., $\boldsymbol{B} = \bar{\bar{\mu}} \boldsymbol{H}$. The normal $\boldsymbol{B}$ components on the boundary need to be known to determine all the $\boldsymbol{H}$ components. Therefore, one can only correctly model the demagnetization at the material surface by including the discontinuity of the normal $\boldsymbol{H}$ components and tangential $\boldsymbol{B}$ components over the boundary. This problem is nonnegligible in magnetic material simulations due to the anisotropy and high value of material permeability. Furthermore, large time-step sizes utilized in unconditionally stable algorithm exacerbate this problem, represented by numerical instability. Therefore, conventional FDTD meshing needs to be modified to include the complete set of boundary conditions.

In this work, we solve this problem by rigorous material meshing and field-splitting at the interface, with the former ensuring continuous tangential field intensities and the latter ensuring discontinuous normal field intensities. This is shown in Figure 2.2-3b and Figure 2.2-3c. We follow Yee's spatial allocation of $\boldsymbol{E}$ and $\boldsymbol{H}$ fields, with $\boldsymbol{B}$ overlaying $\boldsymbol{H}$, and the electric property interface and magnetic property interface staggered by half of the spatial cell. Therefore, only tangential fields lie on the interfaces, enforcing tangential field intensity continuity.

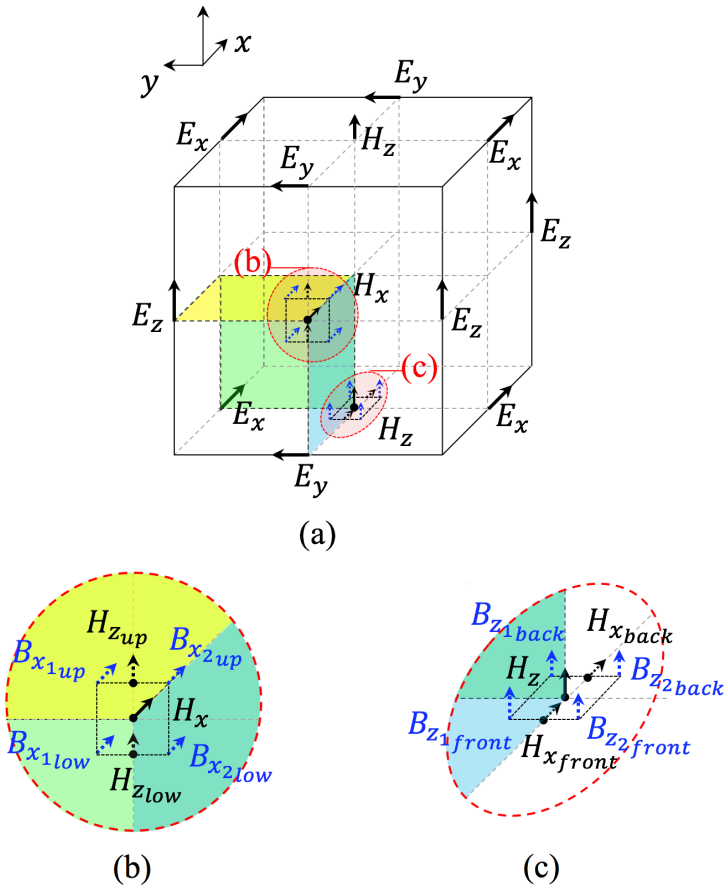

Figure 2.2-3. **a.** Spatial allocation of fields and split fields across magnetic material interfaces (shaded areas), **b.** split fields at y- and z- interfaces, with $\boldsymbol{H_{z_{up}}}$, $\boldsymbol{H_{z_{low}}}$, $\boldsymbol{B_{x1_{up}}}$, $\boldsymbol{B_{x1_{low}}}$, $\boldsymbol{B_{x2_{up}}}$ and $\boldsymbol{B_{x2_{up}}}$ defined on the $\boldsymbol{H_x}$ nodes, **c.** split fields at y- and x- interfaces, with $\boldsymbol{H_{x_{front}}}$, $\boldsymbol{H_{x_{back}}}$, $\boldsymbol{B_{z1_{front}}}$, $\boldsymbol{B_{z1_{back}}}$, $\boldsymbol{B_{z2_{front}}}$ and $\boldsymbol{B_{z2_{back}}}$ defined on the $\boldsymbol{H_z}$ nodes. The positions of these fields are drawn apart for better visibility.

Furthermore, since the tangential $\boldsymbol{H}$ components are coupled to the normal $\boldsymbol{H}$ components by magnetic spin, the calculation of the continuous tangential components requires knowledge of adjacent normal components that might be discontinuous across the interfaces. To handle this issue, the normal $\boldsymbol{H}$ field is split into two separate components, lying on each side of the

interfaces. These two separate $\boldsymbol{H}$ components are unequal across the material interfaces, with an average value of the actual field, e.g., $(H_{z_{up}} + H_{z_{low}})/2 = H_z$. The same technique is applied to the tangential $\boldsymbol{B}$ components which are also discontinuous across the boundaries. However, $\boldsymbol{B}$ is split into four different components, because $\boldsymbol{B}$ is discontinuous across both *z*- and *y*- interfaces. The split fields are calculated individually in the corresponding region using Eq. (2.2-2) and Eq. (2.2-3). For example:

$$A_1 B_{x_{1up}}^{n+\frac{1}{2}} = A_0 H_x^{n+\frac{1}{2}} - A_2 B_{z_{ave}}^{n+\frac{1}{2}} - A_3 B_{x_{1up}}^{n} - A_4 B_{z_{ave}}^{n} - A_5 H_x^n - A_6 H_{z_{up}}^n, \tag{2.2-8}$$

$$A_1 B_{z_{1front}}^{n+\frac{1}{2}} = A_0 H_z^{n+\frac{1}{2}} + A_2 B_{x_{ave}}^{n+\frac{1}{2}} - A_3 B_{z_{1front}}^{n} + A_4 B_{x_{ave}}^{n} - A_5 H_z^n + A_6 H_{x_{front}}^n, \tag{2.2-9}$$

where $B_{z_{ave}}$ and $B_{x_{ave}}$ are spatial interpolation values, calculated by Eq. (2.2-10) and Eq. (2.2-11):

$$\begin{aligned} B_{z_{ave}}\left(i, j+\frac{1}{2}, k+\frac{1}{2}\right) = {} & B_z\left(i+\frac{1}{2}, j+\frac{1}{2}, k\right) + B_z\left(i+\frac{1}{2}, j+\frac{1}{2}, k+1\right) \\ & + B_z\left(i-\tfrac{1}{2}, j+\tfrac{1}{2}, k\right) + B_z\left(i-\tfrac{1}{2}, j+\tfrac{1}{2}, k+1\right), \end{aligned} \tag{2.2-10}$$

$$\begin{aligned} B_{x_{ave}}\left(i+\frac{1}{2}, j+\frac{1}{2}, k\right) = {} & B_x\left(i, j+\frac{1}{2}, k+\frac{1}{2}\right) + B_x\left(i, j+\frac{1}{2}, k-\frac{1}{2}\right) \\ & + B_x\left(i+1, j+\tfrac{1}{2}, k+\tfrac{1}{2}\right) + B_x\left(i+1, j+\tfrac{1}{2}, k-\tfrac{1}{2}\right), \end{aligned} \tag{2.2-11}$$

To summarize, the flow of the proposed multiphysics modeling is as follows:

1) Update $\boldsymbol{E}^{n+1/2}$ using Eq. (2.2-7).
2) Update $\boldsymbol{B}^{n+1/2}$ using differentiated Faraday's law in Eq. (2.0-1).
3) Update $\boldsymbol{H}^{n+1/2}$ using Eq. (2.2-2) and Eq. (2.2-3).

4) Update split fields $H_{z_{up}}$, $H_{z_{low}}$, $B_{x1_{up}}$, $B_{x1_{low}}$, $B_{x2_{up}}$ $B_{x2_{up}}$, $H_{x_{front}}$, $H_{x_{back}}$, $B_{z1_{front}}$, $B_{z1_{back}}$, $B_{z2_{front}}$ and $B_{z2_{back}}$ at time-step $(n + 1/2)$ at the interfaces using Eq. (2.2-8) and Eq. (2.2-9).

5) Repeat Step 1) to Step 4) to advance all the fields to time-step $(n + 1)$.

Without linear spatial interpolation [15], the proposed method is precise and stable even with a large time-step on the order of 10^4 CFL.

2.2.1 Numerical Validation I: E-plane Ferrite Resonance Isolator

Ferrite isolators constructed in rectangular waveguides have become one of the most successful of the nonreciprocal devices because of their versatility [5, 6]. Figure 2.2-4 shows a typical full-height E-plane ferrite isolator structure, with a thin ferrite slab mounted along the E-plane direction which extends along the waveguide longitudinal direction. A DC magnetic bias field is applied along the in-plane direction of the ferrite slab, which saturates the ferrite and sets up a preferential direction of magnetic dipole moments interacting with electromagnetic waves [3]. The circularly polarized field propagating in the magnetized ferrite strongly interacts with magnetic dipole moments in the same direction as the precession, but weakly interacts in the opposite direction of precession. Therefore, the attenuation constants and propagation constants of the field near ferromagnetic resonance are very different in the two propagation directions [5]. As a result, the ferrite isolator could also work as a field displacement phase shifter.

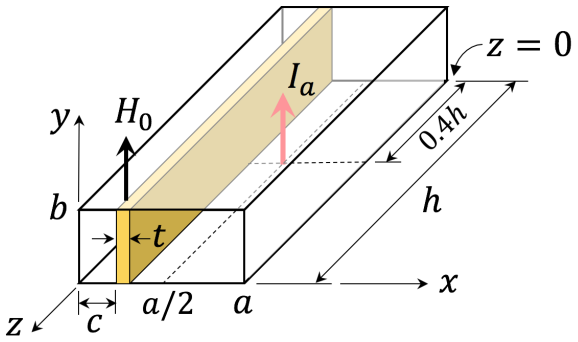

Figure 2.2-4. X-band waveguide with a thin ferrite slab mounted in the E-plane. a = 22.86 mm, b = 11.43 mm, h = 300 mm, c=0.125a, $\boldsymbol{t = 0.5\,mm}$, $\boldsymbol{\epsilon_r = 13}$, $\boldsymbol{4\pi M_S = 1700\,G}$, $\boldsymbol{H_0 = 2840\,Oe}$, $\boldsymbol{\Delta H = 200\,Oe}$, $\boldsymbol{\Delta x = 0.02\,mm}$, $\boldsymbol{\Delta y = 3.387\,mm}$, $\boldsymbol{\Delta z = 0.2\,mm}$. The electric current line source is located at 0.4h.

An X-band ferrite resonance isolator is shown in Figure 2.2-4, with waveguide dimensions of $22.86mm \times 11.43mm \times 300mm$. In the center of the cross section at $z = 0.4h$, a full-height current line source is applied at 10 GHz so that only the TE_{10} mode exists. The E-plane ferrite slab is mounted at $c = 0.125a$, with a thickness of $t = 0.5\,mm$. The slab is YIG, with a dielectric constant being $\epsilon_r = 13$, the saturation magnetization being $4\pi M_S = 1700\,G$, and the FMR linewidth being $\Delta H = 200\,Oe$ [6]. A magnetic DC bias, $H_0 = 2840\,Oe$, is applied in +y direction, leading to an FMR frequency of $f_r = \omega_r/2\pi = 10.05GHz$, where ω_r is calculated by Kittel's equation (2.2-12):

$$\omega_r = \sqrt{\omega_{0_0}(\omega_m + \omega_{0_0})} \quad (\hat{y}\text{ bias}). \tag{2.2-12}$$

where $\omega_{0_0} = \mu_0 \gamma H_0$ and $\omega_m = \mu_0 \gamma M_S$ in SI units.

In this case, the spatial resolution is $0.02\times3.387\times0.2\ mm$ ($\Delta x\times\Delta y\times\Delta z$). The time-step is 50 times the CFL ($\Delta t_{CFL} = 3.8591\times10^{-14}s$), to keep the sampling frequency below the Nyquist rate. The excitation is a modified Gaussian pulse $J_{Sy} = e^{-(t-3T)^2/2T^2}\cos(\omega_0 t)$, with $T = 2/f_0$ and $f_0 = 10\ GHz$.

The simulated E_y field at 10 GHz shown in Figure 2.2-5 validates the theoretical prediction. As can be seen, E_y attenuates rapidly in –z direction and slowly in the +z direction. With the magnetic DC bias H_0 applied in the +y direction, the EM wave propagating in the –z direction is polarized in the same rotation of the magnetic spin, and thus presents large attenuation near ferromagnetic resonance. Ideally, the EM wave propagating in +z direction does not interact with the magnetic spin. However, due to demagnetization, the EM field is not perfectly circularly polarized and is slightly disturbed by the ferrite, presenting a low attenuation constant.

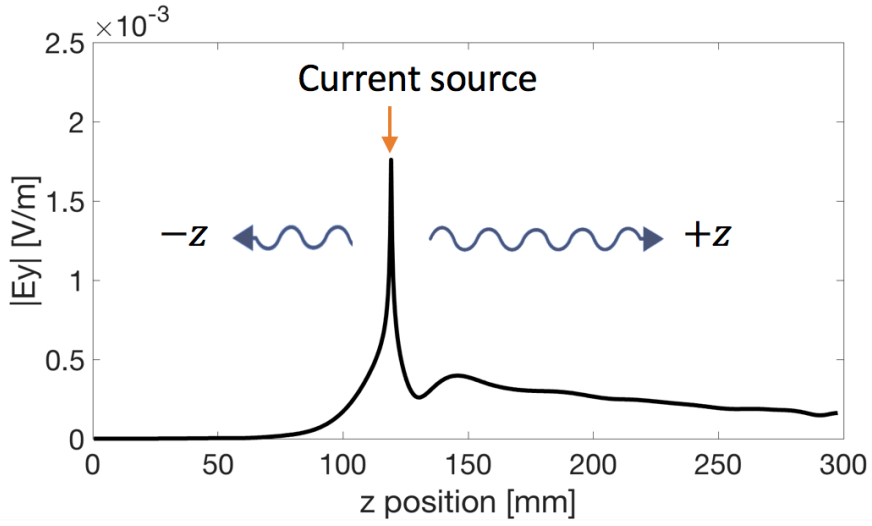

Figure 2.2-5. $\boldsymbol{E_y}$ field distribution at 10 GHz along z direction at the center of cross section, $\boldsymbol{x = a/2}$ and $\boldsymbol{y = b/2}$.

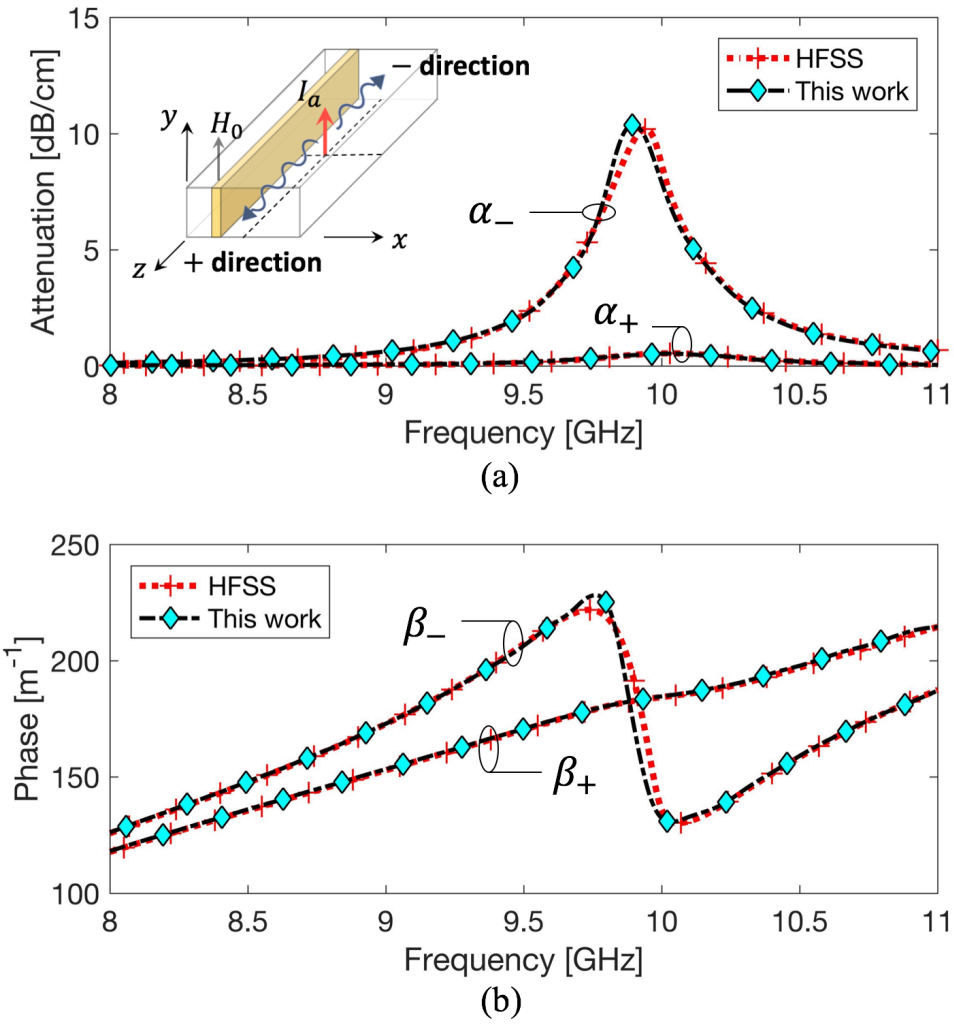

Figure 2.2-6. a. Attenuation constants and **b.** phase constants of forward and reverse propagation direction for the resonance isolator specified by Figure 2.2-4**.**

Attenuation constants and phase constants are derived from the simulated frequency-domain E_y field by extracting the damping speed of the field magnitude and the variation speed of the phase, with the signal processing code ESPRIT [61, 62], as shown in Figure 2.2-6. The agreement between the commercial software and the proposed method validates the accuracy of

this work, while the fully coupled algorithm provides readiness for expansion of physics, such as eddy current loss, crystalline anisotropy, and exchange coupling between spins. Furthermore, the proposed fully coupled modeling has the capability of simulating and designing very electrically small devices and devices with very large form factor.

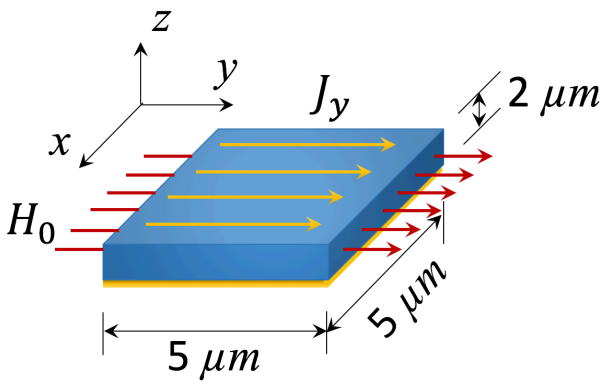

Figure 2.2-7. Infinite YIG thin film backed by PEC ground plane, on which a uniform electric current sheet $\boldsymbol{J_y}$ is placed. The film has a thickness of $\boldsymbol{2\ \mu m}$ and it is magnetized by $\boldsymbol{H_0}$ in the y direction, which is parallel to the electric current. The four sides of the structure are enclosed by periodic boundaries, leading to an effectively infinite in-plane dimension. The simulation space is $\boldsymbol{5\times5\times60\ \mu m}$ with $\boldsymbol{1\times1\times0.4\ \mu m}$ spatial resolution. The top surface of the simulation space is covered by an absorbing boundary condition.

2.2.2 Numerical Validation II: Magnetic Thin Film Permeability

A continuous current sheet at a distance 2 μm away from a perfect electrical conductor (PEC) with thin-film YIG filled-in between them is simulated, shown by Figure 2.2-7. The simulation space is $5\times5\times60\ \mu m$ with $1\times1\times0.4\ \mu m$ spatial resolution. The outer boundary along

the x and y axes is a periodic boundary, so that the film is equivalently infinite in-plane. The top surface of the simulation space is covered by an absorbing boundary condition. The simulation space is filled with vacuum. The time-step is 5000 times the CFL ($\Delta t_{CFL} = 7.6980\times10^{-16}s$). The surface current excitation is a modified Gaussian pulse $J_{Sy} = e^{-(t-3T)^2/2T^2}\cos(\omega t)$, with $T = 3/f_0$ and $f_0 = 2GHz$. The properties of YIG are applied to the magnetic thin film, i.e. $4\pi M_S = 1700\ Gauss$, $\epsilon_r = 13$, $\sigma = 0$. The thin film is magnetized by an in-plane magnetic DC bias ($H_0 = 105\ Oersted$) parallel to the electric current excitation, so that the FMR frequency is near 1.2 GHz, according to Kittel's equation (2.2-12). Note that in this case the FMR linewidth is $\Delta H = 30\ Oersted$, which is a conservative value for YIG, because single crystalline YIG has FMR linewidth as low as 1 $Oersted$. The total time-marching duration is 3020 seconds for 50000 time steps, which is impossible to be achieved by conventional FDTD with the same multiphysics setup. Figure 2.2-8 indicates accurate FMR prediction by the modeling, and the theoretical curve in Figure 2.2-8 is plotted based on Eq. (2.2-13):

$$[\mu] = \begin{bmatrix} \mu & 0 & -j\kappa \\ 0 & \mu_0 & 0 \\ -j\kappa & 0 & \mu \end{bmatrix} \quad (\hat{y}\text{ bias}). \tag{2.2-13}$$

where $\mu = \mu_0\left[1 + \omega_m(\omega_m + \omega_0)/[\omega_0(\omega_m + \omega_0) - \omega^2]\right]$, $\kappa = \mu_0\omega\omega_m/(\omega_0(\omega_m + \omega_0) - \omega^2)$, and $\omega_0 = \mu_0\gamma H_0 + j\alpha\omega$. Figure 2.2-9 clearly shows the distribution of the B_x and E_y fields at FMR, with B_x decreasing away from the bottom PEC, and E_y increasing.

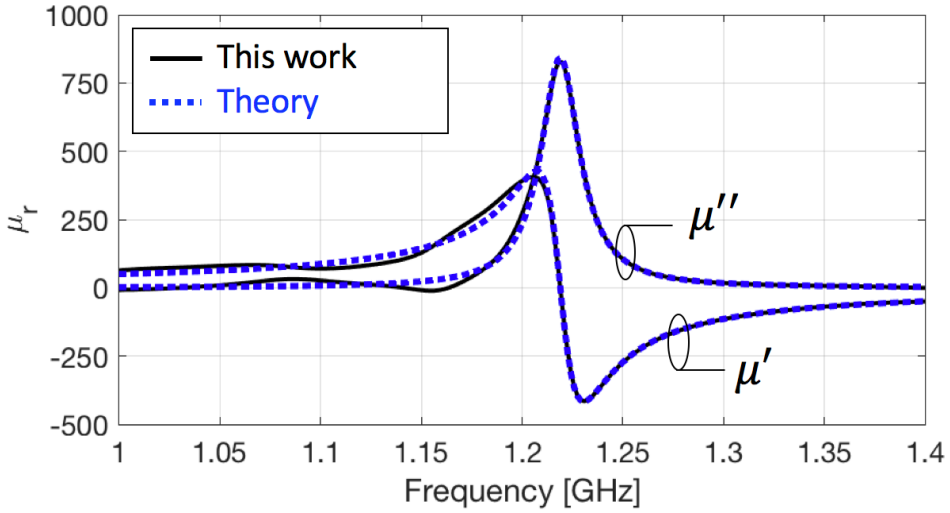

Figure 2.2-8. Dispersive permeability of thin-film YIG, simulated with the structure shown in Figure 2.2-7.

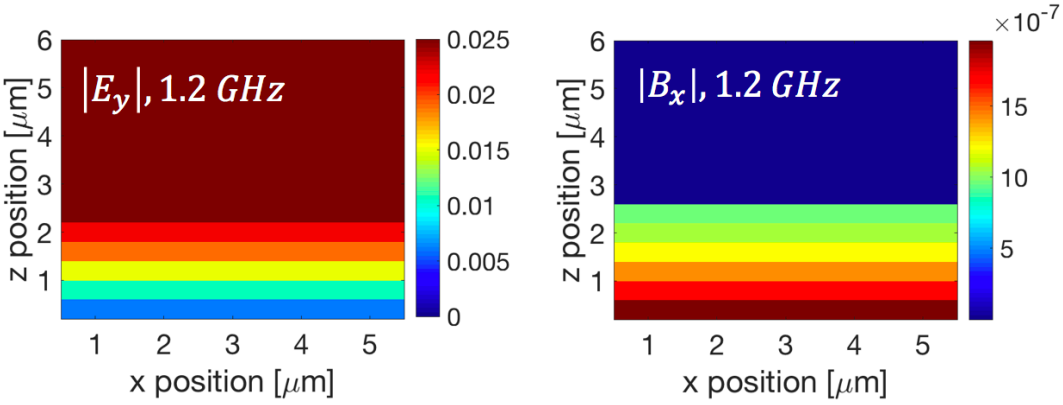

(a) (b)

Figure 2.2-9. Simulated **a.** electric field $\boldsymbol{E_y}$ and **b.** magnetic flux density $\boldsymbol{B_x}$ distribution in infinite YIG thin film at FMR frequency. The PEC ground plane is located at z=0.

2.3 Platform Effect Elimination

2.3.1 Radiation Q Factor with Platform Effect

As introduced in Chapter 1, conventional current based antennas suffer the platform effect when placed at a short distance above a conducting plane. The radiation becomes inefficient because the image current flows in the opposite direction and cancels the original current source. The excessive reactive energy stored between the radiating element and the conducting plane raises the radiation quality factor (radiation Q factor), and makes the antenna difficult to match [33]. In [7], a strain-mediated multiferroic antenna structure is proposed, which consists of a sandwich of two layers of piezoelectric material and one layer of thin-film magnetostrictive material. The lower bound of radiation Q factor decreases with higher permeability. The concept of utilizing high permeability magnetic material to lower the radiation quality factor is consistent with the approaches attempted in [34-36].

Consider an infinite, uniform current sheet that radiates into free space. The current source is grounded by an infinite perfect electrically conducting (PEC) plane (Figure 2.3-1). The thickness of the substrate is electrically small so that $kh \ll 1$. The wave directly radiated into the free space and the one reflected by the PEC plane interfere with each other. Therefore, the electromagnetic waves in different regions are:

$$\text{Energy storage field:} \quad \begin{cases} E_x = E_0 \sin(kz) \\ H_y = E_0/j\eta_0 \cos(kz) \end{cases} \qquad z < h$$

$$\text{Radiated field:} \quad \begin{cases} E_x = E_0 \sin(kh) \exp(-jk_0 z) \\ H_y = E_0/\eta_0 \sin(kh) \exp(-jk_0 z) \end{cases} \qquad z > h \tag{2.3-1}$$

where E_0 is the aperture electric field amplitude at the interface between the free space and the substrate. The radiated power into the free space is

$$P_{rad} = \frac{1}{2\eta_0}\iint_S |E|^2\, ds \approx \frac{1}{2\eta_0}E_0^2(kh)^2S \tag{2.3-2}$$

In Eq. (2.3-2), an approximation of linear electric field distribution along z direction is used. Similarly, an approximation of uniform magnetic field distribution along z direction leads to

$$W_H = \frac{1}{2}\iiint_{z<h}\mu|H|^2\, dv \approx \frac{1}{2}\mu|H|^2hS = \frac{1}{2}\epsilon E_0^2hS \tag{2.3-3}$$

Since $W_E \ll W_H$, the electric energy stored in the structure is negligible, thus $W_{total} \approx W_H$, which results in:

$$Q_{rad} \approx \omega\frac{W_H}{P_{rad}} = \frac{1}{\mu_r k_0 h} = \frac{\lambda_0}{2\pi h}\frac{1}{\mu_r} \tag{2.3-4}$$

Hence, for an antenna working at 2 *GHz*, Q_{rad} is on the order of 10^4 when the thickness of the substrate is 2 μm if the material is non-magnetic. Since traditional antennas are mostly made of conductors and rely on conductive current to radiate, platform effect is an inevitable shortcoming of traditional low-profile antennas. On the other hand, magnetic substrate with high relative permeability offers the capability of significantly lowering Q_{rad} and improving the radiation performance of low profile antennas.

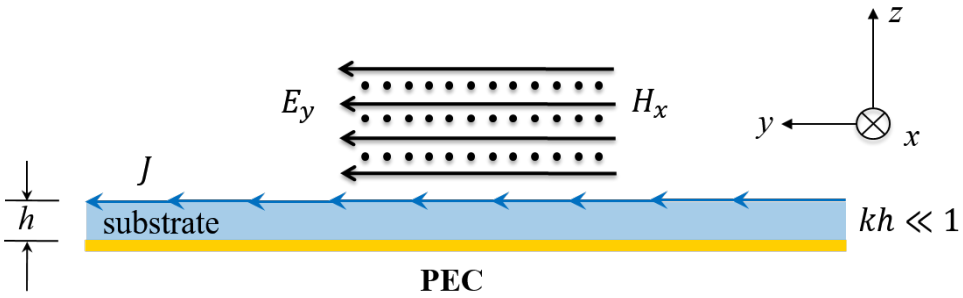

Figure 2.3-1. Radiation from electric current source. The coordinate system is chosen such that the surface current is in the *y* direction. The thickness of the substrate satisfies the condition $\boldsymbol{kh \ll 1}$.

In order to visualize the effect of platform effect on the radiation performance of the structure in Figure 2.1-1, define the radiation efficiency with the platform, $\xi_{platform}$, which indicates the percentage of power that can be released into the free space with the influence of platform effect:

$$\xi_{platform} = \frac{P_{rad}}{P_{free}} \tag{2.3-5}$$

where P_{rad} is the radiated power with the PEC ground, and P_{free} is the radiated power without the PEC ground.

$$P_{rad} = \frac{1}{2}\eta_0 \iint_S |H|^2 \, ds \tag{2.3-6}$$

$$P_{free} = \frac{1}{2}\eta_0 \iint_S \left|\frac{J_S}{2}\right|^2 ds \tag{2.3-7}$$

with *H* the observed magnetic field at a distance above the surface current with the PEC ground. The value of $\xi_{platform}$ also gives the information of the impedance mismatch between the structure with platform effect and free space.

Before moving on to the fully coupled scheme, we developed a conventional 3-D ADI FDTD code with only Maxwell's equation, to prove the concept. Figure 2.1-1 illustrates the FDTD model with continuous thin film. The size of the simulation space is 10×20×40 μm in the order of x, y and z direction. The upper boundary is absorbing boundary, the boundaries perpendicular to y axis are PEC boundary, and the boundaries perpendicular to x axis are perfect magnetic conductor (PMC). The thin film is grounded by PEC plane. A uniform electric current excitation is placed at the interface between the thin film and air. The field components are defined such that all the electric field components are along the edge of the spatial cell, and all the magnetic field components are normal to the cell surface. The material properties are defined such that all the tangential field components are continuous at material interfaces, e.g. H_x is continuous at interfaces parallel to x-y plane and x-z plane. The spatial resolution is Δx=1μm, Δy=0.1μm, Δz=0.1μm, and the time step is set as Δt=120Δt_{CFL}. The surface current excitation frequency is 2 *GHz*, and it is in the form of modified Gaussian pulse, with a bandwidth of ±500 *MHz*.

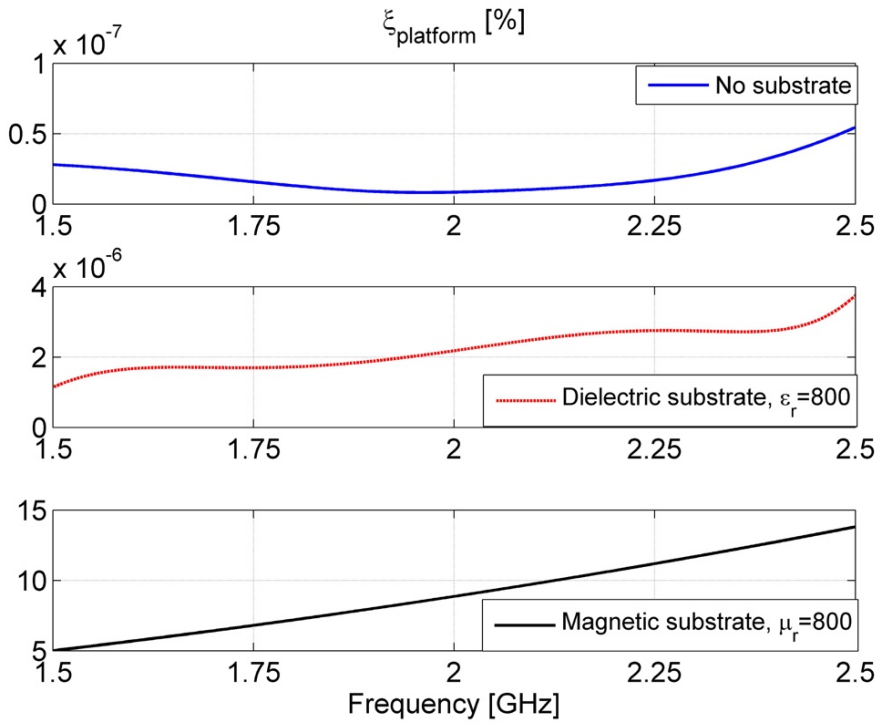

Figure 2.3-2. Radiation efficiencies of electric current sheet with platform effect, observed at z=38 μm. The thickness of the continuous substrate is 1.5 μm. All materials are lossless.

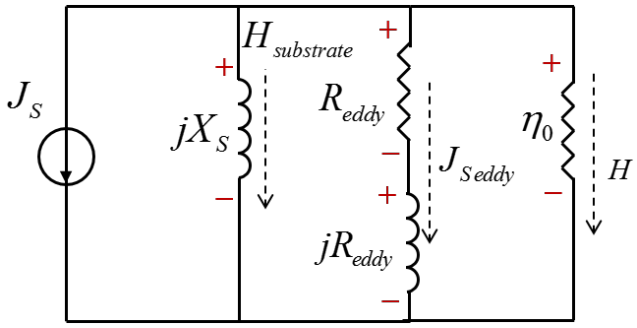

Figure 2.3-3. Equivalent circuit model of Figure 2.3-1. $H_{substrate}$ is the magnetic field inside the substrate, and H is the magnetic field observed in free space above the structure.

Comparing the values of $\xi_{platform}$ near 2 *GHz* in the three cases of Figure 2.3-5, one can clearly observe the advantage of magnetic substrate, because $\xi_{platform}$ in this case is 10^9 of that without any substrate, and 10^6 of that with highly dielectric substrate. The dielectric substrate could help improve the radiation because it changes the phase of the reflected wave.

It is evident that magnetic materials with high relative permeability could help overcome the platform effect. However, unfortunately, most of the materials that have such high permeability are ferromagnetic materials, which are highly conductive and suffer significant eddy current loss. For example, the relative permeability of FeGaB near ferromagnetic resonance could reach 1000, but the conductivity is 5×10^5 S/m. The high radiation Q factor caused by platform effect also affects the radiation efficiency which becomes more sensitive to ohmic loss and dielectric loss. The radiation efficiency is given by

$$\xi_{platform} = \frac{Q_{diss}}{Q_{rad}+Q_{diss}} \approx \frac{Q_{diss}}{Q_{rad}}, \text{ when } Q_{diss} \ll Q_{rad} \tag{2.3-8}$$

where Q_{diss} is the dissipation Q factor. As Q_{rad} increases, the radiation efficiency becomes lower and the influence of Q_{diss} becomes more dominant.

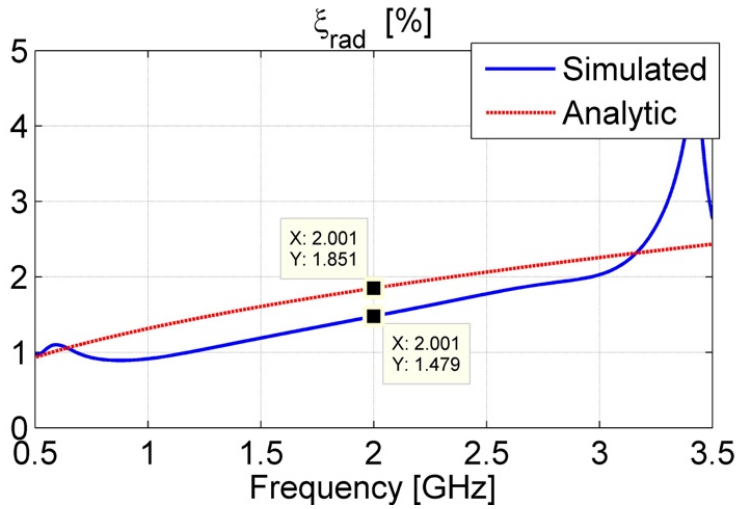

Figure 2.3-4. Radiation efficiencies with continuous thin film, observed at z=38 μm. The substrate material is FeGaB, with μ_r=800, σ=5×10^5 S/m. The thickness of the continuous substrate is 1.5 μm.

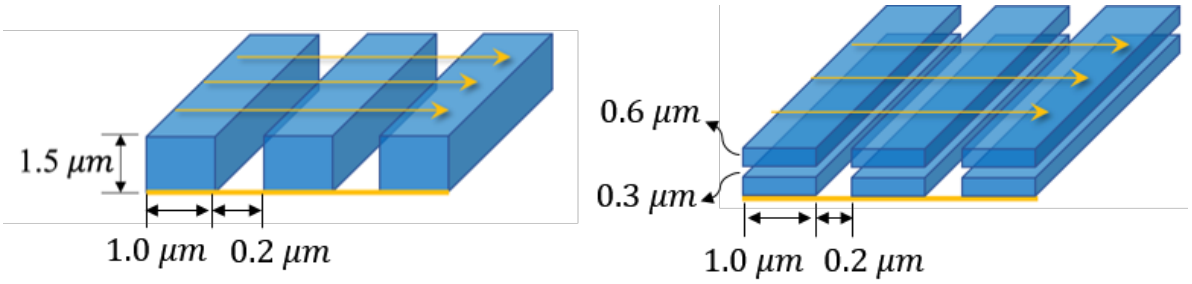

(a) (b)

Figure 2.3-5. Structures designed to suppress eddy current loss. **a.** Strip structure. **b.** 2-layer strip structure.

The structure in Figure 2.3-1 could be modeled by the equivalent circuit in Figure 2.3-3, and the analytic radiation efficiency could be calculated. Figure 2.3-4 shows that the simulated radiation efficiency and the analytic one agree with each other, but both are poor (only around 1.5%). In order to design a low-profile antenna with both high $\xi_{platform}$ and high ξ_{rad}, one needs to manipulate the shape of the magnetic thin film, so that the eddy current loss is suppressed. By briefly analyzing Faraday's law in the integral form $\int_C E \cdot dl = -(\partial/\partial t) \iint_S B \cdot dS$, one can quickly concludes that the eddy current loss can be well suppressed by cutting the continuous thin film into thin strips or by laminating it into multiple layers, as shown in Figure 2.3-5. It should be noted that the width of the strips should be comparable to the thickness, otherwise the eddy current loop could not be broken into small loops and the conductive loss will not be reduced. Additionally, the longitudinal direction of the strips should be along the magnetic flux. Figure 2.3-6 shows the magnitude of E_y component on y-z plane. Since the material is highly conductive, most of the electromagnetic field is concentrated within the air gap between adjacent strips. The improvement of radiation efficiency is shown by Figure 2.3-7. The strip structure could increase the radiation efficiency by 4.8 times compared to continuous film, and the 2-layer strip structure shows an improvement of 7 times. Therefore, one can conclude that in order to design low-profile antennas with good impedance matching feature and good radiation efficiency performance, the designer could use magnetic thin-film materials in lamination form.

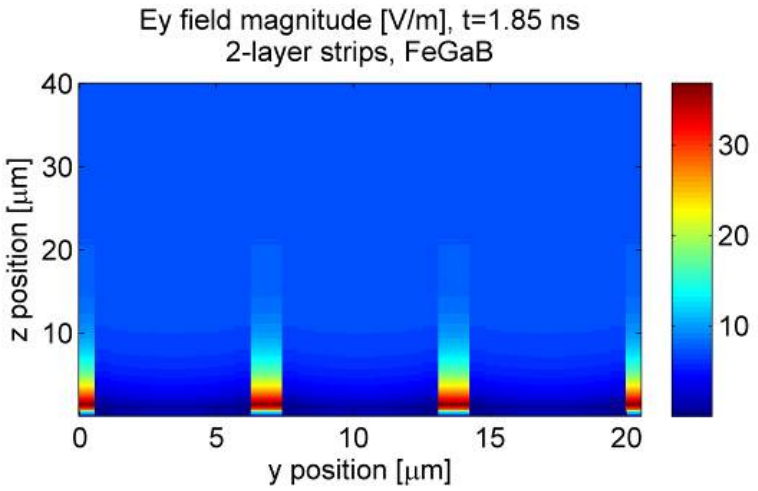

Figure 2.3-6. Magnitude of the electric field *y* component, observed at x=5 μm. The structure is the 2-layer strip shown in Figure 2.3-5b.

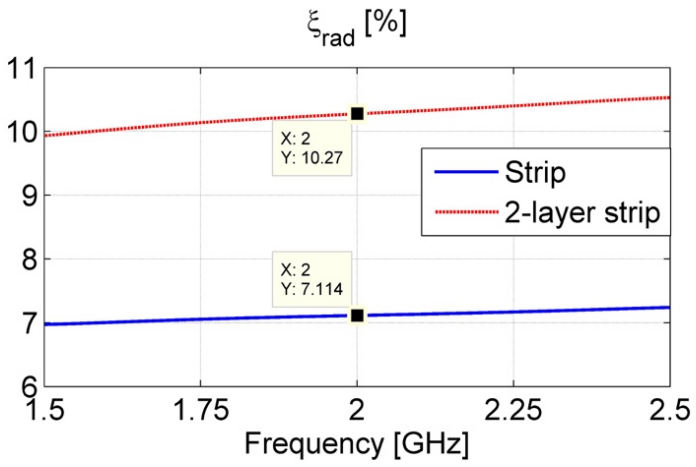

Figure 2.3-7. Radiation efficiencies of the two structures shown by Figure 2.3-5, observed at z=38 μm. The substrate material is FeGaB, with μ_r=800, σ=5×10^5 S/m.

2.3.2 Platform Effect Elimination with 3-D MUST Algorithm

In this section, the effect of high permeability in platform elimination is preliminarily explored in the full 3D geometry, using the proposed multiphysics solver. Figure 2.3-8 shows a $400\times400\ \mu m$ electric current sheet close to PEC loaded with 2 μm-thick YIG film. The simulation space is $480\times480\times60\ \mu m$ with $20\times20\times0.4\ \mu m$ spatial resolution. The radiator is placed in the middle of $x-y$ plane. The time-step is 5000 times of the CFL ($\Delta t_{CFL} = 7.6980\times10^{-16}s$). An FMR linewidth of $\Delta H = 30\ Oersted$ is used. As mentioned in Section 2.2.2, such a linewidth could be easily achieved with modern nanofabrication techniques. In order to distinguish the magnetic property from other possible effects, the relative permittivity is artificially set to be $\epsilon_r = 1$. The rest of the setup is the same to the case in Section 2.2.2.

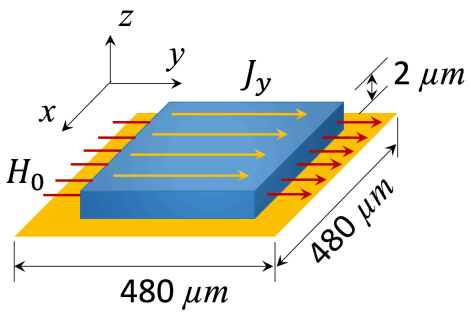

Figure 2.3-8. Planar current source on top of PEC ground plane, loaded with YIG thin film. The entire simulation space has dimensions as follows: $\boldsymbol{x = 480\ \mu m, y = 480\ \mu m, z = 60\ \mu m}$, with $\boldsymbol{\Delta x = 20\ \mu m, \Delta y = 20\ \mu m, \Delta z = 0.4\ \mu m}$. The YIG thin film is in the center of *x*-*y* plane, with a dimension of $\boldsymbol{400\times400\times2\ \mu m}$, i.e. a $\boldsymbol{40\ \mu m}$ gap is placed between the film and the outer boundary. The top surface of the simulation space is covered by an absorbing boundary condition.

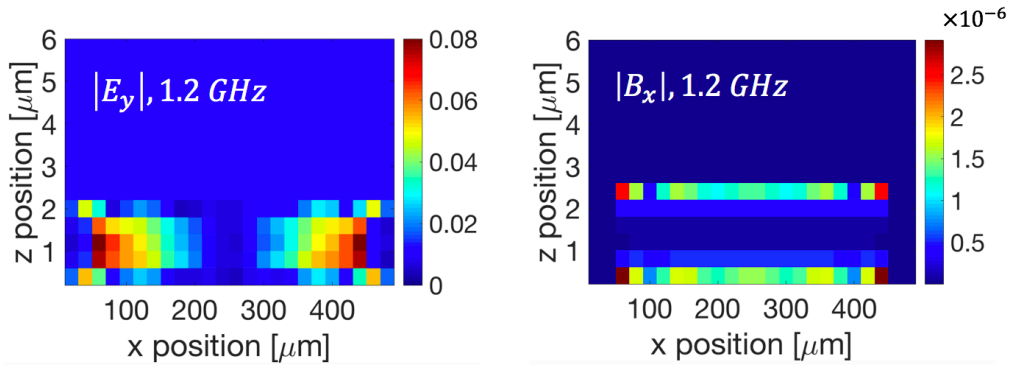

Figure 2.3-9. Simulated **a.** electric field $\boldsymbol{E_y}$ and **b.** magnetic flux density $\boldsymbol{B_x}$ distribution in finite YIG thin film at FMR frequency. The PEC ground plane is located at z=0.

Different from Figure 2.2-9, Figure 2.3-9 shows the edge effect due to the finite size of the magnetic film. The significant portion of the E_y and B_x fields close to the air gap indicates the existence of a potentially strong radiation. This is consistent with the prediction made in [7]. The far-field radiation pattern of an YIG thin film loaded electric current-excited radiator is calculated by a near-to-far field transform based on the surface equivalence theorem [63]. The transformation is conducted on an array of the structure shown in Figure 2.3-8, with 19.2× 19.2 cm total in-plane dimension, and 2 μm thickness, as shown in Figure 2.3-10. As shown in Figure 2.3-11, the radiation pattern is similar to that of an electric dipole, as expected. Among different bias fields, the radiation patterns are similar with only minor asymmetry change of the cross-pol. Such a structure presents relatively high cross-pol due to the anisotropic property of the magnetic thin film. Figure 2.3-12 shows the surface resistance of the radiator as a function of both frequency and magnetic DC bias. The surface impedance is calculated by

$$R_{surface} = \frac{2P_{rad}}{A \times |J_y|^2} \tag{2.3-9}$$

where A is the total area of the array. Such surface resistance reveals the influence of the PEC ground to the radiation performance, i.e. the platform effect. With no magnetic material, $R_{surface}$ is less than $2\times10^{-3}\Omega$. With magnetic thin film, the permeability is large at FMR, which boosts the surface resistance by three orders of magnitude. Figure 2.3-13 shows the radiation efficiency as a function of both frequency and magnetic DC bias. As mentioned in Section 2.3.1, the radiation efficiency is defined as the ratio of the radiated power from the structure under consideration, to the electric current radiation in free space, as shown by Eq. (2.3-5). It also reveals the influence of the PEC ground to the radiation performance. With no magnetic material, the radiation efficiency is less than 2×10^{-9}. Utilizing ferrite material to enhance antenna performance is consistent with the approaches attempted in [64].

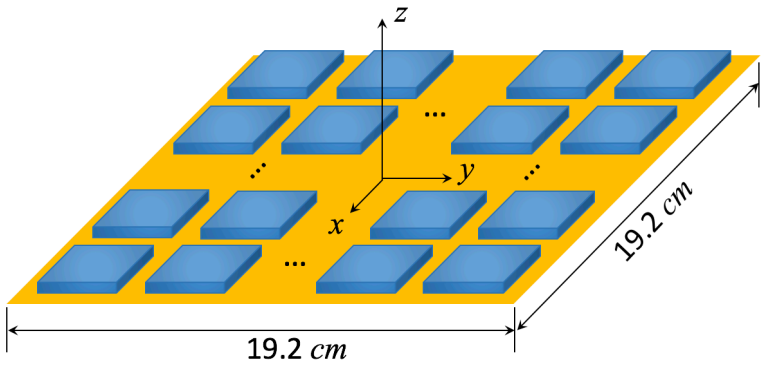

Figure 2.3-10. Planar array of YIG-loaded electric current radiator. The unit cell of Figure 2.3-8 is repeated by 400 times in both x and y directions, leading to a total dimension of $\mathbf{19.2\times 19.2\ cm}$. The effective area of YIG thin film is $\mathbf{16\times16\ cm^2}$. Both the magnetic DC bias $\boldsymbol{H_i}$ and the electric current source $\boldsymbol{J_y}$ are in the y direction.

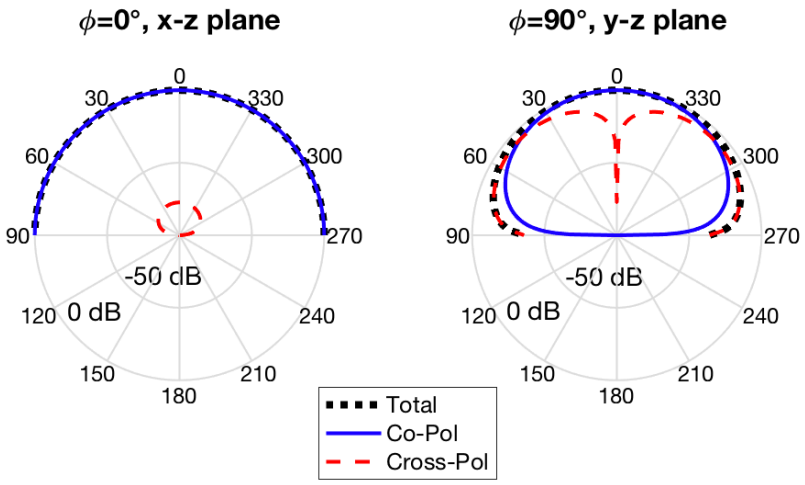

Figure 2.3-11. Far-field pattern from the planar current source on top of PEC ground plane, loaded with YIG thin film. $\boldsymbol{H_0 = 105\ Oersted}$.

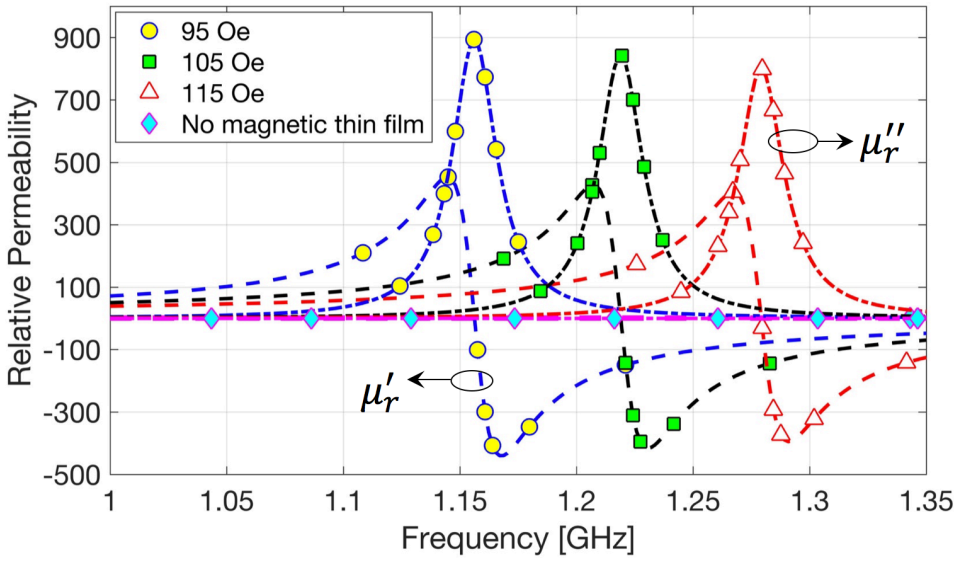

(a)

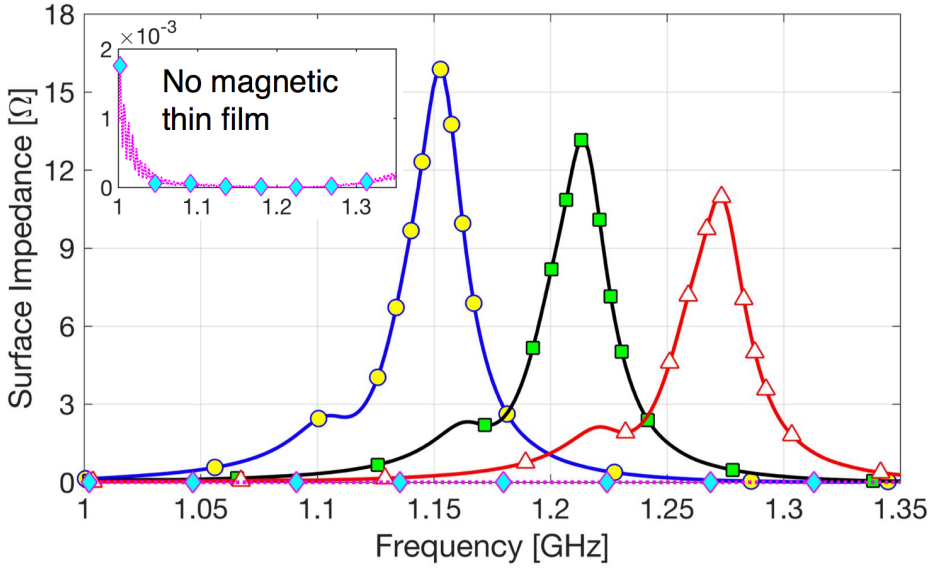

(b)

Figure 2.3-12. Surface resistance of ferrite-loaded current source shown in Figure 2.3-10.

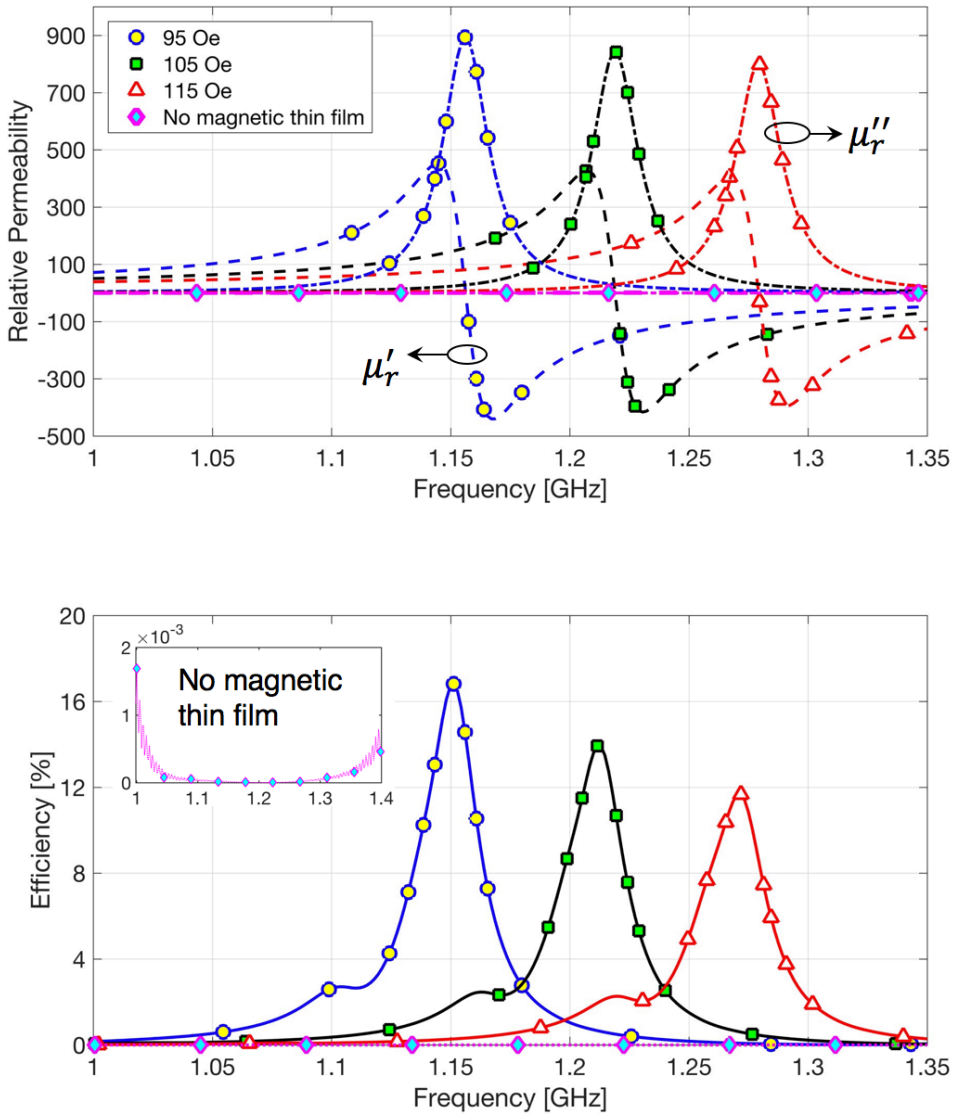

Figure 2.3-13. Radiation efficiency of ferrite-loaded current source shown in Figure 2.3-10.

2.4 Summary

A multiphysics simulation algorithm is proposed for the first time, to accurately model the dynamic interaction between micromagnetics and electrodynamics. The proposed method can model the fine detail of RF devices consisting magnetic thin films, and predict the unique properties of magnetic materials quickly and accurately. With easy expansion to include additional physics, the proposed algorithm has the potential of solving and designing nonlinear, nonuniform, and/or anisotropic devices.

2.5 Appendix: 3-D ADI FDTD Time Marching Equations with LLG

The equations for E_x fields calculation in the first sub-iteration are shown in (2A-1), with $P_{e_x1} = (\Delta t^2)/[4\epsilon_r\epsilon_0(\Delta y)^2]$, $P_{e_x2} = (\Delta t^2)/(4\epsilon_r\epsilon_0\Delta y\Delta z)$, $P_{e_x3} = \Delta t/(2\epsilon_r\epsilon_0\Delta z)$, $P_{e_x4} = \Delta t/(2\epsilon_r\epsilon_0\Delta y)$, $P_{e_x5} = (\Delta t^2)/(4\epsilon_r\epsilon_0\Delta x\Delta y)$, $R_n = A_n/A_0$ at the corresponding mesh.

$$\left\{1+\frac{\sigma\Delta t}{4\epsilon_r\epsilon_0}+2P_{e_x1}R_1\right\}E_x\Big|^{n+\frac{1}{2}}_{i+\frac{1}{2},j,k} - P_{e_x1}R_1E_x\Big|^{n+\frac{1}{2}}_{i+\frac{1}{2},j-1,k} - P_{e_x1}R_1\,E_x\Big|^{n+\frac{1}{2}}_{i+\frac{1}{2},j+1,k}$$

$$+\frac{1}{4}P_{e_x2}R_2\left[E_y\Big|^{n+\frac{1}{2}}_{i,j+\frac{1}{2},k+1} - E_y\Big|^{n+\frac{1}{2}}_{i,j+\frac{1}{2},k-1} + E_y\Big|^{n+\frac{1}{2}}_{i+1,j+\frac{1}{2},k+1} - E_y\Big|^{n+\frac{1}{2}}_{i+1,j+\frac{1}{2},k-1}\right]$$

$$-\frac{1}{4}P_{e_x2}R_2\left[E_y\Big|^{n+\frac{1}{2}}_{i,j-\frac{1}{2},k+1} - E_y\Big|^{n+\frac{1}{2}}_{i,j-\frac{1}{2},k-1} + E_y\Big|^{n+\frac{1}{2}}_{i+1,j-\frac{1}{2},k+1} - E_y\Big|^{n+\frac{1}{2}}_{i+1,j-\frac{1}{2},k-1}\right]$$

$$=\left[1-\frac{\sigma\Delta t}{4\epsilon_r\epsilon_0}\right]E_x\Big|^{n}_{i+\frac{1}{2},j,k} - P_{e_x3}\left[H_y\Big|^{n}_{i+\frac{1}{2},j,k+\frac{1}{2}} - H_y\Big|^{n}_{i+\frac{1}{2},j,k-\frac{1}{2}}\right] + P_{e_x4}\left[R_5H_z\Big|^{n}_{i+\frac{1}{2},j+\frac{1}{2},k} - R_5H_z\Big|^{n}_{i+\frac{1}{2},j-\frac{1}{2},k}\right]$$

$$-\frac{1}{2}P_{e_x4}\left[R_6H_{x_{back}}\Big|^{n}_{i+\frac{1}{2},j+\frac{1}{2},k} + R_6H_{x_{front}}\Big|^{n}_{i+\frac{1}{2},j+\frac{1}{2},k} - R_6H_{x_{back}}\Big|^{n}_{i+\frac{1}{2},j-\frac{1}{2},k} - R_6H_{x_{front}}\Big|^{n}_{i+\frac{1}{2},j-\frac{1}{2},k}\right]$$

$$+\frac{1}{4}P_{e_x4}\begin{bmatrix}(R_3+R_1)B_{z_{1_{back}}}\Big|^{n}_{i+\frac{1}{2},j+\frac{1}{2},k} + (R_3+R_1)B_{z_{1_{front}}}\Big|^{n}_{i+\frac{1}{2},j+\frac{1}{2},k}\\ +(R_3+R_1)B_{z_{2_{back}}}\Big|^{n}_{i+\frac{1}{2},j+\frac{1}{2},k} + (R_3+R_1)B_{z_{2_{front}}}\Big|^{n}_{i+\frac{1}{2},j+\frac{1}{2},k}\end{bmatrix}$$

$$-\frac{1}{4}P_{e_x4}\begin{bmatrix}(R_3+R_1)B_{z_{1back}}|^n_{i+\frac{1}{2},j-\frac{1}{2},k}+(R_3+R_1)B_{z_{1front}}|^n_{i+\frac{1}{2},j-\frac{1}{2},k}\\+(R_3+R_1)B_{z_{2back}}|^n_{i+\frac{1}{2},j-\frac{1}{2},k}+(R_3+R_1)B_{z_{2front}}|^n_{i+\frac{1}{2},j-\frac{1}{2},k}\end{bmatrix}$$

$$-P_{e_x4}\left[(R_2+R_4)B_{x_{ave}}|^n_{i+\frac{1}{2},j+\frac{1}{2},k}-(R_2+R_4)B_{x_{ave}}|^n_{i+\frac{1}{2},j-\frac{1}{2},k}\right]$$

$$-P_{e_x5}R_1\left[E_y|^n_{i+1,j+\frac{1}{2},k}-E_y|^n_{i,j+\frac{1}{2},k}-E_y|^n_{i+1,j-\frac{1}{2},k}+E_y|^n_{i,j-\frac{1}{2},k}\right]$$

$$+\frac{1}{4}P_{e_x1}R_2\begin{bmatrix}E_z|^n_{i,j+1,k+\frac{1}{2}}-E_z|^n_{i,j,k+\frac{1}{2}}+E_z|^n_{i,j+1,k-\frac{1}{2}}-E_z|^n_{i,j,k-\frac{1}{2}}\\+E_z|^n_{i+1,j+1,k+\frac{1}{2}}-E_z|^n_{i+1,j,k+\frac{1}{2}}+E_z|^n_{i+1,j+1,k-\frac{1}{2}}-E_z|^n_{i+1,j,k-\frac{1}{2}}\end{bmatrix}$$

$$-\frac{1}{4}P_{e_x1}R_2\begin{bmatrix}E_z|^n_{i,j,k+\frac{1}{2}}-E_z|^n_{i,j-1,k+\frac{1}{2}}+E_z|^n_{i,j,k-\frac{1}{2}}-E_z|^n_{i,j-1,k-\frac{1}{2}}\\+E_z|^n_{i+1,j,k+\frac{1}{2}}-E_z|^n_{i+1,j-1,k+\frac{1}{2}}+E_z|^n_{i+1,j,k-\frac{1}{2}}-E_z|^n_{i+1,j-1,k-\frac{1}{2}}\end{bmatrix} \quad \text{(2A-1)}$$

Similarly, the time-marching equations for E_y and E_z fields in the first sub-iteration are shown in (2A-2) and (2A-3), respectively.

$$\left\{1+\frac{\sigma\Delta t}{4\epsilon_r\epsilon_0}+2P_{e_y1}R_1\right\}E_y|^{n+\frac{1}{2}}_{i,j+\frac{1}{2},k}-P_{e_y1}R_1E_y|^{n+\frac{1}{2}}_{i,j+\frac{1}{2},k-1}-P_{e_y1}R_1E_y|^{n+\frac{1}{2}}_{i,j+\frac{1}{2},k+1}$$

$$-\frac{1}{4}P_{e_y2}R_2\begin{bmatrix}E_x|^{n+\frac{1}{2}}_{i+\frac{1}{2},j+1,k}-E_x|^{n+\frac{1}{2}}_{i+\frac{1}{2},j,k}+E_x|^{n+\frac{1}{2}}_{i+\frac{1}{2},j+1,k+1}-E_x|^{n+\frac{1}{2}}_{i+\frac{1}{2},j,k+1}\\+E_x|^{n+\frac{1}{2}}_{i-\frac{1}{2},j+1,k}-E_x|^{n+\frac{1}{2}}_{i-\frac{1}{2},j,k}+E_x|^{n+\frac{1}{2}}_{i-\frac{1}{2},j+1,k+1}-E_x|^{n+\frac{1}{2}}_{i-\frac{1}{2},j,k+1}\end{bmatrix}$$

$$+\frac{1}{4}P_{e_y2}R_2\begin{bmatrix}E_x|^{n+\frac{1}{2}}_{i+\frac{1}{2},j+1,k}-E_x|^{n+\frac{1}{2}}_{i+\frac{1}{2},j,k}+E_x|^{n+\frac{1}{2}}_{i+\frac{1}{2},j+1,k-1}-E_x|^{n+\frac{1}{2}}_{i+\frac{1}{2},j,k-1}\\+E_x|^{n+\frac{1}{2}}_{i-\frac{1}{2},j+1,k}-E_x|^{n+\frac{1}{2}}_{i-\frac{1}{2},j,k}+E_x|^{n+\frac{1}{2}}_{i-\frac{1}{2},j+1,k-1}-E_x|^{n+\frac{1}{2}}_{i-\frac{1}{2},j,k-1}\end{bmatrix}$$

$$=\left[1-\frac{\sigma\Delta t}{4\epsilon_r\epsilon_0}\right]E_y|^n_{i,j+\frac{1}{2},k}-P_{e_y3}\left[H_z|^n_{i+\frac{1}{2},j+\frac{1}{2},k}-H_z|^n_{i-\frac{1}{2},j+\frac{1}{2},k}\right]+P_{e_y4}\left[R_5H_x|^n_{i,j+\frac{1}{2},k+\frac{1}{2}}-R_5H_x|^n_{i,j+\frac{1}{2},k-\frac{1}{2}}\right]$$

$$+\frac{1}{2}P_{e_y4}\left[R_6H_{z_{low}}|^n_{i,j+\frac{1}{2},k+\frac{1}{2}}+R_6H_{z_{up}}|^n_{i,j+\frac{1}{2},k+\frac{1}{2}}-R_6H_{z_{low}}|^n_{i,j+\frac{1}{2},k-\frac{1}{2}}-R_6H_{z_{up}}|^n_{i,j+\frac{1}{2},k-\frac{1}{2}}\right]$$

$$+\frac{1}{4}P_{e_y4}\begin{bmatrix}(R_3+R_1)B_{x_{1low}}|^n_{i,j+\frac{1}{2},k+\frac{1}{2}}+(R_3+R_1)B_{x_{1up}}|^n_{i,j+\frac{1}{2},k+\frac{1}{2}}\\+(R_3+R_1)B_{x_{2low}}|^n_{i,j+\frac{1}{2},k+\frac{1}{2}}+(R_3+R_1)B_{x_{2up}}|^n_{i,j+\frac{1}{2},k+\frac{1}{2}}\end{bmatrix}$$

$$-\frac{1}{4}P_{e_y4}\begin{bmatrix}(R_3+R_1)B_{x_{1_{low}}}|^n_{i,j+\frac{1}{2},k-\frac{1}{2}}+(R_3+R_1)B_{x_{1_{up}}}|^n_{i,j+\frac{1}{2},k-\frac{1}{2}}\\+(R_3+R_1)B_{x_{2_{low}}}|^n_{i,j+\frac{1}{2},k-\frac{1}{2}}+(R_3+R_1)B_{x_{2_{up}}}|^n_{i,j+\frac{1}{2},k-\frac{1}{2}}\end{bmatrix}$$

$$+P_{e_y4}\left[(R_2+R_4)B_{z_{ave}}|^n_{i,j+\frac{1}{2},k+\frac{1}{2}}-(R_2+R_4)B_{z_{ave}}|^n_{i,j+\frac{1}{2},k-\frac{1}{2}}\right]$$

$$-P_{e_y2}R_1\left[E_z|^n_{i,j+1,k+\frac{1}{2}}-E_z|^n_{i,j,k+\frac{1}{2}}-E_z|^n_{i,j+1,k-\frac{1}{2}}+E_z|^n_{i,j,k-\frac{1}{2}}\right]$$

$$-\frac{1}{4}P_{e_y5}R_2\left[E_y|^n_{i+1,j+\frac{1}{2},k}+E_y|^n_{i+1,j+\frac{1}{2},k+1}-E_y|^n_{i-1,j+\frac{1}{2},k}-E_y|^n_{i-1,j+\frac{1}{2},k+1}\right]$$

$$+\frac{1}{4}P_{e_y5}R_2\left[E_y|^n_{i+1,j+\frac{1}{2},k}+E_y|^n_{i+1,j+\frac{1}{2},k-1}-E_y|^n_{i-1,j+\frac{1}{2},k}-E_y|^n_{i-1,j+\frac{1}{2},k-1}\right] \quad \text{(2A-2)}$$

with $P_{e_y1}=(\Delta t^2)/[4\epsilon_r\epsilon_0(\Delta z)^2]$, $P_{e_y2}=(\Delta t^2)/(4\epsilon_r\epsilon_0\Delta y\Delta z)$, $P_{e_y3}=\Delta t/(2\epsilon_r\epsilon_0\Delta x)$, $P_{e_y4}=\Delta t/(2\epsilon_r\epsilon_0\Delta z)$, $P_{e_y5}=(\Delta t^2)/(4\epsilon_r\epsilon_0\Delta z\Delta x)$, $R_n=A_n/A_0$ at the corresponding mesh.

$$\left\{1+\frac{\sigma\Delta t}{4\epsilon_r\epsilon_0}+\frac{(\Delta t)^2}{2\epsilon_r\epsilon_0\mu_0(\Delta x)^2}\right\}E_z|^{n+\frac{1}{2}}_{i,j,k+\frac{1}{2}}-\frac{(\Delta t)^2}{4\epsilon_r\epsilon_0\mu_0(\Delta x)^2}E_z|^{n+\frac{1}{2}}_{i-1,j,k+\frac{1}{2}}-\frac{(\Delta t)^2}{4\epsilon_r\epsilon_0\mu_0(\Delta x)^2}E_z|^{n+\frac{1}{2}}_{i+1,j,k+\frac{1}{2}}$$

$$=\left[1-\frac{\sigma\Delta t}{4\epsilon_r\epsilon_0}\right]E_z|^n_{i,j,k+\frac{1}{2}}+\frac{\Delta t}{2\epsilon_r\epsilon_0\Delta x}\left[H_y|^n_{i+\frac{1}{2},j,k+\frac{1}{2}}-H_y|^n_{i-\frac{1}{2},j,k+\frac{1}{2}}\right]-\frac{\Delta t}{2\epsilon_r\epsilon_0\Delta y}\left[H_x|^n_{i,j+\frac{1}{2},k+\frac{1}{2}}-H_y|^n_{i,j-\frac{1}{2},k+\frac{1}{2}}\right]$$

$$+\frac{(\Delta t)^2}{4\epsilon_r\epsilon_0\mu_0\Delta x\Delta z}\left[E_x|^n_{i-\frac{1}{2},j,k+1}-E_x|^n_{i-\frac{1}{2},j,k}-E_x|^n_{i+\frac{1}{2},j,k+1}+E_x|^n_{i+\frac{1}{2},j,k}\right] \quad \text{(2A-3)}$$

The calculation of the electric fields in the second sub-iteration is derived in a similar manner, shown in (2A-4)–(2A-6).

$$\left\{1+\frac{\sigma\Delta t}{4\epsilon_r\epsilon_0}+\frac{(\Delta t)^2}{2\epsilon_r\epsilon_0\mu_0(\Delta z)^2}\right\}E_x|^{n+1}_{i+\frac{1}{2},j,k}-\frac{(\Delta t)^2}{4\epsilon_r\epsilon_0\mu_0(\Delta z)^2}E_x|^{n+1}_{i+\frac{1}{2},j,k-1}-\frac{(\Delta t)^2}{4\epsilon_r\epsilon_0\mu_0(\Delta z)^2}E_x|^{n+1}_{i+\frac{1}{2},j,k+1}$$

$$=\left[1-\frac{\sigma\Delta t}{4\epsilon_r\epsilon_0}\right]E_x|^{n+\frac{1}{2}}_{i+\frac{1}{2},j,k}+\frac{\Delta t}{2\epsilon_r\epsilon_0\Delta y}\left[H_z|^{n+\frac{1}{2}}_{i+\frac{1}{2},j+\frac{1}{2},k}-H_z|^{n+\frac{1}{2}}_{i+\frac{1}{2},j-\frac{1}{2},k}\right]-\frac{\Delta t}{2\epsilon_r\epsilon_0\Delta z}\left[H_y|^{n+\frac{1}{2}}_{i+\frac{1}{2},j,k+\frac{1}{2}}-H_y|^{n+\frac{1}{2}}_{i+\frac{1}{2},j,k-\frac{1}{2}}\right]$$

$$+\frac{(\Delta t)^2}{4\epsilon_r\epsilon_0\mu_0\Delta x\Delta z}\left[E_z|^{n+\frac{1}{2}}_{i+1,j,k-\frac{1}{2}}-E_z|^{n+\frac{1}{2}}_{i,j,k-\frac{1}{2}}-E_z|^{n+\frac{1}{2}}_{i+1,j,k+\frac{1}{2}}+E_z|^{n+\frac{1}{2}}_{i,j,k+\frac{1}{2}}\right] \quad \text{(2A-4)}$$

$$\left\{1+\frac{\sigma\Delta t}{4\epsilon_r\epsilon_0}+2Q_{e_y1}R_1\right\}E_y|^{n+1}_{i,j+\frac{1}{2},k}-Q_{e_y1}R_1E_y|^{n+1}_{i-1,j+\frac{1}{2},k}-Q_{e_y1}R_1\,E_y|^{n+1}_{i+1,j+\frac{1}{2},k}$$

$$+\frac{1}{4}Q_{e_y2}R_2\begin{bmatrix}E_z|^{n+1}_{i,j+1,k+\frac{1}{2}}-E_z|^{n+1}_{i,j,k+\frac{1}{2}}+E_z|^{n+1}_{i,j+1,k-\frac{1}{2}}-E_z|^{n+1}_{i,j,k-\frac{1}{2}}\\+E_z|^{n+1}_{i+1,j+1,k+\frac{1}{2}}-E_z|^{n+1}_{i+1,j,k+\frac{1}{2}}+E_z|^{n+1}_{i+1,j+1,k-\frac{1}{2}}-E_z|^{n+1}_{i+1,j,k-\frac{1}{2}}\end{bmatrix}$$

$$-\frac{1}{4}Q_{e_y2}R_2\begin{bmatrix}E_z|^{n+1}_{i,j+1,k+\frac{1}{2}}-E_z|^{n+1}_{i,j,k+\frac{1}{2}}+E_z|^{n+1}_{i,j+1,k-\frac{1}{2}}-E_z|^{n+1}_{i,j,k-\frac{1}{2}}\\+E_z|^{n+1}_{i-1,j+1,k+\frac{1}{2}}-E_z|^{n+1}_{i-1,j,k+\frac{1}{2}}+E_z|^{n+1}_{i-1,j+1,k-\frac{1}{2}}-E_z|^{n+1}_{i-1,j,k-\frac{1}{2}}\end{bmatrix}$$

$$=\left[1-\frac{\sigma\Delta t}{4\epsilon_r\epsilon_0}\right]E_y|^{n+\frac{1}{2}}_{i,j+\frac{1}{2},k}+Q_{e_y3}\left[H_x|^{n+\frac{1}{2}}_{i,j+\frac{1}{2},k+\frac{1}{2}}-H_x|^{n+\frac{1}{2}}_{i,j+\frac{1}{2},k-\frac{1}{2}}\right]-Q_{e_y4}\left[R_5H_z|^{n+\frac{1}{2}}_{i+\frac{1}{2},j+\frac{1}{2},k}-R_5H_z|^{n+\frac{1}{2}}_{i-\frac{1}{2},j+\frac{1}{2},k}\right]$$

$$+\frac{1}{2}Q_{e_y4}\left[R_6H_{x_{back}}|^{n+\frac{1}{2}}_{i+\frac{1}{2},j+\frac{1}{2},k}+R_6H_{x_{front}}|^{n+\frac{1}{2}}_{i+\frac{1}{2},j+\frac{1}{2},k}-R_6H_{x_{back}}|^{n+\frac{1}{2}}_{i-\frac{1}{2},j+\frac{1}{2},k}-R_6H_{x_{front}}|^{n+\frac{1}{2}}_{i-\frac{1}{2},j+\frac{1}{2},k}\right]$$

$$-\frac{1}{4}Q_{e_y4}\begin{bmatrix}(R_3+R_1)B_{z_{1back}}|^{n+\frac{1}{2}}_{i+\frac{1}{2},j+\frac{1}{2},k}+(R_3+R_1)B_{z_{1front}}|^{n+\frac{1}{2}}_{i+\frac{1}{2},j+\frac{1}{2},k}\\+(R_3+R_1)B_{z_{2back}}|^{n+\frac{1}{2}}_{i+\frac{1}{2},j+\frac{1}{2},k}+(R_3+R_1)B_{z_{2front}}|^{n+\frac{1}{2}}_{i+\frac{1}{2},j+\frac{1}{2},k}\end{bmatrix}$$

$$+\frac{1}{4}Q_{e_y4}\begin{bmatrix}(R_3+R_1)B_{z_{1back}}|^{n+\frac{1}{2}}_{i-\frac{1}{2},j+\frac{1}{2},k}+(R_3+R_1)B_{z_{1front}}|^{n+\frac{1}{2}}_{i-\frac{1}{2},j+\frac{1}{2},k}\\+(R_3+R_1)B_{z_{2back}}|^{n+\frac{1}{2}}_{i-\frac{1}{2},j+\frac{1}{2},k}+(R_3+R_1)B_{z_{2front}}|^{n+\frac{1}{2}}_{i-\frac{1}{2},j+\frac{1}{2},k}\end{bmatrix}$$

$$+Q_{e_y4}\left[(R_2+R_4)B_{x_{ave}}|^{n+\frac{1}{2}}_{i+\frac{1}{2},j+\frac{1}{2},k}-(R_2+R_4)B_{x_{ave}}|^{n+\frac{1}{2}}_{i-\frac{1}{2},j+\frac{1}{2},k}\right]$$

$$-Q_{e_y2}R_1\left[E_x|^{n+\frac{1}{2}}_{i+\frac{1}{2},j+1,k}-E_x|^{n+\frac{1}{2}}_{i+\frac{1}{2},j,k}-E_x|^{n+\frac{1}{2}}_{i-\frac{1}{2},j+1,k}+E_x|^{n+\frac{1}{2}}_{i-\frac{1}{2},j,k}\right]$$

$$+\frac{1}{4}Q_{e_y5}R_2\left[E_y|^{n+\frac{1}{2}}_{i,j+\frac{1}{2},k+1}-E_y|^{n+\frac{1}{2}}_{i,j+\frac{1}{2},k-1}+E_y|^{n+\frac{1}{2}}_{i+1,j+\frac{1}{2},k+1}-E_y|^{n+\frac{1}{2}}_{i+1,j+\frac{1}{2},k-1}\right]$$

$$-\tfrac{1}{4}Q_{e_y5}R_2\left[E_y|^{n+\frac{1}{2}}_{i,j+\frac{1}{2},k+1}-E_y|^{n+\frac{1}{2}}_{i,j+\frac{1}{2},k-1}+E_y|^{n+\frac{1}{2}}_{i-1,j+\frac{1}{2},k+1}-E_y|^{n+\frac{1}{2}}_{i-1,j+\frac{1}{2},k-1}\right] \qquad \text{(2A-5)}$$

where $Q_{e_y1}=(\Delta t^2)/[4\epsilon_r\epsilon_0(\Delta x)^2]$, $Q_{e_y2}=(\Delta t^2)/(4\epsilon_r\epsilon_0\Delta y\Delta x)$, $Q_{e_y3}=\Delta t/(2\epsilon_r\epsilon_0\Delta z)$, $Q_{e_y4}=\Delta t/(2\epsilon_r\epsilon_0\Delta x)$, $Q_{e_y5}=(\Delta t^2)/(4\epsilon_r\epsilon_0\Delta x\Delta z)$, $R_n=A_n/A_0$ at the corresponding mesh.

$$
\begin{aligned}
&\left\{1+\frac{\sigma\Delta t}{4\epsilon_r\epsilon_0}+2Q_{e_z1}R_1\right\}E_z|_{i,j,k+\frac{1}{2}}^{n+1}-Q_{e_z1}R_1E_z|_{i,j-1,k+\frac{1}{2}}^{n+1}-Q_{e_z1}R_1\,E_z|_{i,j+1,k+\frac{1}{2}}^{n+1}\\
&-\frac{1}{4}Q_{e_z2}R_2\left[E_y|_{i+1,j+\frac{1}{2},k}^{n+1}+E_y|_{i+1,j+\frac{1}{2},k+1}^{n+1}-E_y|_{i-1,j+\frac{1}{2},k}^{n+1}-E_y|_{i-1,j+\frac{1}{2},k+1}^{n+1}\right]\\
&+\frac{1}{4}Q_{e_z2}R_2\left[E_y|_{i+1,j-\frac{1}{2},k}^{n+1}+E_y|_{i+1,j-\frac{1}{2},k+1}^{n+1}-E_y|_{i-1,j-\frac{1}{2},k}^{n+1}-E_y|_{i-1,j-\frac{1}{2},k+1}^{n+1}\right]\\
&=\left[1-\frac{\sigma\Delta t}{4\epsilon_r\epsilon_0}\right]E_z|_{i,j,k+\frac{1}{2}}^{n+\frac{1}{2}}+Q_{e_z3}\left[H_y|_{i+\frac{1}{2},j,k+\frac{1}{2}}^{n+\frac{1}{2}}-H_y|_{i-\frac{1}{2},j,k+\frac{1}{2}}^{n+\frac{1}{2}}\right]-Q_{e_z4}\left[R_5H_x|_{i,j+\frac{1}{2},k+\frac{1}{2}}^{n+\frac{1}{2}}-R_5H_x|_{i,j-\frac{1}{2},k+\frac{1}{2}}^{n+\frac{1}{2}}\right]\\
&-\frac{1}{2}Q_{e_z4}\left[R_6H_{z_{low}}|_{i,j+\frac{1}{2},k+\frac{1}{2}}^{n+\frac{1}{2}}+R_6H_{z_{up}}|_{i,j+\frac{1}{2},k+\frac{1}{2}}^{n+\frac{1}{2}}-R_6H_{z_{low}}|_{i,j-\frac{1}{2},k+\frac{1}{2}}^{n+\frac{1}{2}}-R_6H_{z_{up}}|_{i,j-\frac{1}{2},k+\frac{1}{2}}^{n+\frac{1}{2}}\right]\\
&-\frac{1}{4}Q_{e_z4}\left[\begin{array}{l}(R_3+R_1)B_{x_{1_{low}}}|_{i,j+\frac{1}{2},k+\frac{1}{2}}^{n+\frac{1}{2}}+(R_3+R_1)B_{x_{1_{up}}}|_{i,j+\frac{1}{2},k+\frac{1}{2}}^{n+\frac{1}{2}}\\+(R_3+R_1)B_{x_{2_{low}}}|_{i,j+\frac{1}{2},k+\frac{1}{2}}^{n+\frac{1}{2}}+(R_3+R_1)B_{x_{2_{up}}}|_{i,j+\frac{1}{2},k+\frac{1}{2}}^{n+\frac{1}{2}}\end{array}\right]\\
&+\frac{1}{4}Q_{e_z4}\left[\begin{array}{l}(R_3+R_1)B_{x_{1_{low}}}|_{i,j-\frac{1}{2},k+\frac{1}{2}}^{n+\frac{1}{2}}+(R_3+R_1)B_{x_{1_{up}}}|_{i,j-\frac{1}{2},k+\frac{1}{2}}^{n+\frac{1}{2}}\\+(R_3+R_1)B_{x_{2_{low}}}|_{i,j-\frac{1}{2},k+\frac{1}{2}}^{n+\frac{1}{2}}+(R_3+R_1)B_{x_{2_{up}}}|_{i,j-\frac{1}{2},k+\frac{1}{2}}^{n+\frac{1}{2}}\end{array}\right]\\
&-Q_{e_z4}\left[(R_2+R_4)B_{z_{ave}}|_{i,j+\frac{1}{2},k+\frac{1}{2}}^{n+\frac{1}{2}}-(R_2+R_4)B_{z_{ave}}|_{i,j-\frac{1}{2},k+\frac{1}{2}}^{n+\frac{1}{2}}\right]\\
&-Q_{e_z5}R_1\left[E_y|_{i,j+\frac{1}{2},k+1}^{n+\frac{1}{2}}-E_y|_{i,j+\frac{1}{2},k}^{n+\frac{1}{2}}-E_y|_{i,j-\frac{1}{2},k+1}^{n+\frac{1}{2}}+E_y|_{i,j-\frac{1}{2},k}^{n+\frac{1}{2}}\right]\\
&-\frac{1}{4}Q_{e_z1}R_2\left[\begin{array}{l}E_x|_{i+\frac{1}{2},j+1,k}^{n+\frac{1}{2}}-E_x|_{i+\frac{1}{2},j,k}^{n+\frac{1}{2}}+E_x|_{i+\frac{1}{2},j+1,k+1}^{n+\frac{1}{2}}-E_x|_{i+\frac{1}{2},j,k+1}^{n+\frac{1}{2}}\\+E_x|_{i-\frac{1}{2},j+1,k}^{n+\frac{1}{2}}-E_x|_{i-\frac{1}{2},j,k}^{n+\frac{1}{2}}+E_x|_{i-\frac{1}{2},j+1,k+1}^{n+\frac{1}{2}}-E_x|_{i-\frac{1}{2},j,k+1}^{n+\frac{1}{2}}\end{array}\right]\\
&+\frac{1}{4}Q_{e_z1}R_2\left[\begin{array}{l}E_x|_{i+\frac{1}{2},j,k}^{n+\frac{1}{2}}-E_x|_{i+\frac{1}{2},j-1,k}^{n+\frac{1}{2}}+E_x|_{i+\frac{1}{2},j,k+1}^{n+\frac{1}{2}}-E_x|_{i+\frac{1}{2},j-1,k+1}^{n+\frac{1}{2}}\\+E_x|_{i-\frac{1}{2},j,k}^{n+\frac{1}{2}}-E_x|_{i-\frac{1}{2},j-1,k}^{n+\frac{1}{2}}+E_x|_{i-\frac{1}{2},j,k+1}^{n+\frac{1}{2}}-E_x|_{i-\frac{1}{2},j-1,k+1}^{n+\frac{1}{2}}\end{array}\right]
\end{aligned}
\tag{2A-6}
$$

where $Q_{e_z1}=(\Delta t^2)/[4\epsilon_r\epsilon_0(\Delta y)^2]$, $Q_{e_z2}=(\Delta t^2)/(4\epsilon_r\epsilon_0\Delta y\Delta x)$, $Q_{e_z3}=\Delta t/(2\epsilon_r\epsilon_0\Delta x)$, $Q_{e_z4}=\Delta t/(2\epsilon_r\epsilon_0\Delta y)$, $Q_{e_z5}=(\Delta t^2)/(4\epsilon_r\epsilon_0\Delta y\Delta z)$, $R_n=A_n/A_0$ at the corresponding mesh.

Chapter 3

BAW Mediated Multiferroic Antennas

In a dynamic multiferroic system, the behavior of acoustic waves and electromagnetic waves are respectively governed by Newton's laws and Maxwell's equations as follows

$$\nabla \cdot \boldsymbol{T} = \rho \frac{\partial \boldsymbol{v}}{\partial t},\ \nabla_S \boldsymbol{v} = \frac{\partial \boldsymbol{S}}{\partial t} \tag{3.0-1}$$

$$\nabla \times \boldsymbol{E} = -\frac{\partial \boldsymbol{B}}{\partial t},\ \nabla \times \boldsymbol{H} = \sigma \boldsymbol{E} + \frac{\partial \boldsymbol{D}}{\partial t} \tag{3.0-2}$$

where in Eq. (3.0-1), $\boldsymbol{v}$ is the particle velocity vector, $\boldsymbol{\rho}$ is the mass density of the material and $\boldsymbol{\sigma}$ is the conductivity. The behavior of the BAW mediated multiferroic antenna can thus be predicted with an FDTD algorithm that jointly solves these two sets of equations.

3.1 Architecture and Performance Bound

Due to the thin profile of the structure, both the magnetostrictive and piezoelectric layers are assumed to extend to infinity in the film plane with uniform strain and stress field distributions. The FDTD modeling in this section is thus 1-D. The purpose of this model is not to design a practical antenna structure but to understand the fundamental physics and coupling between the electromagnetics and dynamic mechanics. Therefore, Newton's law (3.0-1) and Maxwell's equations (3.0-2) are reduced to their 1-D forms respectively:

$$\frac{\partial T}{\partial t} = \rho \frac{\partial v}{\partial t},\ \frac{\partial v}{\partial z} = \frac{\partial S}{\partial t}$$

$$\frac{\partial E}{\partial z} = -\frac{\partial B}{\partial t},\ \frac{\partial H}{\partial z} = \sigma E + \frac{\partial D}{\partial t} \tag{3.1-1}$$

3.1.1 1-D FDTD Formulation with Constant Permeability

The bilateral interactions between the acoustic waves and electromagnetic waves are thus modeled by substituting the strain mediated constitutive relations Eq. (1.2-4) and Eq. (1.2-5) into Eq. (3.1-1). The combination of Eq. (1.2-4) and Eq. (3.1-1) leads to 1-D differential equations in the piezoelectric layer:

$$\frac{\partial E}{\partial t} = -\frac{e_D}{\epsilon_S}\frac{\partial v}{\partial z} + \frac{1}{\epsilon_S}\frac{\partial D}{\partial t} \tag{3.1-2}$$

$$\frac{\partial T}{\partial t} = c_D\frac{\partial v}{\partial z} - \frac{e_D}{\epsilon_S}\frac{\partial D}{\partial t} \tag{3.1-3}$$

where the electric flux density D serves as the excitation. Similarly, the combination of Eq. (1.2-5) and Eq. (3.1-1) leads to 1-D differential equations in the magnetostrictive layer:

$$\frac{\partial H}{\partial t} = -\frac{e_B}{\mu_S}\frac{\partial v}{\partial z} + \frac{1}{\mu_S}\frac{\partial B}{\partial t} \tag{3.1-4}$$

$$\frac{\partial T}{\partial t} = c_B\frac{\partial v}{\partial z} - \frac{e_B}{\epsilon_S}\frac{\partial B}{\partial t} \tag{3.1-5}$$

In order to solve the equations in Eq. (3.1-1) simultaneously, the FDTD method must perform time marching for both the electromagnetic field variables and the mechanical field variables on the same time scale. However, as the wavelength of an acoustic wave is approximately five orders of magnitude smaller than that of an electromagnetic wave at the same frequency, the drastic difference between the spatial scales of these two types of waves gives rise to a numerical issue. In order to retain the spatial resolution for acoustic waves, the spatial grids need to be divided based on the smaller wavelength of the two waves, which is typically no more than one tenth of the acoustic wavelength. In order to satisfy the stability condition, the time steps must be defined according to the shorter traveling time of the two waves when they cross

each spatial grid, which is

$$\Delta t = \min\left(\frac{\Delta z_{ac}}{c}, \frac{\Delta z_{ac}}{v_{ac}}\right) \tag{3.1-6}$$

Note that $c/v_{ac} \approx 10^5$, it is thus concluded that Δt must be much smaller than the RF cycle, which would lead to severe oversampling in time-domain and extremely poor computational efficiency. To avoid the oversampling issue, different spatial scales are applied to these two different waves. For electromagnetic waves, due to its large wavelength, one may use a much sparser grid than that of the acoustic waves to describe its spatial behavior and then interpolate the electromagnetic field inside the large grid with polynomial basis functions to match the field variables of the acoustic waves. This leads to the reduction in the number of unknowns for electromagnetic field variables and avoids the stability problem or oversampling problem. Specific to the 1-D FDTD algorithm implemented for thin film structures, a single grid is needed to represent the electromagnetic field unknowns in the magnetic material and the following polynomial spatial expansion of electromagnetic field is used to derive the field on the acoustic wave grid:

$$B_x = B_{x0}, H_x = H_{x0}, E_y = E_{y1} z \tag{3.1-7}$$

where B_{x0}, H_{x0}, E_{y1} are unknowns to be solved by 1-D FDTD. If more dramatic electromagnetic field variation is expected, higher order terms could be added to Eq. (3.1-7) for better accuracy. With Eq. (3.1-7), Faraday's law in Eq. (3.1-1) reduces to

$$\frac{\partial B_x}{\partial t} = \frac{\partial E_y}{\partial z} = E_{y1} \tag{3.1-8}$$

The radiation boundary condition takes the form,

$$\left.\frac{E_y}{H_x}\right|_{z=h} = -\eta_0 \tag{3.1-9}$$

which yields,

$$\frac{\partial H_x}{\partial t} = -\frac{1}{\eta_0}\left.\frac{\partial E_y}{\partial t}\right|_{z=h} = -\frac{h}{\eta_0}\frac{\partial E_{y1}}{\partial t} \tag{3.1-10}$$

Submitting Eq. (3.1-8) to Eq. (3.1-4) gives,

$$E_{y1} = \mu_S \frac{\partial H_x}{\partial t} + e_B \frac{\partial v}{\partial z} \tag{3.1-11}$$

With Eq. (3.1-10) submitted into Eq. (3.1-11) to eliminate $\frac{\partial H_x}{\partial t}$ and Eq. (3.1-8) substituted to Eq. (3.1-5) to eliminate $\frac{\partial B_x}{\partial t}$, one obtains the following two differential equations,

$$\frac{\mu_S h}{\eta_0}\frac{\partial E_{y1}}{\partial t} + E_{y1} = e_B \frac{\partial v}{\partial z} \tag{3.1-12}$$

$$\frac{\partial T}{\partial t} = c_B \frac{\partial v}{\partial z} - \frac{e_B}{\mu_S} E_{y1} \tag{3.1-13}$$

These two equations are solved jointly with the following Newton's equation,

$$\frac{\partial T}{\partial z} = \rho \frac{\partial v}{\partial t} \tag{3.1-14}$$

Note that Eq. (3.1-14) applies to the whole structure including both the piezoelectric and the magnetostrictive layers. The equations (3.1-12) and (3.1-13) are replaced by the following equations in the piezoelectric layer:

$$\frac{\partial D}{\partial t} = \epsilon_S \frac{\partial E_z}{\partial t} + e_D \frac{\partial v}{\partial z} \tag{3.1-15}$$

$$\frac{\partial T}{\partial t} = c_D \frac{\partial v}{\partial z} - \frac{e_D}{\epsilon_S}\frac{\partial D}{\partial t} \tag{3.1-16}$$

The leap-frog time stepping scheme in FDTD can now be implemented to discretize equations

(3.1-12) to (3.1-16) in spatial and temporal domain, which leads to

$$E_{y1}^{n+1/2} = \frac{\frac{\mu_S h}{\eta_0 \Delta t} - 0.5}{\frac{\mu_S h}{\eta_0 \Delta t} + 0.5} E_{y1}^{n-1/2} + mean\left\{ \frac{e_B}{0.5 + \frac{\mu_S h}{\eta_0 \Delta t}} \frac{v_{i+1/2}^n - v_{i-1/2}^n}{\Delta z} \right\} \tag{3.1-17}$$

$$T_i^{n+1/2} = T_i^{n-1/2} + c_B \frac{v_{i+1/2}^n - v_{i-1/2}^n}{\Delta z} \Delta t - \frac{e_B}{\mu_S} \frac{E_{y1}^{n+1/2} + E_{y1}^{n-1/2}}{2} \Delta t \tag{3.1-18}$$

for the magnetostrictive layer and

$$T_i^{n+1/2} = T_i^{n-1/2} + c_D \frac{v_{i+1/2}^n - v_{i-1/2}^n}{\Delta z} \Delta t - \frac{e_D}{\epsilon_S} \left(D_i^{n+1/2} + D_i^{n-1/2} \right) \tag{3.1-19}$$

$$E_{z_i}^{n+1/2} = E_{z_i}^{n-1/2} + c_D \frac{v_{i+1/2}^n - v_{i-1/2}^n}{\Delta z} \Delta t - \frac{1}{\epsilon_S} \left(D_i^{n+1/2} + D_i^{n-1/2} \right) \tag{3.1-20}$$

for the piezoelectric layers, and

$$v_{i+1/2}^{n+1} = v_{i+1.2}^n + \frac{\Delta t}{\rho \Delta z} \left(T_i^{n+1/2} + T_{i-1}^{n+1/2} \right) \tag{3.1-21}$$

for both phases.

In the magnetostrictive layer, Eq. (3.1-17) describes the time-marching of the aperture electric field as a function of the particle velocity. Both the electric field and the particle velocity are used to update the stress in Eq. (3.1-18) and then the particle velocity is updated from stress in Eq. (3.1-21). An electrical flux density in the form of modified Gaussian pulse $D(t) = \exp\left[-(t-t_0)^2/2T^2\right]\cos(2\pi f t)$ is applied through the vertical direction of the bottom piezoelectric layer, as the excitation of the resonance. In the piezoelectric layer, the vertical electric flux density is used with the particle velocity to update the stress in Eq. (3.1-19), the vertical electric field is then updated with the electric flux density excitation and the particle velocity in Eq. (3.1-20), and ultimately the particle velocity is updated with the stress in Eq. (3.1-21).

3.1.2 1-D Performance Bound

For simplification of discussions, the BAW structure to be simulated is assumed to contain only dispersionless and lossless material. The mechanical property of the material is matched to those of typical ferrite and piezoelectric material. For example, the magnetostrictive material is assumed to have a similar mechanical property to that of yttrium iron garnet (YIG) and the piezoelectric material is assumed with a similar mechanical property to that of zinc oxide (ZnO). The following are the material properties assumed for the simulation: $\epsilon_T = 12.64\epsilon_0$, $\mu_T = 2000\mu_0$, $c_D = 2.3032\times10^{11}\ [N/m^2]$, $c_H = 2.11\times10^{11}\ [N/m^2]$, $d_H = 1.04\times10^{-7}\ [m/A]$, $d_D = 11.67\times10^{-12}\ [C/N]$, $e_D = 1.32\ [C/m^2]$, $\rho_E = 5.68\times10^{3}\ [kg/m^3]$, $\rho_H = 5.17\times10^{3}\ [kg/m^3]$. It should be noted that the dynamic permeability and the piezomagnetic coefficients of the magnetostrictive material are artificially adjusted to study the effects of those parameters critical to the antenna performance. The aforementioned material properties lead to a magnetomechanical coupling figure of merit $k_H^2 = 0.9080$. The central frequency of the excitation is $f = 1.0\ GHz$ with a bandwidth of +/-300MHz. With the electromagnetic unknown reduction strategy, the time step and spatial grid can now be defined based on the properties of BAW,

$$\Delta z = \frac{\lambda_{av}}{108} \approx 50\ nm, \Delta t = \frac{\Delta z}{v_{ac}}\frac{1}{16} \approx 50\ ps \tag{3.1-22}$$

Figure 3.1-1 shows the dynamic stress waveform at the center of the magnetostrictive layer of the structure shown in Figure 1.2-3 obtained by the proposed FDTD simulation. The amplitude of the standing stress field decays due to the electromagnetic radiation. It implies that the radiation of electromagnetic waves acts as a damping load to the acoustic wave resonances.

Figure 3.1-2 plots the vertical stress profile in the 3-layer BAW structure as a function of time, for the first three resonant modes. It is observed that electromagnetic radiation occurs when the mechanical strain is maximized in the middle layer, as shown in Figure 3.1-2a and Figure 3.1-2c. However, when there is a null of the strain profile in the middle layer, no radiation is observed, which is shown in Figure 3.1-2b. This further validates the concept that the electromagnetic radiation is created only through the dynamic magnetic flux generated by the strain excitation.

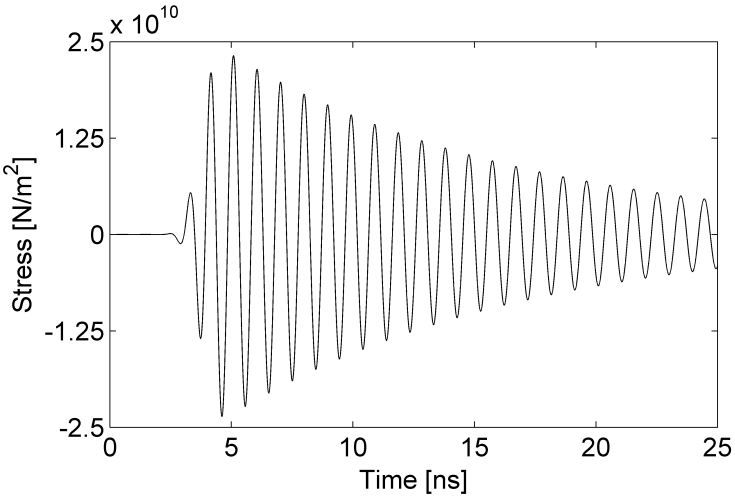

Figure 3.1-1. Dynamic stress field in the middle line of the proposed BAW mediated multiferroic antenna structure shown in Figure 1.2-3.

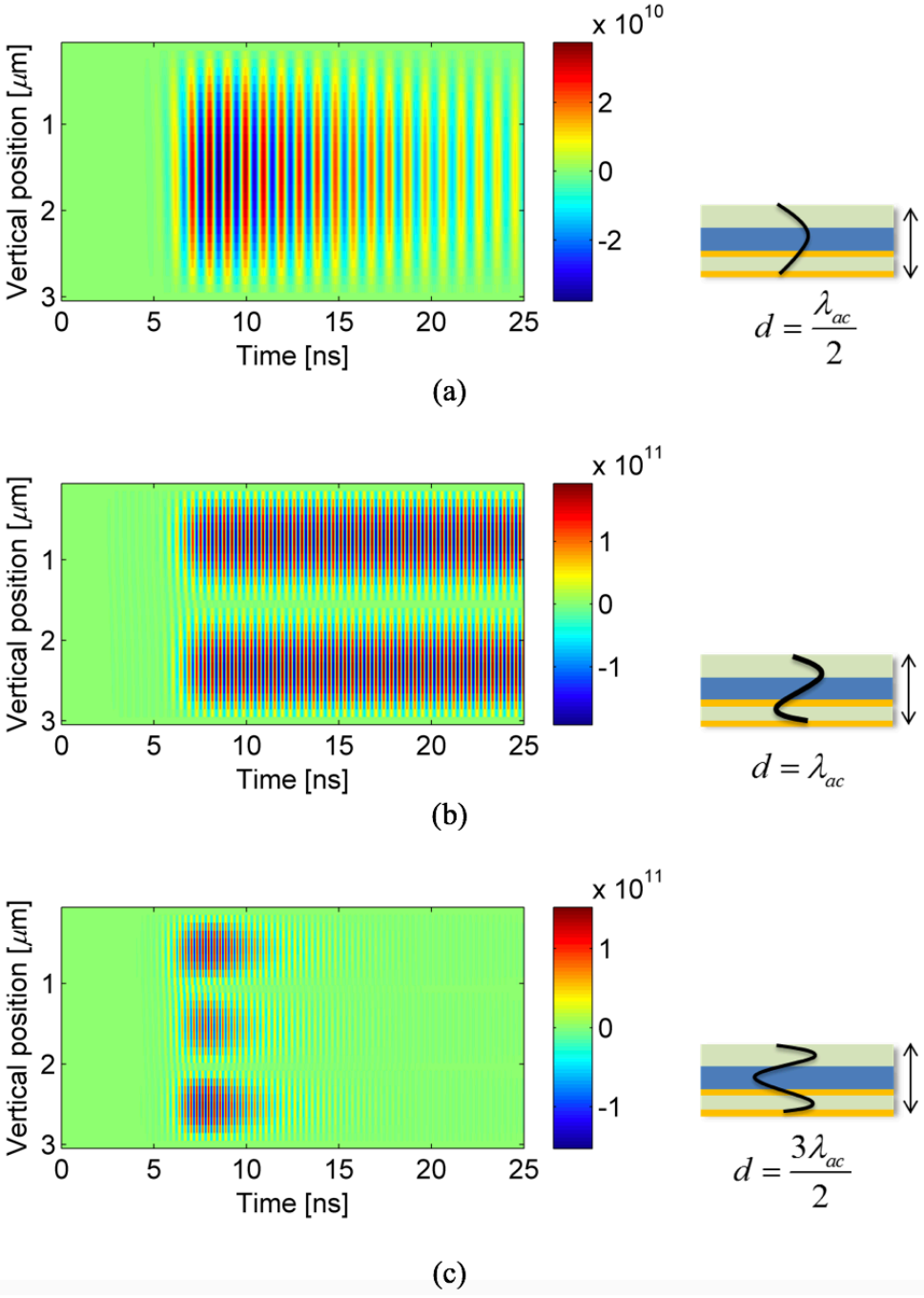

Figure 3.1-2. Stress profiles throughout the BAW structure as a function of time for different resonant modes. **a.** $f = 1.03\ GHz$, **b.** $f = 2.28\ GHz$, **c.** $f = 3.17\ GHz$.

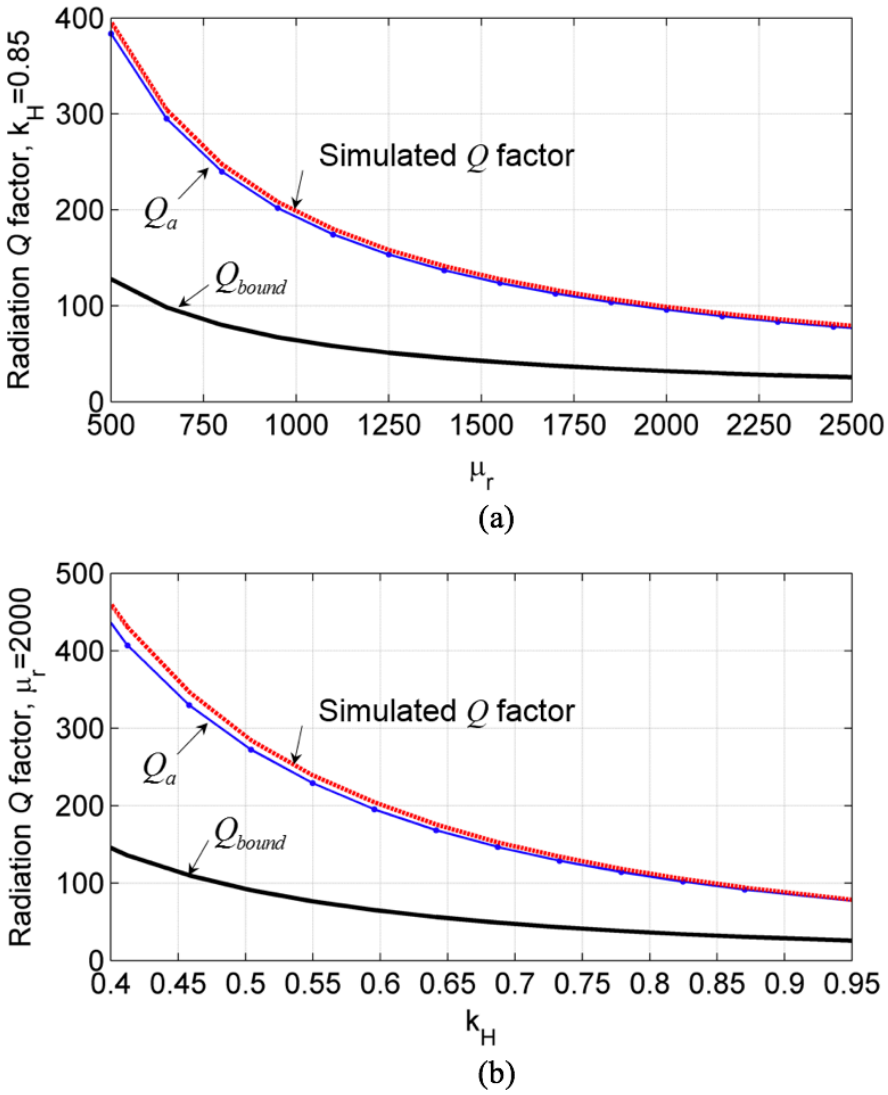

Figure 3.1-3. **a.** Simulated radiation Q factor compared to the theory for different permeability, $\boldsymbol{k_H = 0.85}$. **b.** Simulated radiation Q factor compared to the theory for different magnetomechanical coupling figure of merits, $\boldsymbol{\mu_r = 2000}$. Parameters in Figure 1.2-3 apply.

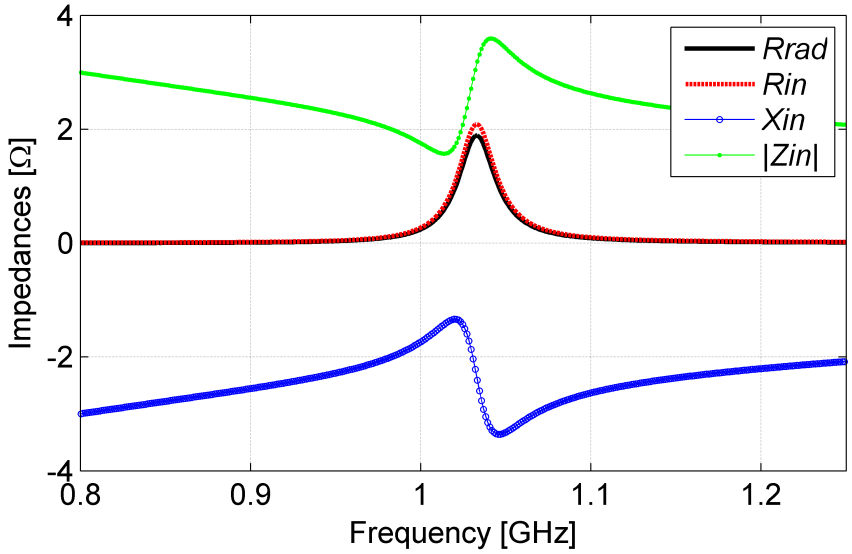

Figure 3.1-4. Input impedance and radiation resistance for a reference area of 1 mm^2.

Radiation quality factors are derived from the simulated stress waveform by extracting the damping speed of the resonance incurred by the electromagnetic radiation with the signal processing code ESPRIT. Based on the aforementioned material property setting, the theoretical lower bound of radiation Q factor is 25.5 according to Eq. (3.1-14), which corresponds to the analytical radiation Q of 76.4 for the BAW mediated antenna. The simulated radiation Q factor of the antenna with FDTD code is 77.9, which is very close to the analytical result. In general, the simulated radiation Q factor matches well with the analytical radiation Q factor for different permeability settings and magnetomechanical coupling figure of merits as shown in Figure 3.1-3. The agreement between the numerical solutions and the analytic solutions validates both the operating principle of the proposed antenna structure and the FDTD algorithm developed for solving such a multi-physics problem. Furthermore, it shows that a relative permeability of 2000 and a magnetomechanical coupling figure of merit greater than 85% in the magnetostrictive

material could lead to efficient radiation (with radiation Q factor of below 100) at 1.03 GHz even with a 1-μm-thick layer of magnetostrictive material.

The antenna input impedance and radiation resistance as functions of frequency are calculated with different methods with both results plotted in Figure 3.1-4 for comparison. The antenna input impedance is calculated by taking the ratio of the input voltage to the excitation displacement current. The input voltage is obtained by performing the line integral of vertical electric field through the bottom piezoelectric layer, and the excitation displacement current is computed by $I = A(\partial D/\partial t)$. The radiation resistance is calculated using the ratio between the radiated power obtained with Eq. (3.1-12) and the square of the excitation displacement current. In Figure 3.1-4, the input resistance agrees well with the radiation resistance even though they are obtained with different approaches. The agreement has further validated the FDTD simulation method. The radiation resistance is 1.9 Ohms per square millimeter near BAW resonance.

3.2 1-D BAW Mediated Multiferroic Antennas Near Ferromagnetic Resonance

The one dimensional finite difference time domain (1D FDTD) algorithm in the previous section [7] explores the effect of BAW on the electromagnetic resonance, by modeling the bidirectional coupling of these two phenomena in a multiferroic antenna that is composed of alternating layers of piezoelectric and magnetostrictive materials. It is evident that the electromagnetic energy released from the device is generated by the odd mode BAW resonances. Little electromagnetic radiation is observed from even mode BAW resonances because the mechanic energy is null in the middle magnetostrctive layer. To explore the effect of magnetic

dispersion, or FMR, on the antenna performance, a current-driven thin-film ferrite antenna was simulated in [65], with the similar FDTD technique. However, in order to accurately predict the performance of the multiferroic antenna, both FMR effect and eddy current loss should be included, besides electromagnetic coupling, BAW, piezoelectricity and magnetostriction. There are respectable amount of work targeted at the electromagnetic performance of the magnetic material, with or without [15, 18, 70-72] magnetostriction. Micromagnetic modeling has been a popular method to explore the dynamic magnetization, domain patterns, or hysteresis [18, 68, 69, 71]. In the case of eddy current loss, the magnetic field H is modified with an additional term H_{eddy} [70, 72]. Since most of the aforementioned work focus on the magnetization, simplified or quasi-static Maxwell's equations are considered [67, 69].

3.2.1 Energy-Coupling Figure of Merit

In order to fully investigate the multiferroic antenna performance, the complete form of Maxwell's equation, together with LLG equation, Newton's law, and the constitutive coupling relations, should be solved simultaneously. To realize this goal, we apply the prototype 1D FDTD modeling to the three-layer strain-mediated multiferroic antenna structure. Therefore, it takes into account the coupling between electromagnetics, acoustics, and magnetic dispersion. The radiation efficiency of the antenna and the mechanical-magnetic figure of merit of the magnetostrictive material, are obtained from the simulation and plotted as functions of frequency and magnetic DC bias, respectively.

The structure of BAW mediated multiferroic antenna is shown in Figure 1.2-3. It consists of one thin magnetostrictive layer sandwiched by two thin piezoelectric layers, which are

isolated from the silicon wafer by an air cavity. The electric current or voltage applied to the electrodes of the bottom layer creates mechanic strain field through converse piezoelectric effect. The strain field is coupled into the middle magnetostrictive layer and hence the whole sandwiched structure, which forms the bulk acoustic resonance. As long as the acoustic standing wave amplitude is maximized in the middle layer, the strain field could be transferred into dynamic magnetic flux though piezomagnetic effect. This magnetic flux leads to aperture magnetic field which indicates the generation of electromagnetic radiation. Instead of conductive current, the radiating source of BAW antennas is the time-varying magnetic flux induced by the dynamic mechanic strain. As a result, the absence of image current leads to suppressed amount of reactive energy storage and improved radiation performance at GHz, even when the antenna is extremely low-profile.

The stress field enforced on the magnetostrictive material induces an equivalent magnetization, denoted as $M(d_B T)$, where d_B is the strain constant of the magnetostrictive layer, and it is a third rank tensor, in the unit of (meter·Ampere)/Newton. The subscript B indicates that the value of $d_B$is measured under the condition of constant magnetic flux density, instead of constant magnetic field, which is the case for d_H. The value of d_B could be calculated from d_H by

$$d_B = d_H/\mu_T \tag{3.2-1}$$

In Eq. (3.2-1), $\mu_T = (1+\chi)\mu_0$ is used to denote the stress independent permeability of the magnetostrictive material, where χ is the susceptibility. In materials with magnetic dispersion, since d_B is a constant and μ_T is frequency dependent, the value of d_H will be dispersive.

Therefore, the total magnetization could be decomposed into two components, the first one

is induced purely by the magnetic field and is independent of the stress field, denoted as $M_{Maxwell}$, and the second one is $M(d_B T)$, which is stress-dependent. In equation form,

$$M_{total} = M_{total} + M(d_B T) \tag{3.2-2}$$

In the case of zero magnetic field, $M_i = d_{Bijk} T_{jk}$. According to Eq. (3.2-2), the total magnetic flux density could be expanded as in $B_{total} = \mu_0 [H_{Maxwell} + M_{total}]$, which is further expanded as in

$$\begin{aligned} B_{total} &= \mu_0 [H_{Maxwell} + M_{Maxwell} + M(d_B T)] \\ &= \mu_0 (H_{Maxwell} + M_{Maxwell}) + \mu_0 M(d_B T) \\ &= \mu_0 (1 + \chi) H_{Maxwell} + \mu_0 \chi d_B : \boldsymbol{T} \end{aligned} \tag{3.2-3}$$

which results in the expression of the magnetic field,

$$H_{Maxwell} = \frac{B_{total}}{\mu_0 (1+\chi)} - \frac{\chi}{1+\chi} d_B : \boldsymbol{T} = \frac{B_{total}}{\mu_T} - \frac{\chi}{1+\chi} d_B : \boldsymbol{T} \tag{3.2-4}$$

According to Eq. (3.2-3) and Eq. (3.2-4), the physical meaning of χ becomes explicit. The susceptibility χ is the ratio of the magnetization to the corresponding magnetic field, e.g. $M_{Maxwell}$ to $H_{Maxwell}$, and $M(d_B T)$ to $d_B : \boldsymbol{T}$. The value of χ is not changed by the stress field. Based on all the known conditions, we have constitutive coupling equations, also called the magnetostrictive strain equations:

$$M_{total} = \frac{1}{\mu_0} B_{total} - H_{Maxwell} \tag{3.2-5}$$

$$\boldsymbol{S} = s_B : \boldsymbol{T} + d_B \cdot \mu_0 M_{total} \tag{3.2-6}$$

The compliance coefficient s_B is obtained from the Young's modulus, and it is a fourth rank tensor.

$$s_B = s_H\left(1 - \frac{d_H^2}{\mu_T s_H}\right) \tag{3.2-7}$$

where $s_H = 1/c_H$, and c_H is the Young's modulus.

The energy conservation relation that is derived in [7] introduces the magnetomechanical coupling figure of merit k_H^2, which is an important parameter to predict the maximum percentage of mechanical energy that can be transferred into magnetic energy. However, k_H^2 is defined based on the static properties of the material. In dynamic cases, a corresponsive dynamic coupling coefficient needs to be defined, so that we can explore the frequency-dependent performance of the multiferroic antenna. According to Eq. (3.2-5), we can rewrite M_{total} in terms of B_{total}, $H_{Maxwell}$ and $d_B{:}\boldsymbol{T}$. For simplicity, this process is completed in 1-D form. Substituting Eq. (3.2-4) into Eq. (3.2-5) gives

$$M_{total} = \frac{B}{\mu_0} - \frac{B}{\mu_T} + \frac{\chi}{1+\chi} d_B T = \frac{\chi}{1+\chi}\frac{1}{\mu_0} B + \frac{\chi}{1+\chi} d_B T \tag{3.2-8}$$

The same conclusion indicated by Eq. (3.2-8) can be verified by an alternative way:

$$M_{total} = \chi(H_{Maxwell} + d_B T) = \chi\left(\frac{B}{\mu_T} - \frac{\chi}{1+\chi} d_B T + d_B T\right)$$

$$= \frac{\chi}{1+\chi}\frac{1}{\mu_0} B + \frac{\chi}{1+\chi} d_B T \tag{3.2-9}$$

where we can define an equivalent total magnetic field $H_{total} = H_{Maxwell} + d_B T$. This total magnetic field is an equivalent force that drives the magnetization in the material to change. Both Eq. (3.2-8) and Eq. (3.2-9) simplifies Eq. (3.2-6) into the 1D form,

$$S = s_B T + d_B \cdot \mu_0\left(\frac{\chi}{1+\chi}\frac{1}{\mu_0} B + \frac{\chi}{1+\chi} d_B T\right)$$

$$= s_B T + d_B \frac{\chi}{1+\chi} B + d_B^2 \mu_0 \frac{\chi}{1+\chi} T \tag{3.2-10}$$

Therefore, the total mechanical energy stored in the antenna structure is

$$W_{mechanical} = \iiint_V (S \cdot T)\, dV$$

$$= \iiint_V s_B |T|^2\, dV + \iiint_V d_B^2 \mu_0 \frac{\chi}{1+\chi} |T|^2\, dV + \iiint_V d_B \frac{\chi}{1+\chi} (B \cdot T)\, dV \qquad (3.2\text{-}11)$$

and the total magnetic energy is

$$W_{magnetic} = \iiint_V (B \cdot H)\, dV$$

$$= \iiint_V \frac{|B|^2}{\mu_0(1+\chi)} dV - \iiint_V d_B \frac{\chi}{1+\chi} (B \cdot T)\, dV \qquad (3.2\text{-}12)$$

The additional term $\iiint_V d_B^2 \mu_0 \frac{\chi}{1+\chi} |T|^2\, dV$ in Eq. (3.2-11) is due to the stress-independent nature of χ. Therefore, the total stored energy stored in the antenna system is calculated as

$$W_{total} = W_{magnetic} + W_{mechanical}$$

$$= \iiint_V \frac{|B|^2}{\mu_0(1+\chi)} dV + \iiint_V s_B |T|^2\, dV + \iiint_V d_B^2 \mu_0 \frac{\chi}{1+\chi} |T|^2\, dV \qquad (3.2\text{-}13)$$

With the assumption of relatively low radiation performance, $H_{Maxwell} \approx 0$. According to Eq. (3.2-4), we have

$$T \approx \frac{B}{\mu_T} \cdot \frac{1+\chi}{\chi d_B} = \frac{B}{\chi \mu_0 d_B} \qquad (3.2\text{-}14)$$

which reduces Eq. (3.2-13) to

$$W_{total} = \iiint_V \left[\frac{|B|^2}{\mu_0(1+\chi)} + s_B \frac{|B|^2}{\chi^2 \mu_0^2 d_B^2} + d_B^2 \mu_0 \frac{\chi}{1+\chi} \frac{|B|^2}{\chi^2 \mu_0^2 d_B^2} \right] dV$$

$$= \frac{\chi(1+\chi)\mu_0 d_B^2 + s_B}{\chi^2 \mu_0 d_B^2} \iiint_V \frac{|B|^2}{\mu_0(1+\chi)} dV \qquad (3.2\text{-}15)$$

As mentioned earlier, the magnetomechanical figure of merit is the maximum ratio of the mechanical energy input that can be transferred to magnetic energy and stored in the form of

magnetic flux density. In equation form, this definition is interpreted by

$$W_{total} = \frac{1}{k_B^2} W_{magnetic} \tag{3.2-16}$$

Combing Eq. (3.2-15) and Eq. (3.2-16), we can get the expression of k_B^2:

$$k_B^2 = \frac{\chi^2 \mu_0 d_B^2}{\chi(1+\chi)\mu_0 d_B^2 + s_B} \tag{3.2-17}$$

Since in Eq. (3.2-17), the only frequency dependent parameter is χ, the relation between k_B^2 and χ could be explored and plotted. The upper bound of k_B^2 is that $k_B^2 \leq 1$.

3.2.2 1-D FDTD Formulation

The original vector form of the Maxwell and LLG dynamic system is composed of the following equations as in Eq. (3.2-18)–Eq. (3.2-22). Equation (3.2-21) is the equation of motion, and Eq. (3.2-22) is the strain-displacement relation. The constitutive coupling equations (3.2-5) and (3.2-6) are repeated here for completeness.

$$\frac{\partial \boldsymbol{M}_{total}}{\partial t} = \mu_0 \gamma (\boldsymbol{M}_{total} \times \boldsymbol{H}_{total}) - \frac{\alpha}{|M_{total}|} \boldsymbol{M}_{total} \times \frac{\partial \boldsymbol{M}_{total}}{\partial t} \tag{3.2-18}$$

$$\frac{\partial \boldsymbol{E}}{\partial t} = \frac{1}{\epsilon_r \epsilon_0} \Delta \times \boldsymbol{H}_{Maxwell} - \frac{1}{\epsilon_r \epsilon_0} \sigma \boldsymbol{E} \tag{3.2-19}$$

$$\frac{\partial \boldsymbol{B}_{total}}{\partial t} = -\Delta \times \boldsymbol{E} \tag{3.2-20}$$

$$\nabla \cdot \boldsymbol{T} = \rho \frac{\partial \boldsymbol{v}}{\partial t} \tag{3.2-21}$$

$$\nabla_S \cdot \boldsymbol{v} = \frac{\partial \boldsymbol{S}}{\partial t} \tag{3.2-22}$$

$$\boldsymbol{M}_{total} = \frac{1}{\mu_0} \boldsymbol{B}_{total} - \boldsymbol{H}_{Maxwell} \tag{3.2-5}$$

$$\boldsymbol{S} = s_B : \boldsymbol{T} + d_B \cdot \mu_0 M_{total} \tag{3.2-6}$$

In Eq. (3.2-18), both gyromagnetic ratio γ and the damping factor α are negative. $\gamma = -1.759\times10^{-11}C/kg$ [6]. The damping factor α is calculated by the line width ΔH fixed at X-band (9.6GHz) [5]. In 1D case, Eq. (3.2-21) and Eq. (3.2-22) reduce to

$$\frac{\partial T}{\partial z} = \rho \frac{\partial v}{\partial t} \tag{3.2-23}$$

$$\frac{\partial v}{\partial z} = \frac{\partial S}{\partial t} \tag{3.2-24}$$

Apply the magnetic DC bias in the *y* direction, to minimize the demagnetization. Under small signal approximation, the LLG equation Eq. (3.2-18) can be written in terms of *B* and *H* in scalar form [15]:

$$\frac{1}{\mu_0}\frac{\partial b_z}{\partial t} - \frac{\partial h_z}{\partial t} = \gamma[H_i b_x - \mu_0(M_S + H_i)(h_x + d_B T)] + \alpha\left[\frac{1}{\mu_0}\frac{\partial b_x}{\partial t} - \frac{\partial h_x}{\partial t}\right] \tag{3.2-25}$$

$$\frac{1}{\mu_0}\frac{\partial b_x}{\partial t} - \frac{\partial h_x}{\partial t} = \gamma[-H_i b_z + \mu_0(M_S + H_i)h_z] - \alpha\left[\frac{1}{\mu_0}\frac{\partial b_z}{\partial t} - \frac{\partial h_z}{\partial t}\right] \tag{3.2-26}$$

$$b_y = \mu_0 h_y \tag{3.2-27}$$

where M_S is the saturation magnetization, H_i is the applied internal DC magnetic bias. Since for the thin film, the in-plane demagnetizing factor is zero, H_i equals the external DC bias. The lowercase letters in the equations represents dynamic fields, while the uppercase letters represent static fields. It should be noticed that Eq. (3.2-25)–Eq. (3.2-27) are derived on the premise that the term $d_B T$ is dominant in *x* direction, i.e. the magnetic field direction of the EM radiation. Using the same spatial unknown reduction method, assume $e_y = e_{y1} z$ and $h_x = h_{x0} + h_{x2} z^2$. The plane wave radiation boundary condition $\left(e_y/h_x\right)_{z=h} = -\eta_0$ gives

$$h_{x0} = -\frac{d}{\eta_0} e_{y1} - h_{x2} d^2 \tag{3.2-28}$$

where η_0 is the intrinsic impedance of free space. The 1D simplification of Maxwell's equations (3.2-19) and (3.2-20) leads to

$$\frac{\partial b_x}{\partial t} = \frac{\partial e_y}{\partial z} = e_{y1}, e_z = 0, b_z = 0 \tag{3.2-29}$$

Equation (3.2-29) simplifies Eq. (3.2-25) and Eq. (3.2-26) into

$$-\frac{\partial h_z}{\partial t} = \gamma H_i b_x - \gamma \mu_0 (M_S + H_i)(h_x + d_B T) + \frac{\alpha}{\mu_0} e_{y1} - \alpha \frac{\partial h_x}{\partial t} \tag{3.2-30}$$

$$\frac{1}{\mu_0} e_{y1} - \frac{\partial h_x}{\partial t} = \gamma \mu_0 (M_S + H_i) h_z + \alpha \frac{\partial h_z}{\partial t} \tag{3.2-31}$$

Take the time derivative of Eq. (3.2-6) and utilize Eq. (3.2-29), we get

$$\begin{aligned} \frac{\partial S}{\partial t} &= \mu_0 d_B \frac{\partial M}{\partial t} + s_B \frac{\partial T}{\partial t} \\ &= s_B \frac{\partial T}{\partial t} + d_B \frac{\partial T}{\partial t} - \mu_0 d_B \frac{\partial H}{\partial t} \\ &= s_B \frac{\partial T}{\partial t} + d_B e_{y1} - \mu_0 d_B \frac{\partial h_x}{\partial t} \\ &= \frac{\partial v}{\partial z} \end{aligned} \tag{3.2-32}$$

In summary, the scalar differential equations that will be used in the FDTD coding are as follows:

$$h_{x0} = -\frac{\epsilon_r \epsilon_0 d^2}{2} \frac{\partial e_{y1}}{\partial t} - \left(\frac{\sigma d^2}{2} + \frac{d}{\eta_0}\right) e_{y1} \tag{3.2-33}$$

$$h_{x2} = \frac{\epsilon_r \epsilon_0}{2} \frac{\partial e_{y1}}{\partial t} + \frac{\sigma}{2} e_{y1} \tag{3.2-34}$$

$$-\frac{\partial h_z}{\partial t} = \gamma H_i b_x - \gamma \mu_0 (M_S + H_i)(h_x + d_B T) + \frac{\alpha}{\mu_0} e_{y1} - \alpha \frac{\partial h_x}{\partial t} \tag{3.2-35}$$

$$\frac{1}{\mu_0} e_{y1} - \frac{\partial h_x}{\partial t} = \gamma \mu_0 (M_S + H_i) h_z + \alpha \frac{\partial h_z}{\partial t} \tag{3.2-36}$$

$$\frac{\partial b_x}{\partial t} = e_{y1} \tag{3.2-37}$$

$$\frac{\partial T}{\partial z} = \rho \frac{\partial v}{\partial t} \tag{3.2-38}$$

$$\frac{\partial v}{\partial z} = s_B \frac{\partial T}{\partial t} + d_B e_{y1} - \mu_0 d_B \frac{\partial h_x}{\partial t} \tag{3.2-39}$$

The differential equations in the piezoelectric layers are the same to those in [7]. An electrical flux density in the form of a modulated Gaussian pulse $D(t) = \exp[-(t - t_0)^2/2T^2]\cos(2\pi f t)$ is applied through the vertical direction of the bottom piezoelectric layer to excite the resonance.

3.2.3 Modeling Results and Analysis

Typical material properties of yttrium iron garnet (YIG) and ZnO [73, 74] are applied in the FDTD code: $\epsilon_T = 12.64\epsilon_0$, $c_D = 2.3032\times10^{11}\ [N/m^2]$, $c_H = 2.11\times10^{11}\ [N/m^2]$, $d_D = 11.67\times10^{-12}\ [C/N]$, $e_D = 1.32\ [C/m^2]$, $\rho_E = 5.68\times10^3\ [kg/m^3]$, $\rho_H = 5.17\times10^3\ [kg/m^3]$, $4\pi M_S = 1750\ [Gauss]$. Additionally, the initial values of d_H and μ_r are assumed as follows: $d_H|_{DC} = 0.05\ [ppm/Oe]$, and $\mu_r|_{DC} = 1 + M_S/H_i \approx 30$. The damping factor α of YIG is calculated from the FMR linewidth $\Delta H = 20\ Oe$.

The radiation efficiencies of an aperture area of 1 mm^2 as a function of frequency, as well as the mechanical-magnetic figure of merit k_B^2, are shown in Figure 3.2-1. The radiation

efficiency is calculated using $\xi_{rad} = R_{rad}/R_{in}$, where $R_{rad} = 2P_{rad}/I^2$, $Z_{in} = \left(\int_{-h}^{0} E_z\, dz\right)/I$, and $I = (\partial D/\partial t) \cdot A$. The value of k_B^2 drops to almost zero at FMR, however, it reaches to the peak value in the vicinity of FMR, due to the large value of μ' and μ''. By tuning the applied DC magnetic bias in the *y* direction, we are able to couple FMR and BAW resonance together and get enhanced radiation efficiency over a wide bandwidth. However, due to the null of k_B^2, there is always a dip on the curve of the radiation efficiency. Nevertheless, the two resonances could be manipulated to be as close to each other as possible, in order to get as high radiation as possible. As can be seen from Figure 3.2-2, the eddy current loss in the middle magnetostrictive layer could dramatically reduce the antenna radiation performance. Therefore, the desired material for antenna radiation is that with high value of permeability near FMR, and with low electric conductivity.

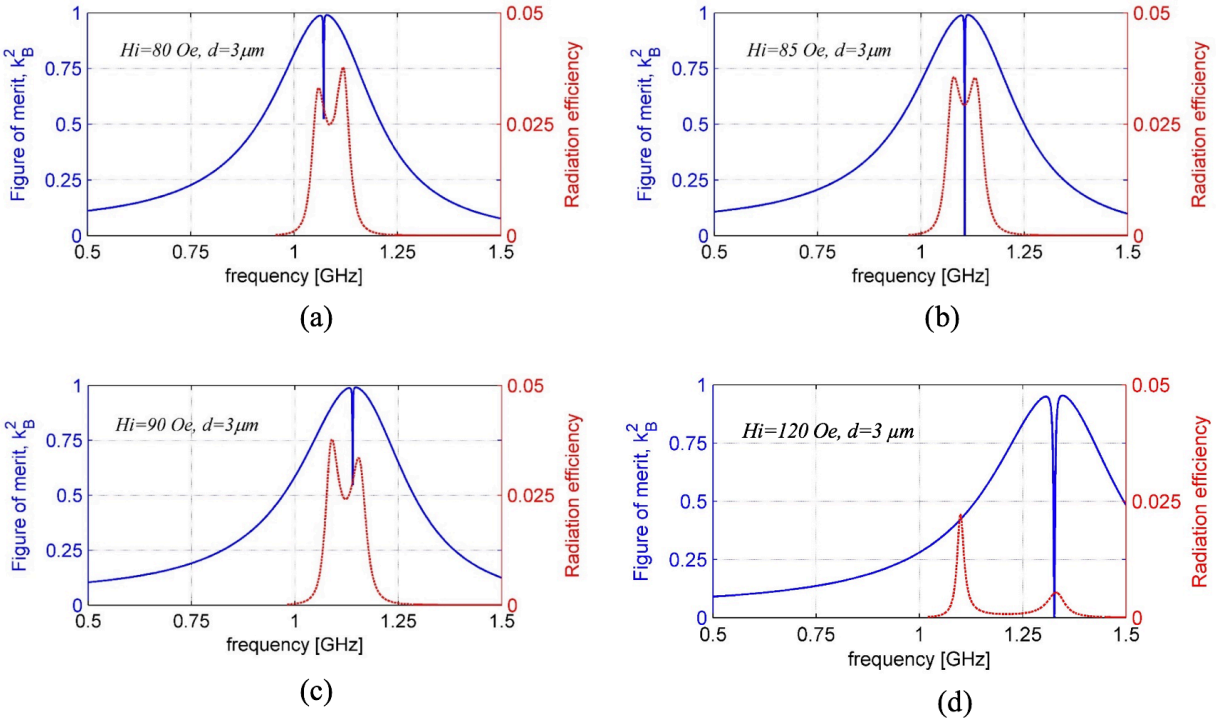

Figure 3.2-1. Radiation efficiency for an aperture area of 1 mm^2 (red curve), and mechanical-magnetic figure of merit $\boldsymbol{k_B^2}$ (blue curve) with magnetic DC biases. **a.** H_i=80 *Oe*, **b.** H_i=85 *Oe*, **c.** H_i=90 *Oe,* **d.** H_i=120 *Oe*. The conductivity of the magnetostrictive material is zero.

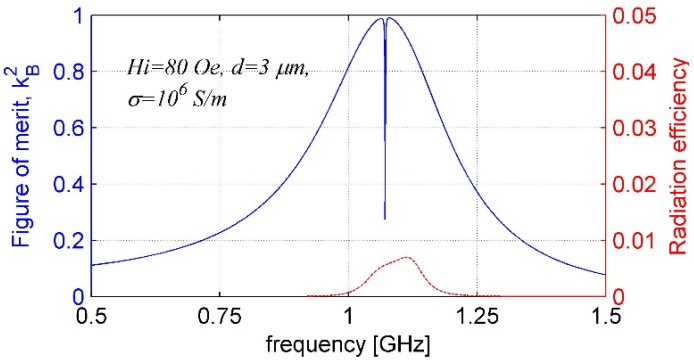

Figure 3.2-2. Radiation efficiency for an aperture area of 1 mm^2 (red curve), and mechanical-magnetic figure of merit $\boldsymbol{k_B^2}$ (blue curve) with magnetic DC bias H_i=80 *Oe*. The conductivity of the magnetostrictive material is $\boldsymbol{\sigma = 10^6}$ S/m.

3.3 3-D MUST Modeling

The 1-D framework presented in the last section is under the assumption of infinite planar dimension, with the edge effect ignored. To fully visualize the antenna performance, we adopt the multiphysics modeling algorithm to the BAW antennas. As shown in Figure 3.3-1, with our 3D modeling tool, we now have the complete capability to capture all the physics in the BAW antenna. Therefore, the BAW antenna radiation performance can be fully explored and optimized. The procedure of time-marching can be repeated on the basis of Section 2.2, and will not be expatiated. The time-stepping equations are advanced from Section 2.5 with the addition of mechanical stress field. The material properties uitilized in the BAW antenna design are specified in Table 3-1.

	h [nm]	Stiffness	$\rho\ [kg/m^3]$	$d_D[C/N]$ $d_B[ppm/Oe]$	$e_D[C/m^2]$	$4\pi M_S\ [Gauss]$	$\Delta H\ [Oe]$
AlN	500	$c_D = 389$ GPa	3.3×10^3	3×10^{-12}	1.55	\	\
FeGaB	400	Young's: 60 GPa Poisson's: 0.3	7.8×10^3	3	\	10000	50
Al_2O_3	400	Young's: 400 GPa Poisson's: 0.21	3.965×10^3	\	\	\	\

Table 3-1. Material properties utilized in the BAW antenna design.

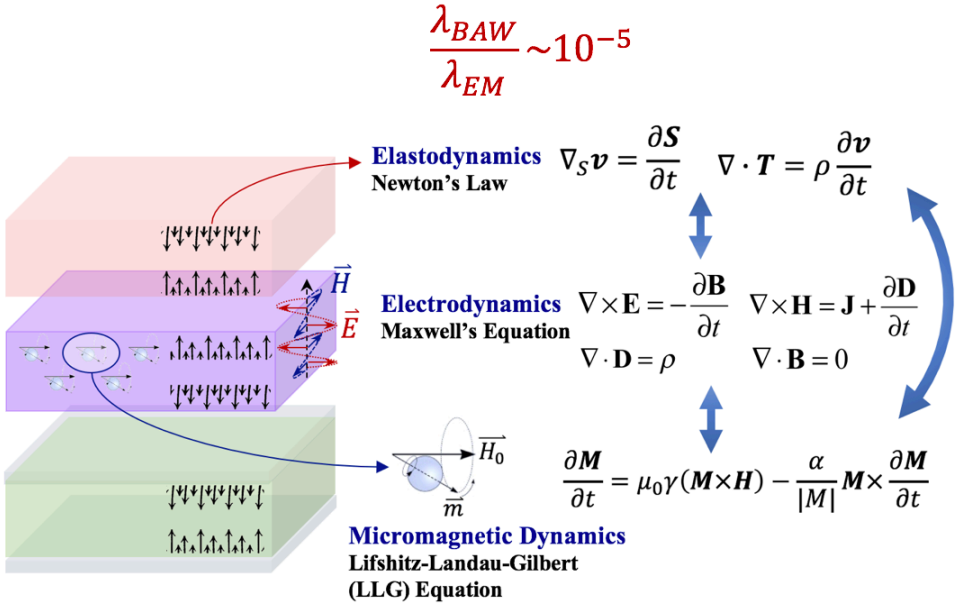

Figure 3.3-1. Multiphysics interaction in BAW antenna in 3-D framework.

The stress field shown by Figure 3.3-2 clearly reveals that the electromagnetic radiation comes from the BAW resonance, and Figure 3.3-3 demonstrates the effect of FMR on the magneto-mechanical coupling. The radiation efficiency is enhanced when the FMR frequency is chosen to overlap with that of the BAW resonance. Figure 3.3-4 shows the radiation patterns, which are similar among different bias fields, with only minor asymmetry change of the cross-pol. The relatively high cross-pol is due to the anisotropic property of the magnetic material.

As shown by Figure 3.3-5, multiferroic antennas achieve efficiency-bandwidth products approaching to that defined by Chu's limit [75], which validates the effectiveness of the electrically small multiferroic structure in supporting radiation out of it. Benchmark against the Chu's limit has shown the potential of using such multiferroic antennas, especially in the integrated circuit application with the modern nano-fabrication technology.

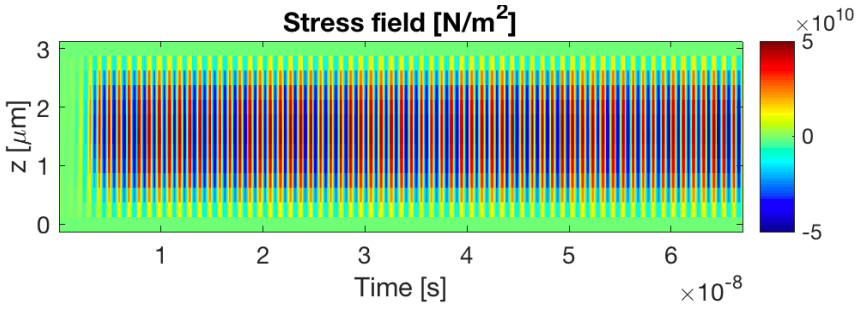

(a)

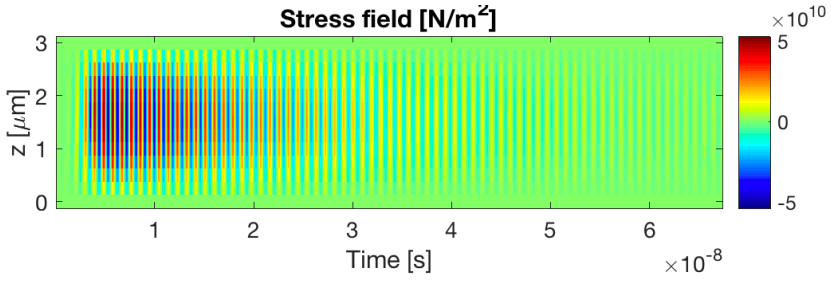

(b)

Figure 3.3-2. Stress field in the BAW antenna. **a.** Magnetostrictive coupling turned off. **b.** Magnetostrictive coupling turned on, $\mathbf{H_0 = 80\ Oe}$. The magneto-elastic material is assumed to have a similar mechanical property to that of YIG and the piezoelectric material with a similar mechanical property to that of zinc oxide (ZnO). It should be noted that the materials are artificially adjusted to study the effects of those parameters critical to the antenna performance.

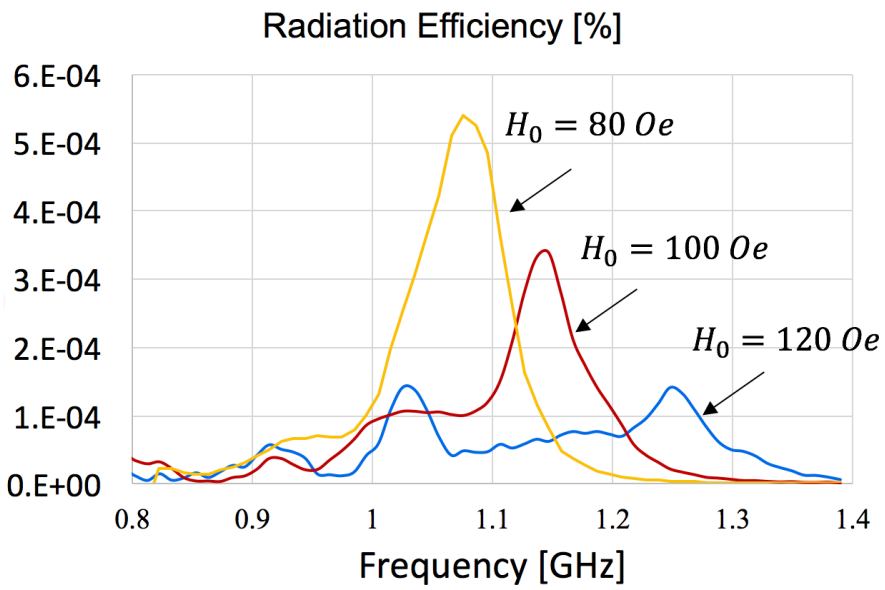

Figure 3.3-3. Radiation efficiency under various in-plane magnetic DC bias.

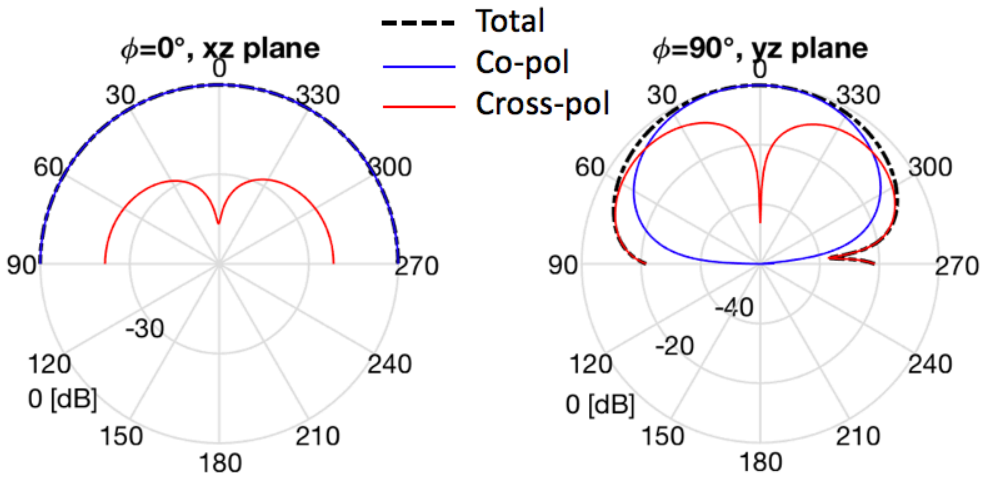

Figure 3.3-4. Far-field pattern of total radiated field, $\mathbf{H_0 = 80\ Oe}$.

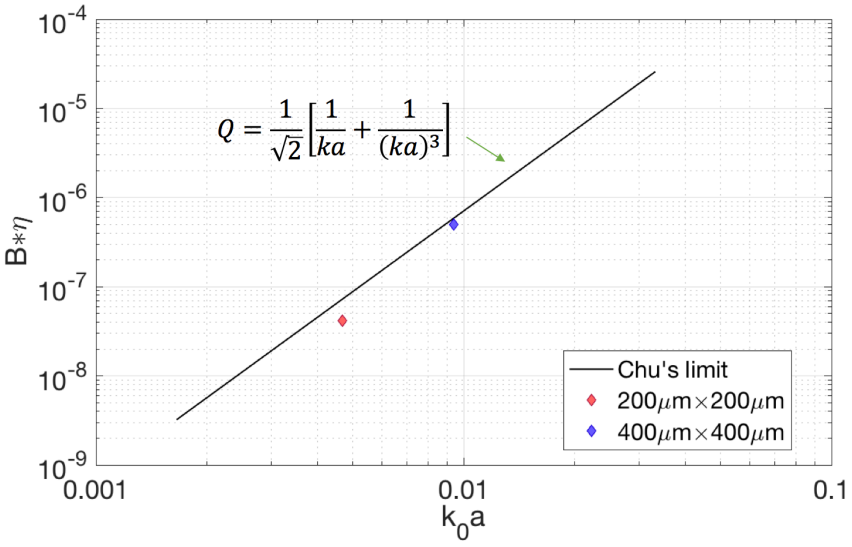

Figure 3.3-5. Benchmark of BAW antenna versus Chu's limit.

Chapter 4

Summary

4.1 Conclusion

In this dissertation, we successfully proposed a multiphysics modeling technique based on ADI FDTD is proposed for the first time, to accurately model the dynamic interaction between micromagnetics and electrodynamics. The proposed method can model the fine detail of RF magnetic devices such as those containing magnetic thin films, and predict the dispersive and anisotropic properties of magnetic materials with high computational efficiency. With further expansion to include nonlinearity, magnetocrystalline anisotropy, exchange coupling and spin transfer torque, the proposed algorithm can be potentially used to design nonlinear RF magnetic and spintronic devices.

Moreover, we have demonstrated by simulation that multiferroic antennas based on the dynamic interactions of electromagnetic and acoustic waves open up a new territory in conformal antenna design. BAW resonator structures are proposed to form effective dynamic strain coupling to a thin magnetostrictive layer, which may generate the dynamic magnetic flux needed for electromagnetic wave radiation. Both 1-D multi-scale FDTD code and the 3-D modeling tool are developed to model the proposed antenna structure. Numerical results agree well with the analytical results, which validates to both theoretical and numerical analyses. The analyses conclude that at the vicinity of FMR in the magnetic layer and with a reasonable magnetomechanical coupling figure of merit, the proposed BAW based multiferroic antenna can achieve a low radiation Q that may eventually lead to high efficiency radiation required for a practical antenna deployment.

4.2 Outlook

Magnetic materials by nature are nonlinear, dispersive, non-reciprocal and anisotropic in microwave regime even within the framework of classical micromagnetics described by the LLG theory. The non-reciprocal and anisotropic property of the magnetic material are the underlying mechanisms of magnetic circulators or polarizers, while the nonlinear and dispersive property of the magnetic materials can be utilized to create frequency selective limiters (FSL) or signal to noise enhancers (SNE) that can operate in a RF front-end to maintain its high sensitivity in a hostile environment.

Currently, the state of the art in modeling RF magnetic components is significantly lagging those consisting of only electric material. Most commercial software being limited to modeling simple, linear material behavior which is not representative of material response in actual hardware. The 3-D MUST algorithm we propose in this dissertation has brought a big step forward toward the realization of such a comprehensive simulation tool, yet has not included the nonlinear effect. Furthermore, applications of thin or thick magnetic film components are thriving thanks to the maturing of nanofabrication technologies such as sputtering or deposition techniques. High quality films are readily available with thickness dimensions in the order of $1/1000^{th}$ to $1/10000^{th}$ of the wavelength, ranging from a few μm to a few tens of μm that could be beneficial to developing advanced antennas and filters even at the low GHz frequencies. While the materials are available, the dramatic scale difference cannot be adequately addressed with commercial software due to the overwhelming computational complexity in both space and time gridding.

The instrinsic nonlinear and dispersive effects are critically important such as the excitation of spin waves through exchange of the magnetic domains with wavelengths in the order of 10 nm. These are important mechanisms contributing to line width broadening and frequency dependent dissipation observed in FSL and SNE. While important, modeling of such effects in a comprehensive way requires spatial resolutions down to a couple of nanometers, creating a modeling problem spanning six orders of magnitude in overall spatial scale, with governing physics being nonlinear quantum theory, including coupling and scattering of multiple magnons. Rigorous modeling of such physics over a practical device dimension is impossible even with the fastest supercomputer in the world. Existing micromagnetic simulators such as OOMMF can only model 3-D structures with dimensions up to only a few tens of nanometers in each direction. Adding nonlinearity to the formulation of spin waves could further exacerbate the computational complexity in such a software and resulting in more unrealistic computation time.

The ultimate goal of our study is to attack this grand challenge through development of a multi-physics, multi-scale time-domain solver that can model the seven orders of magnitudes scale difference from nanometers to centimeters, including the physics from electromagnetic waves, acoustic waves to the nonlinear generation of dipole-exchange spin waves into one unified framework. Eventually, we would like to provide a comprehensive and precise modeling solution for nonlinear magnetics, which is numerically affordable in comparison to existing commercial software.

References

[1] P. K. Amiri and K. L. Wang, "Voltage-controlled magnetic anisotropy in spintronic devices," *SPIN,* vol. 02, p. 1240002, 2012.

[2] C. Jizhai, M. K. Scott, L. Cheng-Yen, P. C. Gregory, and S. L. Christopher, "Nanoscale magnetic ratchets based on shape anisotropy," *Nanotechnology,* vol. 28, p. 08LT01, 2017.

[3] W. Mingzhong and H. Axel, *Solid State Physics*. vol. Volume 64, Eds., ed: Academic Press, 2013, p. iv.

[4] V. G. Harris, "Modern Microwave Ferrites," *Magnetics, IEEE Transactions on,* vol. 48, pp. 1075-1104, 2012.

[5] B. Lax and K. J. Button, *Microwave Ferrites And Ferrimagnetics*: Literary Licensing, LLC, 2012.

[6] D. M. Pozar, *Microwave Engineering*: JohnWiley & Sons, Inc., 2012.

[7] Z. Yao, Y. E. Wang, S. Keller, and G. P. Carman, "Bulk Acoustic Wave-Mediated Multiferroic Antennas: Architecture and Performance Bound," *IEEE Transactions on Antennas and Propagation,* vol. 63, pp. 3335-3344, 2015.

[8] H. Suhl, "The Nonlinear Behavior of Ferrites at High Microwave Signal Levels," *Proceedings of the IRE,* vol. 44, pp. 1270-1284, 1956.

[9] R. W. Orth, "Frequency-Selective Limiters and Their Application," *IEEE Transactions on Electromagnetic Compatibility,* vol. EMC-10, pp. 273-283, 1968.

[10] J. D. Adam and S. N. Stitzer, "A magnetostatic wave signal-to-noise enhancer," *Applied Physics Letters,* vol. 36, pp. 485-487, 1980.

[11] R. Chang, S. Li, M. V. Lubarda, B. Livshitz, and V. Lomakin, "FastMag: Fast micromagnetic simulator for complex magnetic structures (invited)," *Journal of Applied Physics,* vol. 109, p. 07D358, 2011.

[12] J. O. Oti, "SimulMag Version 1.0," 1997.

[13] M. J. Donahue and D. G. Porter, "OOMMF user's guide, version 1.0," N. I. S. Technol., Ed., ed. Gaithersburg, MD, USA: Tech. Rep. NISTIR 6376, 1999.

[14] A. Visintin, "On Landau-Lifshitz' equations for ferromagnetism," *Japan Journal of Applied Mathematics,* vol. 2, p. 69, 1985.

[15] J. A. Pereda, L. A. Vielva, M. A. Solano, A. Vegas, and A. Prieto, "FDTD analysis of magnetized ferrites: application to the calculation of dispersion characteristics of ferrite-loaded waveguides," *Microwave Theory and Techniques, IEEE Transactions on,* vol. 43, pp. 350-357, 1995.

[16] Y. Bo and D. R. Fredkin, "Dynamical micromagnetics by the finite element method," *IEEE Transactions on Magnetics,* vol. 34, pp. 3842-3852, 1998.

[17] P. B. Monk and O. Vacus, "Accurate discretization of a non-linear micromagnetic problem," *Computer Methods in Applied Mechanics and Engineering,* vol. 190, pp. 5243-5269, 7/20/ 2001.

[18] A. V. Farahani and A. Konrad, "FDTD Calculation of Cavity Resonant Frequencies in Case of Nonuniform Internal Magnetic Field Distribution," in *Electromagnetic Field Computation, 2006 12th Biennial IEEE Conference on*, 2006, pp. 117-117.

[19] F. Bruckner, C. Vogler, B. Bergmair, T. Huber, M. Fuger, D. Suess*, et al.*, "Combining micromagnetism and magnetostatic Maxwell equations for multiscale magnetic simulations," *Journal of Magnetism and Magnetic Materials,* vol. 343, pp. 163-168, 10// 2013.

[20] S. Couture and V. Lomakin, "Electromagnetic-Micromagnetic Simulator for Magnetization-Eddy Current Dynamics in Magnetic Materials and Devices," presented at the 2017 IEEE International Symposium on Antennas and Propagation (APSURSI), San Diego, CA, 2017.

[21] Y. Kane, "Numerical solution of initial boundary value problems involving maxwell's equations in isotropic media," *Antennas and Propagation, IEEE Transactions on,* vol. 14, pp. 302-307, 1966.

[22] A. Taflove and S. C. Hagness, *Computational electrodynamics: the finite-difference time-domain method*: Artech house, 2005.

[23] T. Namiki, "A new FDTD algorithm based on alternating-direction implicit method," *Microwave Theory and Techniques, IEEE Transactions on,* vol. 47, pp. 2003-2007, 1999.

[24] Z. Fenghua, C. Zhizhang, and Z. Jiazong, "Toward the development of a three-dimensional unconditionally stable finite-difference time-domain method," *Microwave Theory and Techniques, IEEE Transactions on,* vol. 48, pp. 1550-1558, 2000.

[25] Y.-S. Chung, T. K. Sarkar, B. H. Jung, and M. Salazar-Palma, "An unconditionally stable scheme for the finite-difference time-domain method," *IEEE Transactions on Microwave Theory and Techniques,* vol. 51, pp. 697-704, 2003.

[26] S. W. Staker, C. L. Holloway, A. U. Bhobe, and M. Piket-May, "Alternating-direction implicit (ADI) formulation of the finite-difference time-domain (FDTD) method: Algorithm and material dispersion implementation," *IEEE transactions on electromagnetic compatibility,* vol. 45, pp. 156-166, 2003.

[27] C. Sun and C. Trueman, "Unconditionally stable Crank-Nicolson scheme for solving two-dimensional Maxwell's equations," *Electronics Letters,* vol. 39, pp. 595-597, 2003.

[28] E. L. Tan, "Fundamental schemes for efficient unconditionally stable implicit finite-difference time-domain methods," *IEEE Transactions on Antennas and Propagation,* vol. 56, pp. 170-177, 2008.

[29] M. Gaffar and D. Jiao, "An Explicit and Unconditionally Stable FDTD Method for Electromagnetic Analysis," *IEEE Transactions on Microwave Theory and Techniques,* vol. 62, pp. 2538-2550, 2014.

[30] L. Martin, S. Crane, Y. Chu, M. Holcomb, M. Gajek, M. Huijben*, et al.*, "Multiferroics and magnetoelectrics: thin films and nanostructures," *Journal of Physics: Condensed Matter,* vol. 20, p. 434220, 2008.

[31] H. Schmid, "Multi-ferroic magnetoelectrics," *Ferroelectrics,* vol. 162, pp. 317-338, 1994/01/01 1994.

[32] D. M. Pozar, "Microstrip antennas," *Proceedings of the IEEE,* vol. 80, pp. 79-91, 1992.

[33] J. C. E. Sten, A. Hujanen, and P. K. Koivisto, "Quality factor of an electrically small antenna radiating close to a conducting plane," *Antennas and Propagation, IEEE Transactions on,* vol. 49, pp. 829-837, 2001.

[34] R. C. Hansen and M. Burke, "Antennas with magneto-dielectrics," *Microwave and Optical Technology Letters,* vol. 26, pp. 75-78, 2000.

[35] H. Mosallaei and K. Sarabandi, "Magneto-dielectrics in electromagnetics: concept and applications," *Antennas and Propagation, IEEE Transactions on,* vol. 52, pp. 1558-1567, 2004.

[36] P. M. T. Ikonen, K. N. Rozanov, A. V. Osipov, P. Alitalo, and S. A. Tretyakov, "Magnetodielectric Substrates in Antenna Miniaturization: Potential and Limitations," *Antennas and Propagation, IEEE Transactions on,* vol. 54, pp. 3391-3399, 2006.

[37] N. Altunyurt, M. Swaminathan, P. M. Raj, and V. Nair, "Antenna miniaturization using magneto-dielectric substrates," in *Electronic Components and Technology Conference, 2009. ECTC 2009. 59th*, 2009, pp. 801-808.

[38] F. Namin, T. G. Spence, D. H. Werner, and E. Semouchkina, "Broadband, Miniaturized Stacked-Patch Antennas for L-Band Operation Based on Magneto-Dielectric Substrates," *Antennas and Propagation, IEEE Transactions on,* vol. 58, pp. 2817-2822, 2010.

[39] Y. Xin Mi, S. Quan Hui, J. Ya, C. Qiang, X. Y. Zhou, K. Hong Wei*, et al.*, "Increasing the Bandwidth of Microstrip Patch Antenna by Loading Compact Artificial Magneto-Dielectrics," *Antennas and Propagation, IEEE Transactions on,* vol. 59, pp. 373-378, 2011.

[40] Y. Guo-Min, X. Xing, A. Daigle, O. Obi, M. Liu, L. Jing, *et al.*, "Planar Annular Ring Antennas With Multilayer Self-Biased NiCo-Ferrite Films Loading," *Antennas and Propagation, IEEE Transactions on,* vol. 58, pp. 648-655, 2010.

[41] Y. Guo-Min, X. Xing, A. Daigle, M. Liu, O. Obi, J. W. Wang, *et al.*, "Electronically Tunable Miniaturized Antennas on Magnetoelectric Substrates With Enhanced Performance," *Magnetics, IEEE Transactions on,* vol. 44, pp. 3091-3094, 2008.

[42] N. A. Hill, "Why Are There so Few Magnetic Ferroelectrics?," *The Journal of Physical Chemistry B,* vol. 104, pp. 6694-6709, 2000/07/01 2000.

[43] M. I. Bichurin, I. A. Kornev, V. M. Petrov, A. S. Tatarenko, Y. V. Kiliba, and G. Srinivasan, "Theory of magnetoelectric effects at microwave frequencies in a piezoelectric/magnetostrictive multilayer composite," *Physical Review B,* vol. 64, p. 094409, 08/06/ 2001.

[44] L. Mitoseriu and V. Buscaglia, "Intrinsic/extrinsic interplay contributions to the functional properties of ferroelectric-magnetic composites," *Phase Transitions,* vol. 79, pp. 1095-1121, 2006/12/01 2006.

[45] R. Ramesh and N. A. Spaldin, "Multiferroics: progress and prospects in thin films," *Nat Mater,* vol. 6, pp. 21-29, 01//print 2007.

[46] C.-W. Nan, M. I. Bichurin, S. Dong, D. Viehland, and G. Srinivasan, "Multiferroic magnetoelectric composites: Historical perspective, status, and future directions," *Journal of Applied Physics,* vol. 103, p. 031101, 2008.

[47] C. A. F. Vaz, J. Hoffman, C. H. Ahn, and R. Ramesh, "Magnetoelectric Coupling Effects in Multiferroic Complex Oxide Composite Structures," *Advanced Materials,* vol. 22, pp. 2900-2918, 2010.

[48] R. V. Petrov, A. S. Tatarenko, S. Pandey, G. Srinivasan, J. V. Mantese, and R. Azadegan. (2008, Miniature antenna based on magnetoelectric composites. *Electronics Letters 44(8),* 506-508. Available: http://digital-library.theiet.org/content/journals/10.1049/el_20080325

[49] R. J. Miller, W. P. Geren, and S. P. Hubbell, "Multiferroic antenna/sensor," ed: Google Patents, 2011.

[50] R. D. Mindlin, "Electromagnetic radiation from a vibrating quartz plate," *International Journal of Solids and Structures,* vol. 9, pp. 697-702, 6// 1973.

[51] R. B. Thompson, "A model for the electromagnetic generation of ultrasonic guided waves in ferromagnetic metal polycrystals," *Sonics and Ultrasonics, IEEE Transactions on,* vol. 25, pp. 7-15, 1978.

[52] P. C. Y. Lee, "Electromagnetic radiation from an AT-cut quartz plate under lateral-field excitation," *Journal of Applied Physics,* vol. 65, pp. 1395-1399, 1989.

[53] P. C. Y. Lee, Y. G. Kim, and J. H. Prevost, "Electromagnetic radiation from doubly rotated piezoelectric crystal plates vibrating at thickness frequencies," *Journal of Applied Physics,* vol. 67, pp. 6633-6642, 1990.

[54] Y. Zhi and Y. E. Wang, "Dynamic analysis of acoustic wave mediated multiferroic radiation via FDTD methods," in *Antennas and Propagation Society International Symposium (APSURSI), 2014 IEEE*, 2014, pp. 731-732.

[55] S. Ki-Wone, J. Saehoon, and K. Hyeongdong, "The modeling of thin-film bulk acoustic wave resonators using the FDTD method," *Electron Device Letters, IEEE,* vol. 23, pp. 327-329, 2002.

[56] J.-A. Kong, "Theorems of bianisotropic media," *Proceedings of the IEEE,* vol. 60, pp. 1036-1046, 1972.

[57] B. A. Auld, *Acoustic fields and waves in solids*: Рипол Классик, 1973.

[58] J. Rosenbaum, *Bulk acoustic wave theory and devices*: Artech House on Demand, 1988.

[59] S. Tiwari, P. Nordeen, Q. Xu, Z. Yao, Y. E. Wang, G. P. Carman*, et al.*, "Ferromagnetic resonance in bulk-acoustic wave multiferroic devices," in *Solid State Sensors, Actuators, and Microsystems Workshop (Hilton Head)*, 2016.

[60] W. Yuanxun and L. Hao, "Multimode parameter extraction for multiconductor transmission lines via single-pass FDTD and signal-processing techniques," *IEEE Transactions on Microwave Theory and Techniques,* vol. 46, pp. 89-96, 1998.

[61] R. Roy and T. Kailath, "ESPRIT-estimation of signal parameters via rotational invariance techniques," *Acoustics, Speech and Signal Processing, IEEE Transactions on,* vol. 37, pp. 984-995, 1989.

[62] C. A. Balanis, *Advanced engineering electromagnetics*: John Wiley & Sons, 1999.

[63] Z. Yao and Y. E. Wang, "3D ADI-FDTD modeling of platform reduction with thin film ferromagnetic material," in *Antennas and Propagation (APSURSI), 2016 IEEE International Symposium on*, 2016, pp. 2019-2020.

[64] Z. Yao, Q. Xu, and Y. E. Wang, "FDTD analysis of platform effect reduction with thin film ferrite," in *Radio and Wireless Symposium (RWS), 2015 IEEE*, 2015, pp. 59-61.

[65] L. u. Baňas, "Adaptive techniques for Landau–Lifshitz–Gilbert equation with magnetostriction," *Journal of Computational and Applied Mathematics,* vol. 215, pp. 304-310, 6/1/ 2008.

[66] G. Carbou, M. A. Efendiev, and P. Fabrie, "Global weak solutions for the Landau–Lifschitz equation with magnetostriction," *Mathematical Methods in the Applied Sciences,* vol. 34, pp. 1274-1288, 2011.

[67] R. Hu, A.-K. Soh, G.-P. Zheng, and Y. Ni, "Micromagnetic modeling studies on the effects of stress on magnetization reversal and dynamic hysteresis," *Journal of Magnetism and Magnetic Materials,* vol. 301, pp. 458-468, 6// 2006.

[68] Y. C. Shu, M. P. Lin, and K. C. Wu, "Micromagnetic modeling of magnetostrictive materials under intrinsic stress," *Mechanics of Materials,* vol. 36, pp. 975-997, 10// 2004.

[69] G. Hrkac, M. Kirschner, F. Dorfbauer, D. Suess, O. Ertl, J. Fidler*, et al.*, "Three-dimensional micromagnetic finite element simulations including eddy currents," *Journal of Applied Physics,* vol. 97, p. 10E311, 2005.

[70] M.M.Aziz, "Sub-nanosecond electromagnetic-micromagnetic dynamic simulations using the finite-difference time-domain method," *Progress In Electromagnetics Research B,* vol. 15, 2009.

[71] A. Magni, G. Bertotti, I. D. Mayergoyz, and C. Serpico, "Landau–Lifschitz–Gilbert dynamics and eddy current effects in metallic thin films," *Journal of Magnetism and Magnetic Materials,* vol. 254–255, pp. 210-212, 1// 2003.

[72] Z. Yao and Y. E. Wang, "Dynamic analysis of acoustic wave mediated multiferroic radiation via FDTD methods," in *Antennas and Propagation Society International Symposium (APSURSI), 2014 IEEE*, 2014, pp. 731-732.

[73] L. J. Chu, "Physical Limitations of Omni-Directional Antennas," *Journal of Applied Physics,* vol. 19, pp. 1163-1175, 1948.